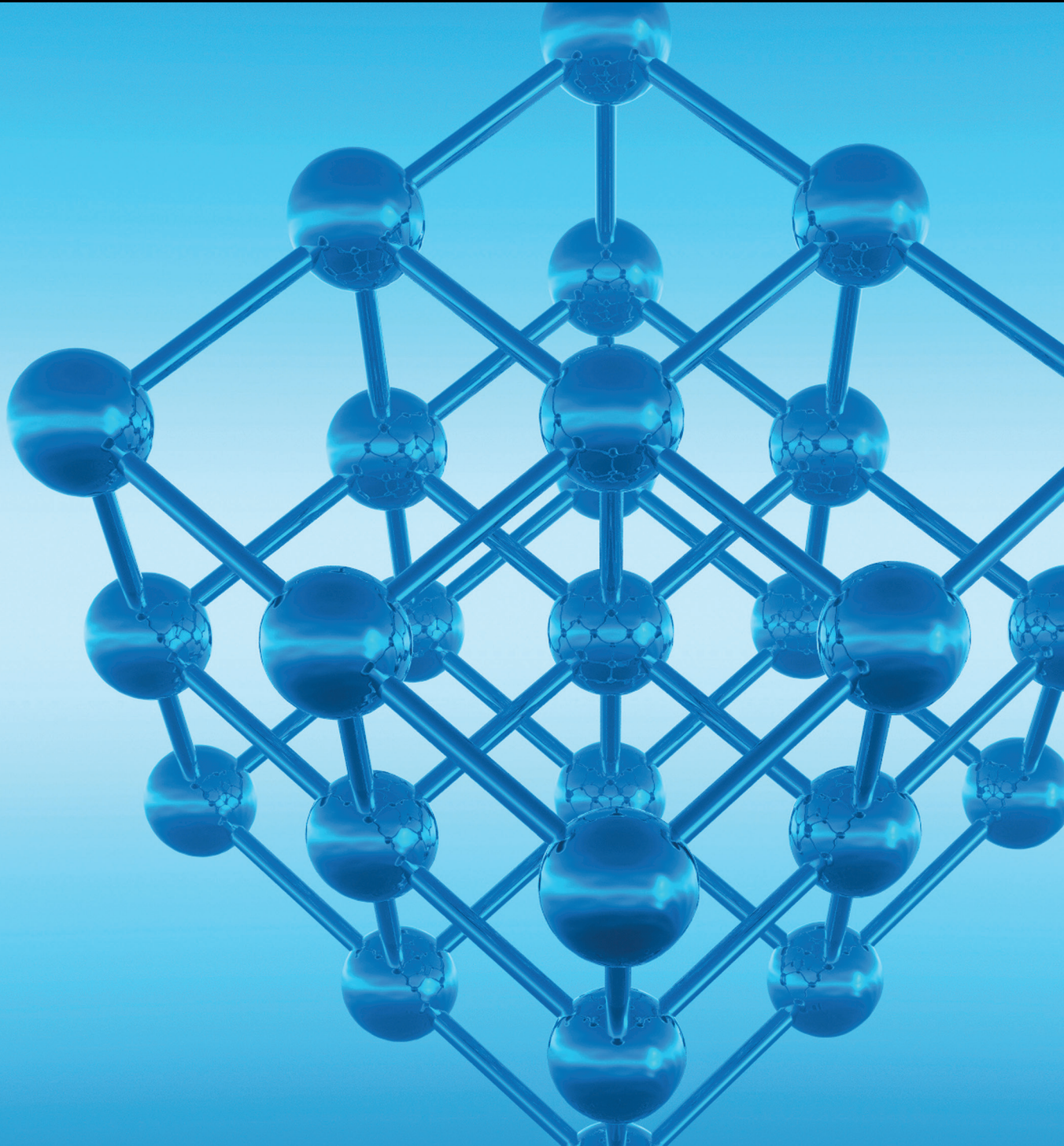


Advances in Condensed Matter Physics

Soft Matter Photonics

Lead Guest Editor: Shuan-Yu Huang

Guest Editors: Daniel Ho and Jia-De Lin






Soft Matter Photonics

Advances in Condensed Matter Physics

Soft Matter Photonics

Lead Guest Editor: Shuan-Yu Huang

Guest Editors: Daniel Ho and Jia-De Lin



Copyright © 2018 Hindawi. All rights reserved.

This is a special issue published in “Advances in Condensed Matter Physics.” All articles are open access articles distributed under the Creative Commons Attribution License, which permits unrestricted use, distribution, and reproduction in any medium, provided the original work is properly cited.

Editorial Board

Bohdan Andraka, USA
Ward Beyermann, USA
Golam M. Bhuiyan, Bangladesh
Luis L. Bonilla, Spain
Ashok Chatterjee, India
Ram N. P. Choudhary, India
Oleg Derzhko, Ukraine
Raouf El-Mallawany, Egypt

Gayanath Fernando, USA
Jörg Fink, Germany
Yuri Galperin, Norway
Prasenjit Guptasarma, USA
Da-Ren Hang, Taiwan
Jan A. Jung, Canada
Leonid Pryadko, USA
Charles Rosenblatt, USA

Sergei Sergeenkov, Brazil
Sergio E. Ulloa, USA
Markus R. Wagner, Germany
Gary Wysin, USA
Kiyokazu Yasuda, Japan
Fajun Zhang, Germany
Jiandi Zhang, USA

Contents



Soft Matter Photonics

Shuan-Yu Huang , Daniel Ho, and Jia-De Lin 
Editorial (2 pages), Article ID 5971203, Volume 2018 (2018)


Circular Polarization and Wavelength Selective Gratings Based on Holographic Cholesteric Liquid Crystal Templates

Hsien-Kuo Chin, Hui-Ying Kuo, Yang-Chen Zheng, Jia-De Lin , and Chia-Rong Lee
Research Article (8 pages), Article ID 5384329, Volume 2018 (2018)

Enhanced Photoluminescence in Gold Nanoparticles Doped Homogeneous Planar Nematic Liquid Crystals

Chi-Huang Chang, Rong-Ji Lin, Chuen-Lin Tien , and Shang-Min Yeh 
Research Article (5 pages), Article ID 8720169, Volume 2018 (2018)


Optical Modeling Analysis of Red, Green, and Yellow Phosphors with a Blue LED

Wen-Shing Sun and Chuen-Lin Tien 
Research Article (10 pages), Article ID 5716259, Volume 2018 (2018)

Angle-Scanning Surface Plasmon Resonance System with 3D Printed Components for Biorecognition Investigation

ChenGuang Zhang, Ching-Jung Chen , Kalpana Settu, and Jen-Tsai Liu 
Research Article (7 pages), Article ID 5654010, Volume 2018 (2018)



Electrically Tunable Diffraction Grating Based on Liquid Crystals

Chuen-Lin Tien , Rong-Ji Lin, Shu-Hui Su, and Chi-Ting Horng 
Research Article (4 pages), Article ID 7849529, Volume 2018 (2018)



Voltage-Controllable Guided Propagation in Nematic Liquid Crystals

Hsin-Yu Yao and Shang-Min Yeh 
Research Article (4 pages), Article ID 8185641, Volume 2018 (2018)

Light Leakage of Multidomain Vertical Alignment LCDs Using a Colorimetric Model in the Dark State

Chuen-Lin Tien , Rong-Ji Lin, and Shang-Min Yeh 
Research Article (6 pages), Article ID 6386428, Volume 2018 (2018)


Green LED as an Effective Light Source for Curing Acrylate-Based Dental Resins in Combination with Irgacure 784

Katalin Bukovinszky, Melinda Szalóki, István Csarnovics, Istvan Szabó, Sándor Kéki, Miklós Nagy ,
and Csaba Hegedűs 
Research Article (10 pages), Article ID 8265305, Volume 2018 (2018)

Effect of Oxygen Flow Rate on the Optical, Electrical, and Mechanical Properties of DC Sputtering ITO Thin Films

Chuen-Lin Tien , Hong-Yi Lin, Chih-Kai Chang, and Chien-Jen Tang
Research Article (6 pages), Article ID 2647282, Volume 2018 (2018)

High Sensitivity Refractive Index Sensor by D-Shaped Fibers and Titanium Dioxide Nanofilm

Chuen-Lin Tien , Hong-Yi Lin, and Shu-Hui Su
Research Article (6 pages), Article ID 2303740, Volume 2018 (2018)

Editorial

Soft Matter Photonics

Shuan-Yu Huang ^{1,2}, **Daniel Ho**,³ and **Jia-De Lin** ⁴

¹*School of Optometry, Chung Shan Medical University, Taichung 402, Taiwan*

²*Department of Ophthalmology, Chung Shan Medical University Hospital, Taichung 402, Taiwan*

³*Department of Electrical and Electronic Engineering, University of Bristol, Bristol BS8 1UB, UK*

⁴*Department of Photonics, National Cheng Kung University, Tainan 701, Taiwan*

Correspondence should be addressed to Shuan-Yu Huang; syhuang@csmu.edu.tw

Received 18 October 2018; Accepted 18 October 2018; Published 25 November 2018

Copyright © 2018 Shuan-Yu Huang et al. This is an open access article distributed under the Creative Commons Attribution License, which permits unrestricted use, distribution, and reproduction in any medium, provided the original work is properly cited.

As well known, photonics in soft matters, such as liquid crystals, polymers, and even bio-tissues, is a burgeoning and important field and attracting much attention in recent years. Soft matters possess some inherent advantages such as excellent tunability, high flexibility, scalable size, easy fabrication, and adaptation to environments. The variety of interesting properties in soft matters deserves not only fundamental researches but also potential applications, especially on photonics.

The aim of this special issue is focused on the discussions and developments of soft matter photonics and related applications. In this special issue, the editors collect interesting and fruitful works on soft matter photonics, ranging from fundamental studies to applied devices. The possibility of soft matter based applications, such as sensors, tunable gratings and waveguides, and photoluminescence, are also presented in this special issue.

In the article entitled “High Sensitivity Refractive Index Sensor by D-Shaped Fibers and Titanium Dioxide Nanofilm”, the authors coated the D-shaped fiber coated with nanosized titanium dioxide (TiO₂) thin film as a sensing head to present a high sensitivity liquid refractive index sensor based on lossy mode resonance effect.

In the article entitled “Effect of Oxygen Flow Rate on the Optical, Electrical, and Mechanical Properties of DC Sputtering ITO Thin Films”, the authors found that the oxygen flow rate has significant influence on the electrical resistivity, residual stress, and surface roughness of the indium tin oxide (ITO) thin film, which is an important material in display technologies and organic electronics.

In the article entitled “Green LED as an Effective Light Source for Curing Acrylate-Based Dental Resins in Combination with Irgacure 784”, the possibility about using green light-emitting diode (LED) as the curing source for the dental resins based on the mixture of acrylate and photoinitiator Irgacure 784 was proposed. The mechanical properties were also investigated.

In the article entitled “Light Leakage of Multidomain Vertical Alignment LCDs Using a Colorimetric Model in the Dark State”, the authors proposed a colorimetric model to analyzing the colorimetric properties of liquid crystal displays (LCDs). With the aid of this model, the multidomain vertical alignment- (MVA-) type LCD module could be designed for less light leakage and thus improve the contrast ratio.

In the article entitled “Voltage-Controllable Guided Propagation in Nematic Liquid Crystals”, the propagation properties of a single beam in a planar nematic liquid crystals cell were discussed. On the basis of the results, the authors also demonstrated that the beam propagation can be easily coupled between two formed channels in the planar nematic liquid crystals cell by adjusting the applied voltage.

In the article entitled “Electrically Tunable Diffraction Grating Based on Liquid Crystals”, a liquid crystals cell with periodic electrodes was fabricated as an electrically tunable diffraction grating. The diffraction efficiency of the grating can be adjusted by adjusting the applied voltage or the polarization of the probe beam.

In the article entitled “Angle-Scanning Surface Plasmon Resonance System with 3D Printed Components for

Biorecognition Investigation”, the authors utilized the fused deposition modeling based three-dimensional printing technology to develop a rapid-prototyping surface plasmon resonance (SPR) system. The resolution of the proposed system can be as high as 6.4×10^{-6} RIU (refractive index unit).

In the article entitled “Optical Modeling Analysis of Red, Green, and Yellow Phosphors with a Blue LED”, the authors evaluated the luminous properties of red, green, and yellow phosphors with a blue LED and built a corresponding optical model, which can be a cross-reference for the design towards the better LED.

In the article entitled “Enhanced Photoluminescence in Gold Nanoparticles Doped Homogeneous Planar Nematic Liquid Crystals”, the authors reported that the photoluminescence of nematic liquid crystals can be enhanced with suitable amount of gold nanoparticles dopants and discussed the mechanism for the enhancement.

In the article entitled “Circular Polarization and Wavelength Selective Gratings Based on Holographic Cholesteric Liquid Crystal Templates”, the liquid crystal polymer template technique was adopted to develop diffraction gratings for specific circular polarization and wavelength. The authors also demonstrated that the diffraction efficiency of the grating can be electrically controlled.

The editors expect to attract more researchers involved in soft matter photonics via sharing the fruitful and fascinating special issue.

Conflicts of Interest

As the quest editorial team of this special issue, we declare that we have no financial and personal relationships with the authors of the manuscripts submitted to this special issue that can inappropriately influence our editorial work.

*Shuan-Yu Huang
Daniel Ho
Jia-De Lin*

Research Article

Circular Polarization and Wavelength Selective Gratings Based on Holographic Cholesteric Liquid Crystal Templates

Hsien-Kuo Chin,¹ Hui-Ying Kuo,^{2,3} Yang-Chen Zheng,⁴ Jia-De Lin ,⁴ and Chia-Rong Lee⁴

¹Division of Cardiovascular, Department of Surgery, Kaohsiung Armed Forces General Hospital, Kaohsiung 802, Taiwan

²Department of Optometry, Chung Shan Medical University, Taichung 402, Taiwan

³Department of Ophthalmology, Chung Shan Medical University Hospital, Taichung 402, Taiwan

⁴Department of Photonics, National Cheng Kung University, Tainan 701, Taiwan

Correspondence should be addressed to Jia-De Lin; geman1218@yahoo.com.tw

Received 6 May 2018; Revised 5 August 2018; Accepted 5 September 2018; Published 3 October 2018

Academic Editor: Jörg Fink

Copyright © 2018 Hsien-Kuo Chin et al. This is an open access article distributed under the Creative Commons Attribution License, which permits unrestricted use, distribution, and reproduction in any medium, provided the original work is properly cited.

Refilling cholesteric liquid crystal (CLC) template gratings with circular polarization, wavelength selectivity, and dual operation mode are first demonstrated. The gratings with template and nontemplate regions are obtained through the two-beam interfering photo-polymerization, washing-out, and refilling procedure. The refilling CLC has different chiral handedness (left or right) and reflection band (at green and red regions). When the wavelength of a probe beam is within the refilled CLC reflection band of the nontemplate region, the device works as an amplitude grating since the sample in the template and nontemplate regions reflects distinct colour region. In addition, the diffraction intensity of the grating can be electrically controlled. Therefore, this CLC-based device can be potentially used in controllable diffraction elements in optics.

1. Introduction

Cholesteric liquid crystal (CLC) is a soft matter with a self-organized helical structure and can be regarded as a one-dimensional photonic crystal [1]. It has multiple responses under various external stimuli and can thus be applied on tunable photonic devices, such as tunable optical filter [2], diffraction grating [3], mirror-less laser [4], microlens [5], and eye protector [6]. CLCs can exhibit various textures, including planar (uniformly standing helix), fingerprint (uniformly lying helix), and focal conic, depending on the orientation of the helical axes in CLCs. Fingerprint CLCs exhibit modulation of refractive index in lateral direction and are suitable for use in developing optical gratings. By embedding the photosensitive moieties or doping some of the additives with photosensitivity into the fingerprint CLC, the helical pitch of the fingerprint CLC can be compressed or extended by light irradiation and can function as an optically tunable diffraction grating [7].

The optically tunable diffraction grating can be used for beam control and wide-range spectral scanning applications

[7–9]. Fingerprint CLC can have the function of a tunable grating [10]. However, gratings based on fingerprint CLCs present no circular polarization selectivity, which is an attractive feature of CLCs. Therefore, gratings based on planar CLCs for diffracting circularly polarized light are developed in recent years [11–13]. Using holographic interference or a mask to generate a periodic distribution of light on photo-sensitive planar CLC-based materials leads to the periodic variations of CLC orientations and thus light diffraction [14, 15]. For example, a CLC grating can be fabricated via a spatial arrangement of the vertical and planar arrangement of the CLC molecules by two-beam interference [11]. A photo-induced surface relief phase grating can be realized on a photoresponsive CLC polymer film through the optical isomerization for reducing the molecular order parameters [12]. Polarization-selective CLC polymer gratings because of periodic phase modulation by phototunable helical pitch have also been demonstrated [13]. However, the planar CLC gratings based on photosensitive materials have stability issues. To improve the stability and functions of the planar CLC grating, a new type of CLC grating must be developed.

TABLE 1: Prescription of the refilled right-handed and left-handed CLC (RCLC and LCLC, respectively) materials. The indices of “red” and “green” behind RCLC or LCLC mean that the CLC materials reflect at red and green regions, respectively.

wt%	RCLC-red	RCLC-green	LCLC-red	LCLC-green
HTW114200-100	77	73	77	73
R811	23	27		
S811			23	27

In this work, optical gratings are fabricated on the basis of two-beam interference and fabrication technique of CLC template (washing-out/refilling) [16–18]. By refilling left- or right-handed CLC (LCLC and RCLC, respectively) into a right-handed CLC polymer template grating, the refilled CLC template grating can diffract light with specific wavelength. In addition, the refilled CLC template grating shows different diffraction efficiencies for left- and right-handed circular polarization (LCP and RCP, respectively) in reflection and transmission modes. The diffraction intensity can also be electrically controlled. The beam steering device exhibits electrical controllability and circular polarization and wavelength selectivity with dual operation modes.

2. Materials and Methods

The mixture used for fabricating CLC templates is composed of E7 (NLC, from Fusol-Material), R811 (right-handed chiral dopant, from Fusol-Material), R1011 (right-handed chiral dopant, from Fusol-Material), RMM691 (chiral monomer, from Merck), RMM257 (achiral diacrylate monomer, from Merck), and Irg184 (photoinitiator, from Pufeng). The weight ratio of these materials is 66.8:13:2:15.5:2.5:0.2. The uniform mixture was injected into an PVA-rubbed empty cell with a cell gap of 38 μm . Two UV laser beams from a He-Cd Laser (from Kimmon) were adjusted to construct an interference pattern on and cure the sample, resulting in a spatially periodic polymerized and nonpolymerized regions inside the sample. The cured sample was immersed in acetone for one day to wash-out the nonreactive materials. After evaporating the acetone, a dried grating with spatially periodic template and nontemplate regions was obtained. Last, another CLC material was then refilled into the grating to finish the fabrication of the refilling CLC template grating. In this paper, four types of refilled CLC materials composed of NLC (HTW114200-100, from Fusol-Material) and chiral dopants (S811 and R811, from Fusol-Material), as shown in Table 1, were prepared to refill into the sample. The four refilled CLCs are labelled as RCLC-red, RCLC-green, LCLC-red, and LCLC-green, in which “R” and “L” in front of CLC mean right- and left-handednesses of chirality, respectively, and “red” and “green” in the labels are the reflection bands at red and green regions, respectively.

As shown in Figure 1, one CW probe beam ($\lambda = 532$ nm or 633 nm) with right-handed or left-handed circular polarization was aligned to normally probe the refilling CLC template grating sample. Two photodetectors were used to measure the first-order diffraction efficiencies in the reflection and transmission modes of diffraction beams.

3. Results and Discussion

3.1. Refilled CLC Template Grating Samples with Various Refilled CLC Materials. As described in the previous section, the template grating was fabricated by refilling the CLC material (shown in Table 1) into the holographically cured sample with a grating spacing of about 7.3 μm . Two different regions are formed after refilling the CLC material into the sample, template, and nontemplate regions, which correspond to the constructive and destructive interference regions, respectively. Since the CLC cannot completely fill the nanopores of the template region, the reflection band of the refilled template region blue-shifts from its original state. The reflection band of the nontemplate region is attributed to the reflection of the refilled CLC. Therefore, the two regions can reflect at different colour regions. In other words, if a probe beam with a specific wavelength probes on the grating sample, the sample can be regarded as an amplitude grating. Given that the reflection of CLC is for a specific circular polarization, the refilled CLC template grating can be designed to reflect lights of a specific wavelength and circular polarization by refilling CLCs with different handednesses and reflection bands. For describing the circular polarization selectivity of the refilled template grating, a parameter called g -value is defined as [19]

$$g = \frac{2(\eta_L - \eta_R)}{(\eta_L + \eta_R)}, \quad (1)$$

where η_L and η_R represent left-handed and right-handed circularly polarized diffraction efficiencies, respectively. A positive g -value indicates that the diffraction efficiency with LCP is greater than that with RCP. Therefore, a large absolute g -value near 2 means a good circular polarization selectivity of the refilled CLC template grating.

Figure 2 shows the circular polarization selectivity of the template grating refilled with CLC material reflecting red light (RCLC-red and LCLC-red, reflection region: 590 nm–650 nm). When the refilled material is RCLC-red, the nontemplate region can reflect red RCP light but the template region reflects blue RCP light, which can be observed via the reflection spectrum shown in Figure 2(a). In the reflection mode, the diffraction efficiency of the RCP red light is greater than that of the LCP red light ($g = -1.14$) [Figure 2(a)]. On the contrary, the effect of the transmission mode is opposite to the reflection mode ($g = 1.38$) [Figure 2(b)]. If the wavelength of the probe beam is 532 nm, then the light cannot be reflected either by the template or the nontemplate region and thus should not experience an amplitude grating. However, the refractive index difference between the template

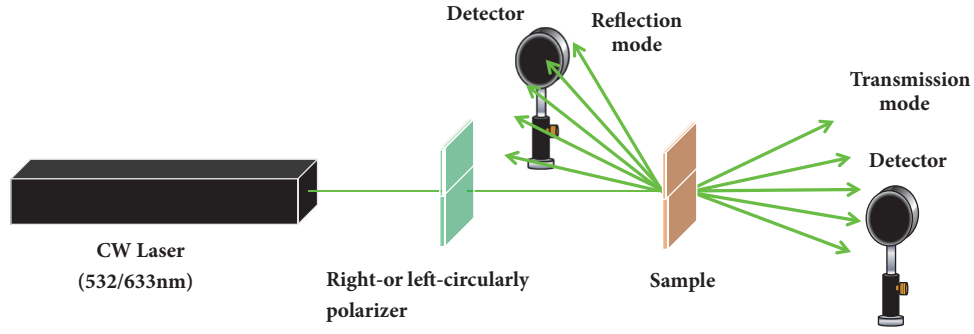


FIGURE 1: Setup for measuring the diffraction efficiencies of the refilled CLC template grating sample in reflection and transmission modes of diffraction beams.

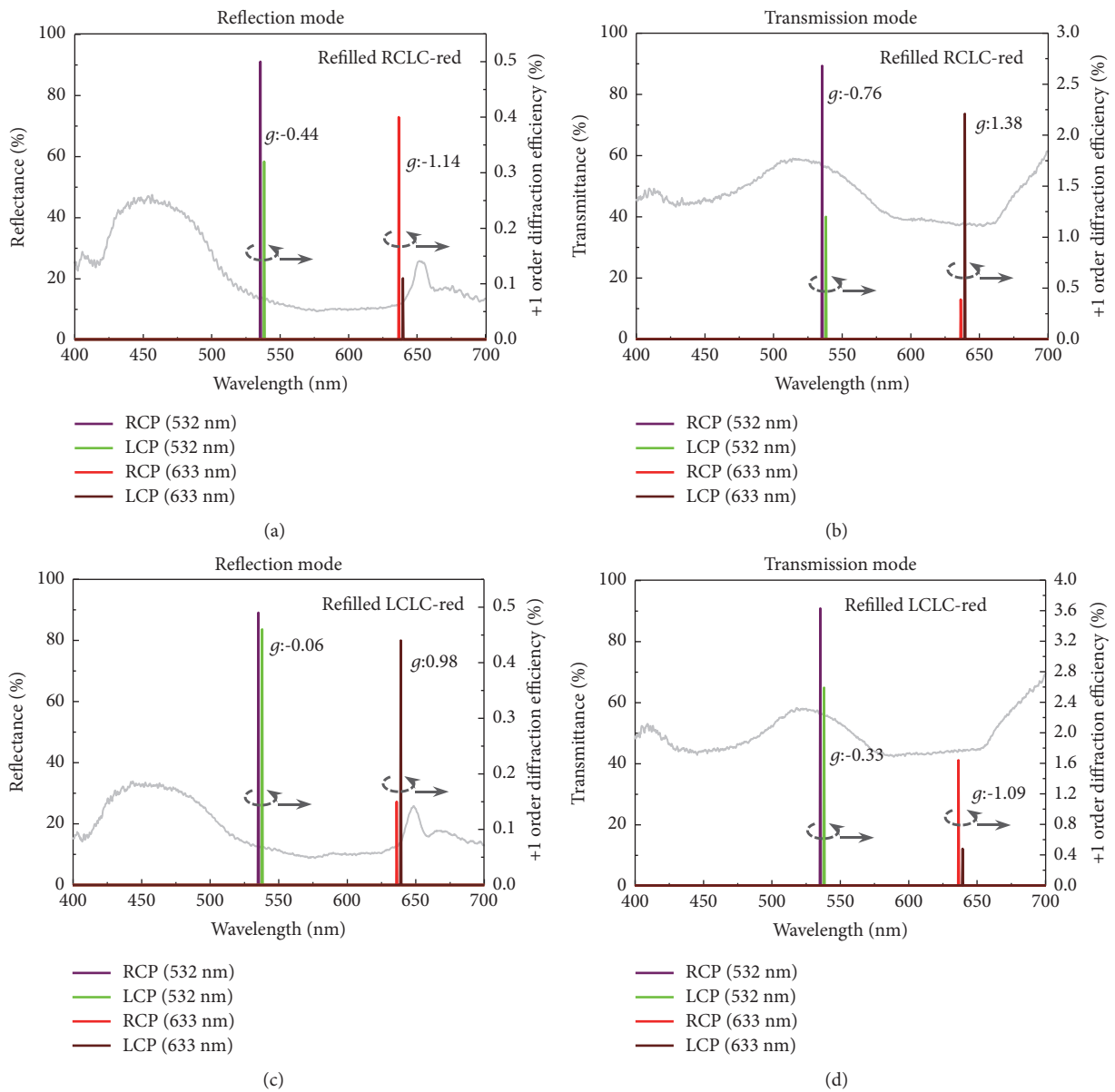


FIGURE 2: Measured +1 order diffraction efficiencies of the refilled CLC template grating in (a)/(c) reflection mode and (b)/(d) transmission mode by the RCP and LCP lights with the wavelengths of 532 and 632 nm, respectively. The refilled material is RCLC-red in (a)/(b) and LCLC-red in (c)/(d).

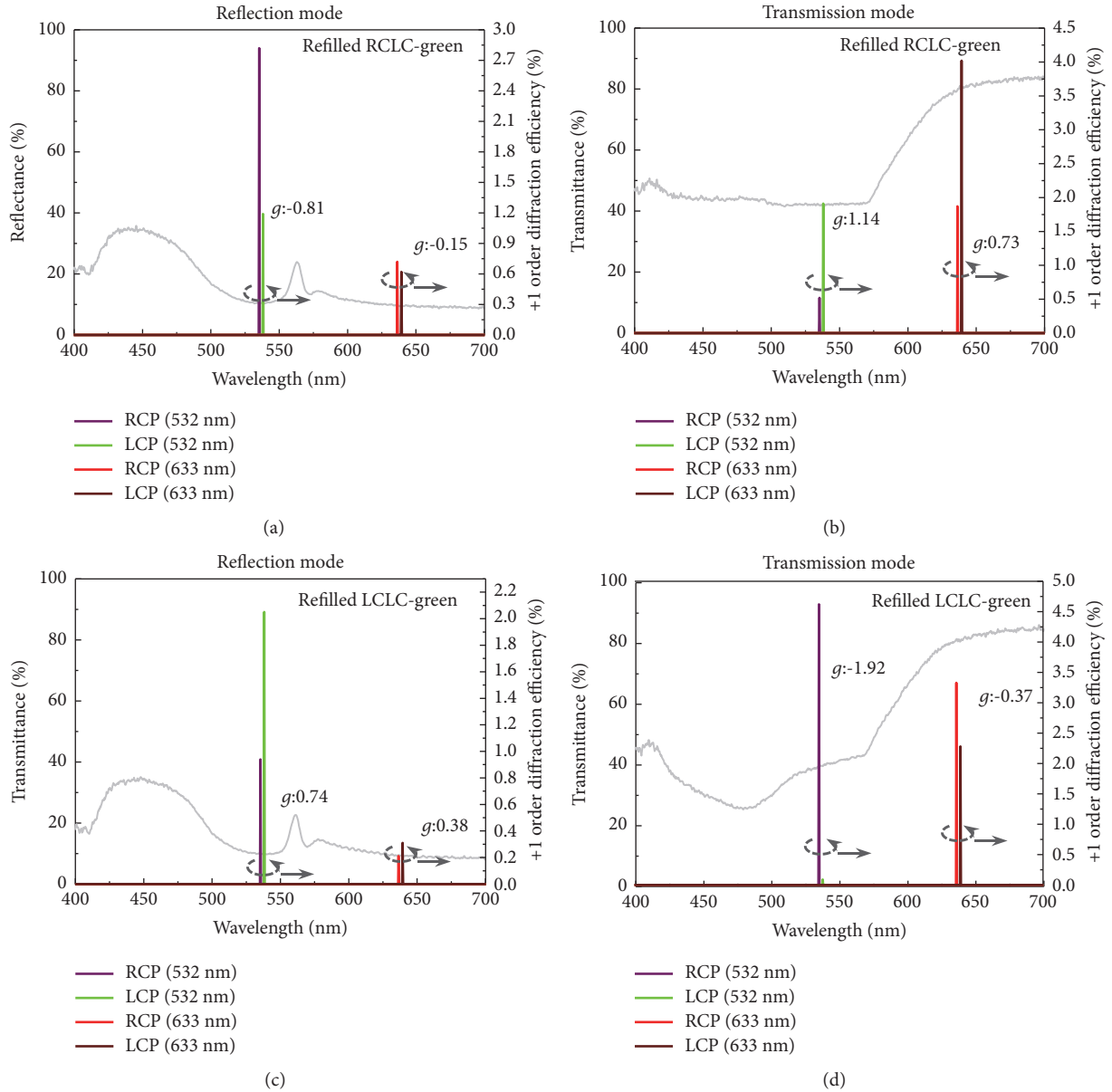


FIGURE 3: Measured +1 order diffraction efficiencies of the refilled CLC template grating in (a)/(c) reflection mode and (b)/(d) transmission mode by the RCP and LCP lights with the wavelengths of 532 and 632 nm, respectively. The refilled material is RCLC-green in (a)/(b) and LCLC-green in (c)/(d).

and nontemplate regions results in a slight effect of phase grating. Therefore, the green light can also be diffracted, but the absolute g -value is smaller than that of the red light. This condition represents no circular polarization selectivity for green light in this sample. When the LCLC-red is used as the refill material, the refilled CLC template grating sample exhibits two reflection bands in the blue and red regions, as shown in Figure 2(c). The properties of the refilled material are similar to RCLC-red, except for the opposite chirality. In the reflection mode, the diffraction efficiency of the RCP red light is smaller than that of the LCP red light ($g = 0.98$), as shown in Figure 2(c). On the contrary, the effect of the transmission mode is opposite to that of the reflection mode

($g = -1.09$), as shown in Figure 2(d). The absolute g -value in the green region is smaller than that in the red region, and no regular circular polarization selectivity occurs for green light in either the reflection or transmission mode. In other words, the polarization selectivity of the grating is only for red light when the refilled CLC reflects red light.

By refilling RCLC-green with reflection band in the green region (reflection region: 510–570 nm), the refilled CLC template grating causes the circular polarization selectivity of the green light. In the reflection mode, the diffraction efficiency of the RCP green light is greater than that of the LCP green light ($g = -0.81$), as shown in Figure 3(a). Conversely, the effect of the transmission mode is opposite

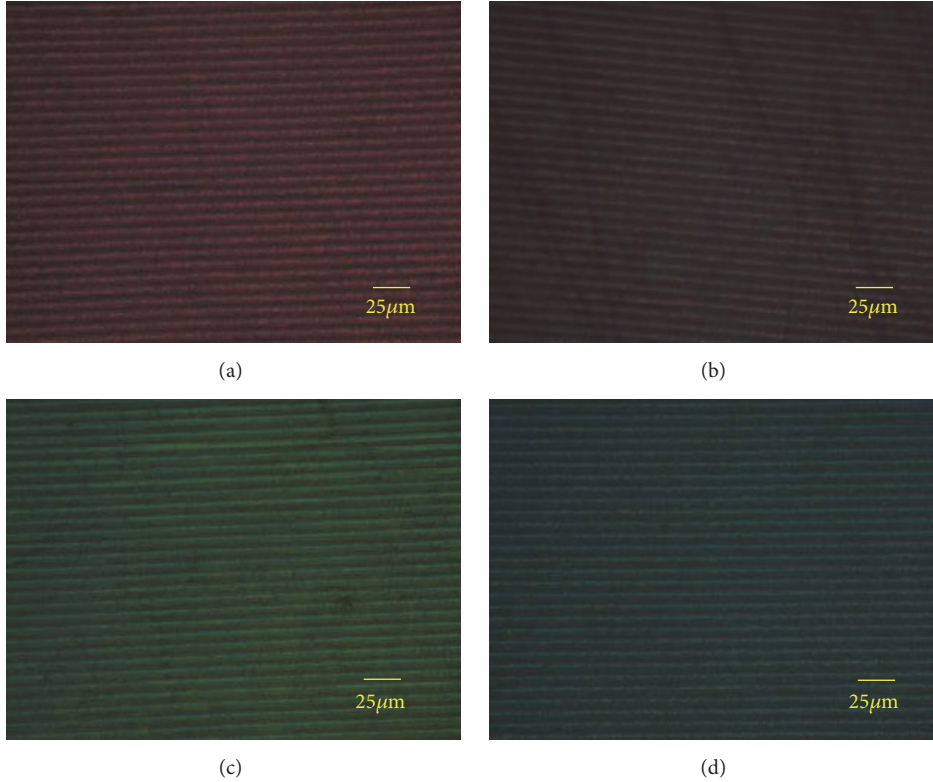


FIGURE 4: Reflected polarized optical microscopic image of the CLC polymer template gratings refilled with (a) RCLC-red, (b) LCLC-red, (c) RCLC-green, and (d) LCLC-green, respectively. The scale bar is 25 μm .

to that of the reflection mode ($g = 1.14$), as shown in Figure 3(b). When the refill material is LCLC-green, the refilled CLC template grating sample exhibits two reflection bands in the blue and green regions. The properties of the refilled material are similar to RCLC-green, except for the opposite chirality. In the reflection mode, the diffraction efficiency of the RCP green light is smaller than that of the LCP green light ($g = 0.74$), as shown in Figure 3(c). Conversely, the effect of the transmission mode is opposite to that of the reflection mode ($g = -1.92$), as shown in Figure 3(d). Figure 4 shows the reflected polarized optical microscopic images (with crossed polarizers) of the refilled template gratings discussed in Figures 2 and 3. In Figures 4(a) and 4(b), the red colour of the stripes is due to the reflection of the refilled red CLC materials, RCLC-red and LCLC-red. Similarly, the green stripes shown in Figures 4(c) and 4(d) are caused by reflection of the refilled green CLC materials.

Since the gratings in the work are fabricated by two-beam interference, the spatial distributions of refractive index and transmittance in the gratings can be expressed by a sinusoidal function. That is, the gratings can be regarded as sinusoidal transmittance gratings or sinusoidal phase gratings, depending on the experimental condition. If the incident light can be reflected by the CLC template or the refilled CLC, the sample is a sinusoidal transmittance grating. On the contrary, the sample can be regarded as a sinusoidal phase grating when the wavelength or polarization of the incident light does not match the reflection band or handedness of the CLC template

or the refilled CLC. For a sinusoidal transmittance grating, the first-order diffraction efficiency varies as the square of the amount of swing of the sinusoidal transmittance modulation Δt , and is given by the formula $\eta_t = (\Delta t/2)^2$. Because the maximum value of Δt is 0.5, the maximum value of the first diffraction efficiency is 6.25% ideally [20]. The experimental values are lower than the maximum theoretical value because the transmittance modulations of the refilled CLC template gratings are smaller than 0.5. For a sinusoidal phase grating, the first-order diffraction efficiency can be expressed by a first-order Bessel function of the phase modulation of the grating $\Delta\varphi$, that is, $\eta_p = J_1^2(\Delta\varphi)$. It means the diffraction efficiency of a sinusoidal phase grating can be ranged from 0 to 33.8%, depending on the value $\Delta\varphi$, which is related to the variation of the refractive indices and thickness of the grating [20]. Since the variation of the refractive indices of the refilled CLC template gratings and thus $\Delta\varphi$ is very small, the diffraction efficiency is not high. In addition, the scattering of light from the refilled CLC template grating is another factor for the low diffraction efficiency.

3.2. Electrically Controlled Diffraction of Refilled CLC Template Grating Sample. Considering that the arrangement of the refilled CLC can be changed by applying an electric field, the diffraction of the refilled CLC template grating can be controlled by AC electric field (1 kHz). As displayed in Figure 5, when the electric field is applied, the CLC in the nontemplate region can be converted from planer to

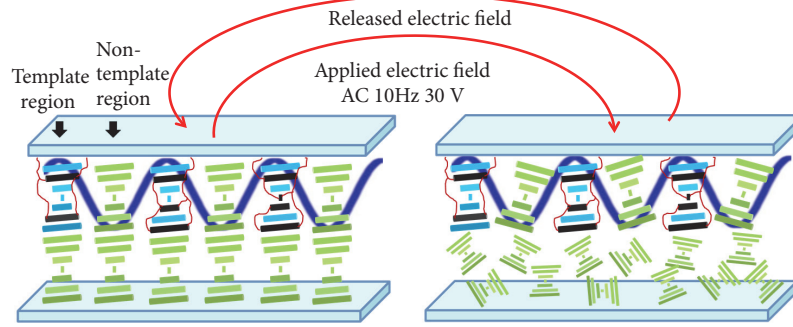


FIGURE 5: Schematic of conversion between planar and focal conic states in the refilled CLC template grating by the presence of an applied electric field.

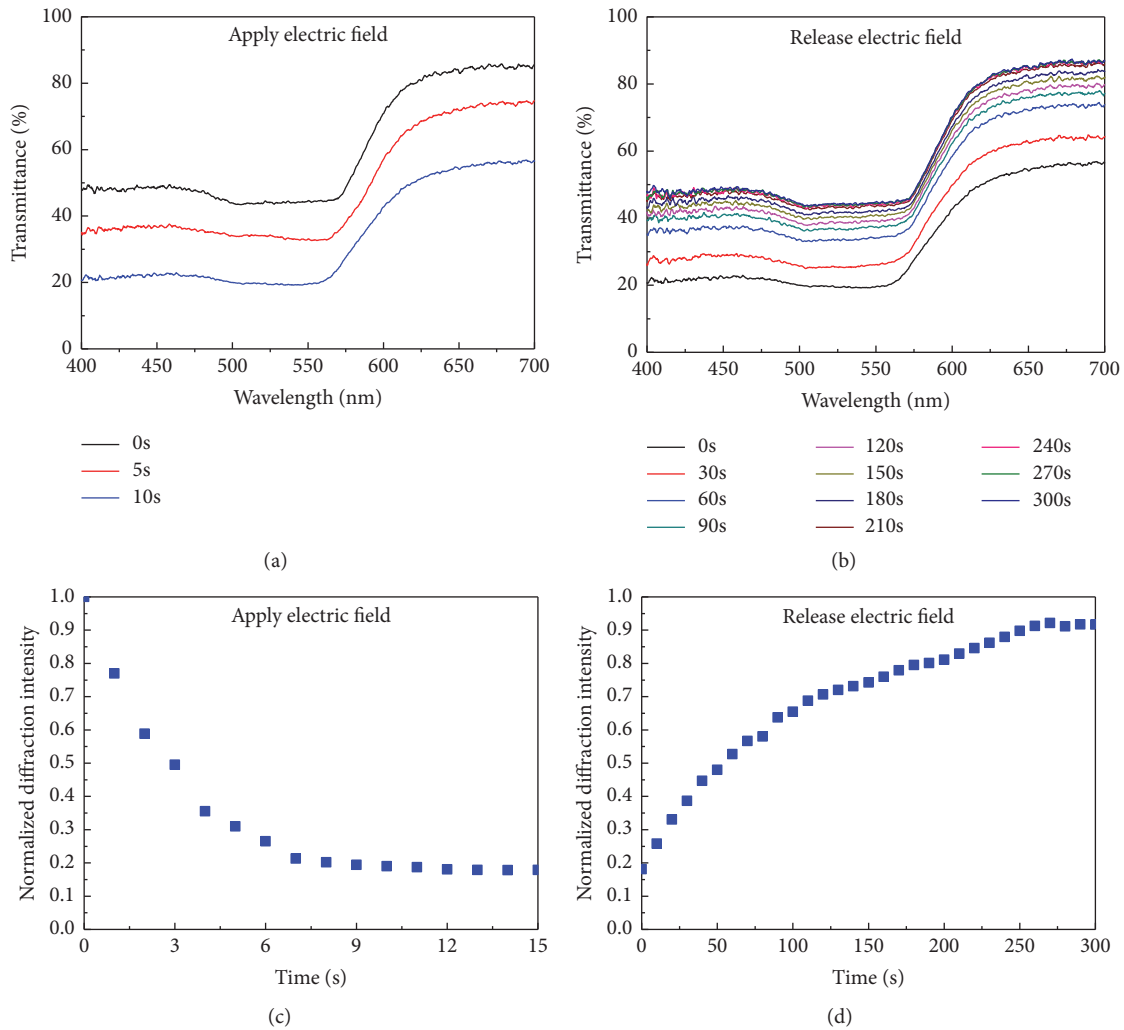


FIGURE 6: Dynamical variations of (a)/(b) the transmittance and (c)/(d) diffraction intensity of the refilled CLC template grating when (a, c) applying and (b, d) releasing the electric field.

focal conic state [21]. The refilled CLC in the nontemplate region will return from focal conic state to planer state when the electric field is released. The CLC molecules in the nontemplate region of the sample enter into a focal conic state when an electric field with 30 V is applied. The strong

scattering of the focal conic state gradually reduces the transmittance, as shown in Figure 6(a). When the electric field is removed, the transmittance gradually rises back to its initial state, as shown in Figure 6(b). The electrically controlled scattering and transmittance results in the variation of the

diffraction intensity with electric field [22]. Therefore, the diffraction intensity of the refilled CLC template grating can be controlled to decrease and increase with the electric field, as shown in Figures 6(c) and 6(d), respectively. In this work, the distance between the detector and the sample is 30 cm. The contrast ratio of the electrically switched diffraction can be higher if less scattered light is received by the detector, which can be achieved by increasing the distance between the detector and the sample.

4. Conclusions

In this paper, holographic interference is used to fabricate diffraction devices based on CLC polymer template gratings with circular polarization and wavelength selectivity. The refilled CLC template gratings can be operated in reflection and transmission modes. The diffractions of the reflection and transmission modes exhibit different circular polarization. By replacing the refilled CLC, the device can diffract light with specific circular polarization and wavelength. Finally, the electrical controllability of the device is demonstrated by switching the CLC texture between planar to focal conic states with an electric field.

Data Availability

The data used to support the findings of this study are available from the corresponding author upon request.

Conflicts of Interest

The authors declare that there are no conflicts of interest regarding the publication of this paper.

Authors' Contributions

Hsien-Kuo Chin and Hui-Ying Kuo contributed equally to this paper.

Acknowledgments

This research is financially supported by clinical research grants from Kaohsiung Armed Forces General Hospital, Taiwan [no. 105-14], and the Ministry of Science and Technology of Taiwan (Contract no. MOST 103-2112-M-006-012-MY3).

References

- [1] P. G. de Gennes and J. Prost, *The Physics of Liquid Crystals*, Oxford University Press, 1993.
- [2] M. Mitov and N. Dessaud, "Going beyond the reflectance limit of cholesteric liquid crystals," *Nature Materials*, vol. 5, no. 5, pp. 361–364, 2006.
- [3] S. P. Palto, L. M. Blinov, M. I. Barnik, V. V. Lazarev, B. A. Umanskii, and N. M. Shtykov, "Photonics of liquid-crystal structures: A review," *Crystallography Reports*, vol. 56, no. 4, pp. 622–649, 2011.
- [4] H. Coles and S. Morris, "Liquid-crystal lasers," *Nature Photonics*, vol. 4, no. 10, pp. 676–685, 2010.
- [5] P. Popov, L. W. Honaker, M. Mirheydari, E. K. Mann, and A. Jákli, "Chiral nematic liquid crystal microlenses," *Scientific Reports*, vol. 7, no. 1, 2017.
- [6] W. Zhang, L. Zhang, X. Liang et al., "Unconventional High-Performance Laser Protection System Based on Dichroic Dye-Doped Cholesteric Liquid Crystals," *Scientific Reports*, vol. 7, no. 1, 2017.
- [7] H.-C. Jau, Y. Li, C.-C. Li et al., "Light-driven wide-range nonmechanical beam steering and spectrum scanning based on a self-organized liquid crystal grating enabled by a chiral molecular switch," *Advanced Optical Materials*, vol. 3, no. 2, pp. 166–170, 2015.
- [8] I. Gvozdevskyy, O. Yaroshchuk, M. Serbina, and R. Yamaguchi, "Photoinduced helical inversion in cholesteric liquid crystal cells with homeotropic anchoring," *Optics Express*, vol. 20, no. 4, pp. 3499–3508, 2012.
- [9] H.-C. Jau, T.-H. Lin, R.-X. Fung, S.-Y. Huang, J.-H. Liu, and A. Y.-G. Fuh, "Optically-tunable beam steering grating based on azobenzene doped cholesteric liquid crystal," *Optics Express*, vol. 18, no. 16, pp. 17498–17503, 2010.
- [10] L.-L. Ma, W. Duan, M.-J. Tang et al., "Light-driven rotation and pitch tuning of self-organized cholesteric gratings formed in a semi-free film," *Polymer*, vol. 9, no. 7, p. 295, 2017.
- [11] A. Ryabchun, A. Bobrovsky, Y. Gritsai, O. Sakhno, V. Shibaev, and J. Stumpe, "Stable selective gratings in LC polymer by photoinduced helix pitch modulation," *ACS Applied Materials & Interfaces*, vol. 7, no. 4, pp. 2554–2560, 2015.
- [12] P.-Z. Sun, Z. Liu, W. Wang et al., "Light-reconfigured waveband-selective diffraction device enabled by micro-patterning of a photoresponsive self-organized helical superstructure," *Journal of Materials Chemistry C*, vol. 4, no. 39, pp. 9325–9330, 2016.
- [13] D. Liu, C. W. M. Bastiaansen, J. M. J. Den Toonder, and D. J. Broer, "Light-induced formation of dynamic and permanent surface topologies in chiral-nematic polymer networks," *Macromolecules*, vol. 45, no. 19, pp. 8005–8012, 2012.
- [14] L. De Sio, S. Serak, N. Tabiryan, S. Ferjani, A. Veltri, and C. Umetsu, "Composite holographic gratings containing light-responsive liquid crystals for visible bichromatic switching," *Advanced Materials*, vol. 22, no. 21, pp. 2316–2319, 2010.
- [15] H. Yeh, G. Chen, C. Lee, and T. Mo, "Optically switchable biphotonic gratings based on dye-doped cholesteric liquid crystal films," *Applied Physics Letters*, vol. 90, no. 26, p. 261103, 2007.
- [16] J. Guo, H. Cao, J. Wei et al., "Polymer stabilized liquid crystal films reflecting both right- and left-circularly polarized light," *Applied Physics Letters*, vol. 93, no. 20, p. 201901, 2008.
- [17] J.-D. Lin, C.-L. Chu, H.-Y. Lin et al., "Wide-band tunable photonic bandgaps based on nematic-refilling cholesteric liquid crystal polymer template samples," *Optical Materials Express*, vol. 5, no. 6, pp. 1419–1430, 2015.
- [18] J.-D. Lin, H.-L. Lin, H.-Y. Lin et al., "Widely tunable photonic bandgap and lasing emission in enantiomorphic cholesteric liquid crystal templates," *Journal of Materials Chemistry C*, vol. 5, no. 13, pp. 3222–3228, 2017.
- [19] A. Bobrovsky, K. Mochalov, V. Oleinikov et al., "Optically and electrically controlled circularly polarized emission from cholesteric liquid crystal materials doped with semiconductor quantum dots," *Advanced Materials*, vol. 24, no. 46, pp. 6216–6222, 2012.
- [20] S. A. Benton and V. M. Bove, *Holographic Imaging*, John Wiley & Sons, Inc., Hoboken, NJ, USA, 2008.

- [21] C. Wang and T. Lin, "Bistable reflective polarizer-free optical switch based on dye-doped cholesteric liquid crystal [Invited]," *Optical Materials Express*, vol. 1, no. 8, p. 1457, 2011.
- [22] Y.-C. Zheng, *ircular-polarization and wavelength selective gratings based on polymer templates of holographic cholesteric liquid crystal [Master, thesis]*, National Cheng Kung University, 2017.

Research Article

Enhanced Photoluminescence in Gold Nanoparticles Doped Homogeneous Planar Nematic Liquid Crystals

Chi-Huang Chang,^{1,2} Rong-Ji Lin,^{3,4} Chuen-Lin Tien ,^{3,5} and Shang-Min Yeh ⁶

¹Department of Ophthalmology, Chung Shan Medical University Hospital, Taichung 402, Taiwan

²Department of Medicine, Chung Shan Medical University, Taichung 402, Taiwan

³Ph.D. Program of Electrical and Communications Engineering, Feng Chia University, Taichung 40724, Taiwan

⁴Department of Optometry, Da-Yeh University, Changhua 515, Taiwan

⁵Department of Electrical Engineering, Feng Chia University, Taichung 40724, Taiwan

⁶Department of Optometry, Central Taiwan University of Science and Technology, Taichung 40601, Taiwan

Correspondence should be addressed to Shang-Min Yeh; optom.yap@gmail.com

Received 7 May 2018; Accepted 19 July 2018; Published 5 August 2018

Academic Editor: Daniel Ho

Copyright © 2018 Chi-Huang Chang et al. This is an open access article distributed under the Creative Commons Attribution License, which permits unrestricted use, distribution, and reproduction in any medium, provided the original work is properly cited.

This study reported the photoluminescence (PL) of gold nanoparticles (GNPs) doped planar nematic liquid crystals (NLCs) and observed around 64% enhancement in PL intensity with suitable doping amounts of GNPs in liquid crystals 5CB. The enhancement in PL intensity has been attributed to the increased surface area from GNPs, which results in increased emissions due to the increased scattering of excitation. The subsequent decay of PL intensity with doping more amounts of GNPs in liquid crystals 5CB was due to the aggregation of the GNPs, which resulted in decayed emissions due to the decay of the scattering of excitation. The concentration and the size of GNPs, as well as the orientation of the LCs' director, with respect to the excitation, which depend on the intensity of the PL, were also investigated.

1. Introduction

Research in the field of liquid crystals (LCs) has developed due to its imposing properties [1–4], especially, the physical and chemical properties, which are widely applied in liquid-crystal displays (LCDs). The main drawback of liquid-crystal displays (LCDs) is low brightness, which is due to the use of absorbing color filters and dichroic sheet polarizers. The luminescence of LCD is a possible method to improve the low brightness issue [5–7]. The problem of making a luminescent LCD is that light emissions in the visible region of the electromagnetic spectrum are lessened by using pure LC materials [8–10]. The enhanced luminescence of the LC materials may definitely realize the emissive LCDs [11–13]. Doping metal materials or metal nanoparticles (NPs) in LCs have attracted much attention due to the enhanced electro-optical properties of the doped LC materials. Palewska et al. investigated the influence of electric field on photoluminescence of lanthanide-doped nematic liquid crystals and obtained a highly resolved luminescence and luminescence

excitation spectra [14]. Kumar et al. reported the characterization and photoluminescence (PL) in gold nanoparticles doped ferroelectric liquid crystals and obtained enhancement in PL intensity [3]. Kuo et al. reported the enhancement of photoluminescence (PL) intensity of NLC doped with silver NPs [15]. Tanabe et al. reported the full-color tunable photoluminescent ionic liquid crystals based on tripodal pyridinium, pyrimidinium, and quinolinium salts [16]. Lu et al. reported the electrically switchable photoluminescence of fluorescent-molecule-dispersed liquid crystals [17]. This study investigates photoluminescence (PL) in GNPs doped homogeneous planar NLCs and obtains about 64% enhancement in PL intensity with doping suitable amounts of GNPs in liquid crystals 5CB.

2. Preparation of Sample and Experimental Setup

The materials adopted in this work are nematic LCs (NLCs), 5CB (from Merck), and GNPs with diameters of 13 nm,

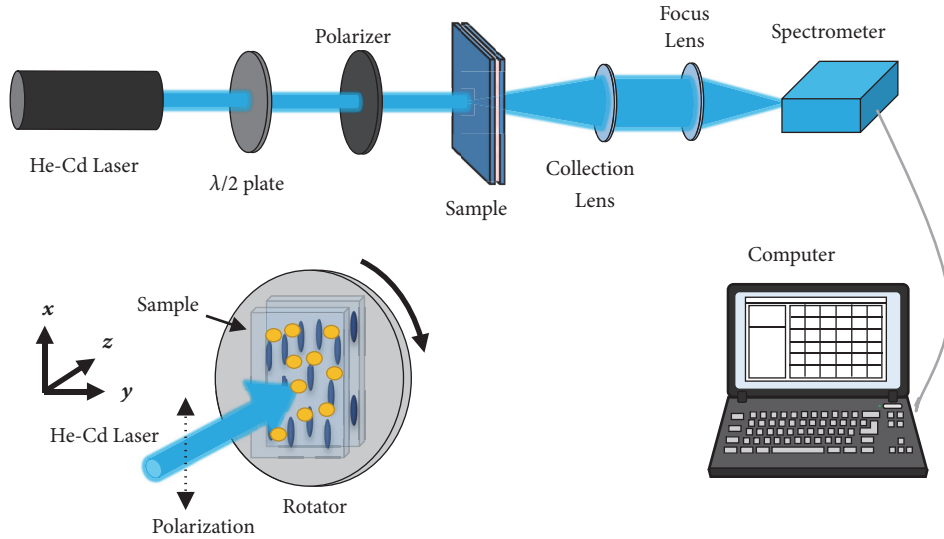


FIGURE 1: Experimental setup for measuring the PL spectra of the enhanced photoluminescence in GNPs doped homogeneous planar NLCs.

32 nm, and 56 nm (the concentrations of GNPs are $5 \cdot 10^9$ particles/ml, $9 \cdot 10^9$ particles/ml, $1.3 \cdot 10^{10}$ particles/ml, $1.8 \cdot 10^{10}$ particles/ml, and $2.5 \cdot 10^{10}$ particles/ml). These materials are uniformly mixed and capillary injected into the sample cell, which is assembled from two indium-tin-oxide-coated glass slides separated by two $5.4 \mu\text{m}$ -thick plastic spacers. The homogeneous planar alignment of the NLCs is accomplished unidirectionally by rubbing polyimide on the inner surfaces of the two glass substrates.

Figure 1 depicts the experimental setup for the investigation of the enhanced photoluminescence in GNPs doped homogeneous planar NLCs, where the CW helium-cadmium laser (wavelength: 325 nm, power: 1 mW) is focused on the sample cell. A half-wave plate ($\lambda/2$ for 325 nm) and a polarizer are placed in front of the sample cell to maintain the excitation power of 1 mW, the polarization of the excitation beam is fixed parallel to the x-axis, and the director of the NLCs is rotated every 15 degrees from x-axis (0 degree) to y-axis (90 degree). The spectra of photoluminescence (PL) are measured with a spectrometer and analyzed by computer.

3. Results and Discussions

Figure 2 shows the experimental absorption and fluorescence emission spectra of the pure NLCs cell (without doping GNPs). The absorption spectrum covered from 288 to 340 nm and the photoluminescence spectrum was recorded from 350 nm to 500 nm, respectively. The maxima of the absorption and fluorescence emissions are about 321 and 394 nm, respectively. The inset of Figure 2 shows the image of the fluorescence emission under the pumped helium-cadmium laser, which is operated at 325 nm.

Figure 3 shows the photoluminescence spectra of GNPs doped homogeneous planar NLCs, where the concentrations of GNPs are $5 \cdot 10^9$ particles/ml, $9 \cdot 10^9$ particles/ml, $1.3 \cdot 10^{10}$ particles/ml, $1.8 \cdot 10^{10}$ particles/ml, and $2.5 \cdot 10^{10}$ particles/ml, respectively; and the gold nanoparticle size is 13 nm in

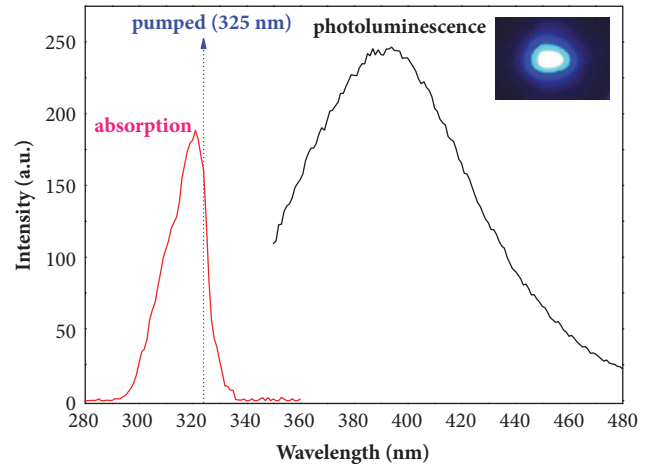


FIGURE 2: The experimental absorption and fluorescence emission spectra of the pure NLCs cell and the image of the fluorescence emission under the pumped helium-cadmium laser operated at 325 nm.

diameter. Figure 3(a) shows that the PL intensity gradually increased with the increased amount of GNPs per ml in NLCs. In the pure NLCs, the peak value of the PL intensity is around 250.4; the peak values of PL intensities are 303.5, 324.4, and 372.8, respectively, which correspond to doping GNPs with the concentrations of $5 \cdot 10^9$ particles/ml, $9 \cdot 10^9$ particles/ml, and $1.3 \cdot 10^{10}$ particles/ml. The ratio between the maximum and minimum of peak intensity is ~ 1.49 , meaning 49% enhancement in PL intensity with suitable concentrations of $1.3 \cdot 10^{10}$ particles/ml.

Figure 3(b) shows that PL intensity gradually decayed with the increased amount of GNPs per ml in NLCs. The peak values of PL intensity are 372.8, 319.3, and 275.0, respectively, which correspond to doping GNPs with concentrations of $1.3 \cdot 10^{10}$ particles/ml, $1.8 \cdot 10^{10}$ particles/ml, and $2.5 \cdot 10^{10}$ particles/ml.

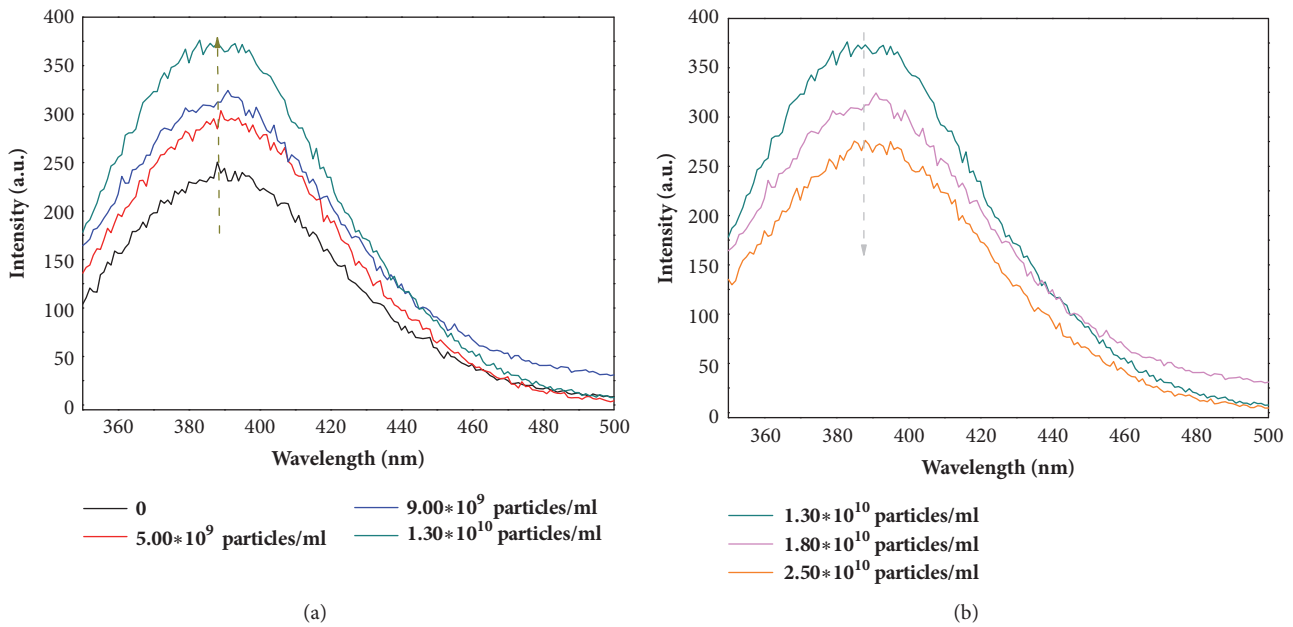


FIGURE 3: The photoluminescence spectra of GNPs doped homogeneous planar NLCs, where the concentrations of GNPs are (a) 0 , 9×10^9 , and 1.3×10^{10} particles/ml, respectively, and (b) 1.3×10^{10} , 1.8×10^{10} , and 2.5×10^{10} particles/ml, respectively, and the gold nanoparticle size is 13 nm in diameter.

The enhancement of photoluminescence intensity is attributed to the increased surface area from the GNPs, which strengthens the multiple reflections of the excitation beam and results in the local surface plasmon resonance effect. This effect becomes more obvious with suitable doping concentrations of GNPs in the NLCs (NLCs). The decay of PL intensity is attributed to the aggregation of the GNPs, which cause the surface area to decrease, resulting in the reduction of the energy transfer effect between NLCs and GNPs, and this effect leads to the decrease of PL intensity.

Figure 4 shows the peak intensity of PL emissions versus concentrations of GNPs with diameter sizes of 13 nm, 32 nm, and 56 nm. The peak intensity of the PL emission gradually increases in the range of concentration from 0 (pure NLCs) to 1.3×10^{10} particles/ml. The fluorescence is enhanced by the scattering of the excitation beam due to the increased surface area of GNPs. At the same concentration of gold nanoparticles (lower than 1.3×10^{10} particles/ml), the peak intensity of PL emission is stronger for 13 nm gold particles. This is because the smaller nanoparticles have larger surface areas, which causes the multiple reflections and scattering of the excitation beam. As the concentration of GNPs is larger than 1.3×10^{10} particles/ml, the peak intensity of the PL emission for a diameter size of 13 nm gradually decreases; instead, it increases the PL emissions for 32 nm and 56 nm. The smaller nanoparticles are aggregated, which reduces the surface areas, and aggregation may disrupt the ordering state of the liquid-crystal alignment. The increasing PL emissions for 32 nm and 56 nm diameters are due the gradually increased surface areas, which result in multiple reflections and scattering of the excitation beam. For GNPs of 32 nm, the peak intensity of the PL emission gradually decays as the concentration of GNPs becomes larger than 1.8×10^{10} particles/ml. This is

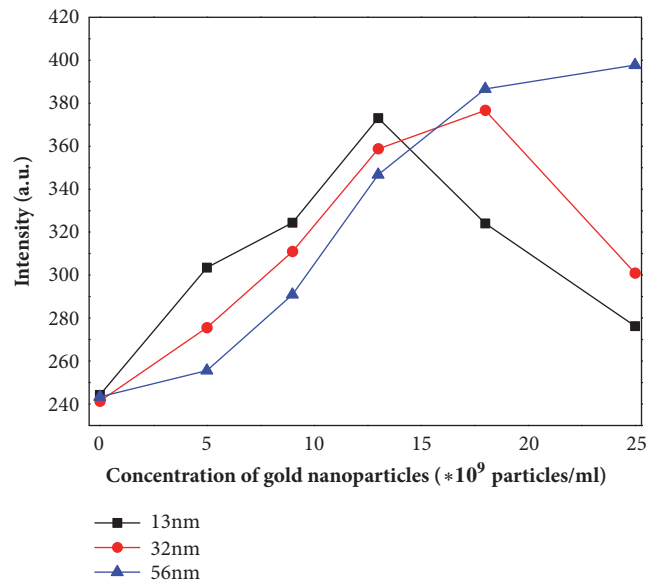


FIGURE 4: The peak intensity of PL emission versus concentrations of GNPs with diameter sizes of 13 nm, 32 nm, and 56 nm.

because the aggregation of the nanoparticles reduces PL intensity. For GNPs of 32 nm, the peak intensity gradually increases with the increased concentration of GNPs; thus, decreased PL emissions can be expected, as the concentration of nanoparticles is sufficient.

Figure 5 shows the peak intensity of the PL emission of pure NLCs and doping GNPs versus the rotational degree of NLCs' director, where the concentration of GNPs is 1.3×10^{10} particles/ml. The polarization of the excitation beam is fixed parallel to the x-axis, and the director of the NLCs is rotated

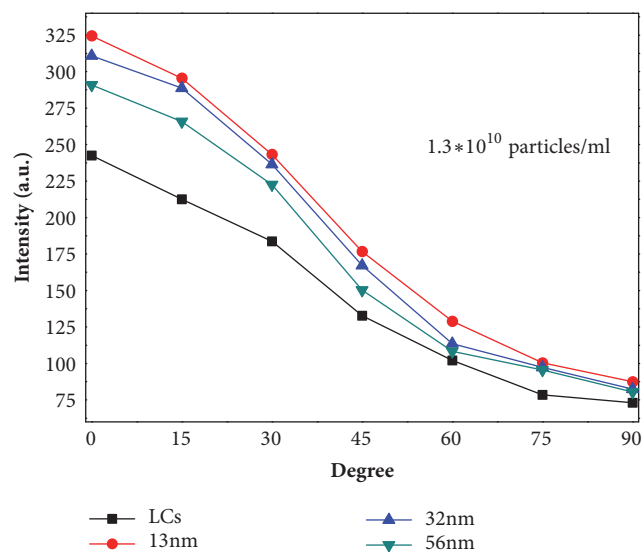


FIGURE 5: The peak intensity of PL emissions of pure NLCs and doping GNPs versus the rotational degree of NLCs' director, where the concentration of GNPs is 1.3×10^{10} particles/ml.

every 15 degrees from the x-axis (0 degree) to the y-axis (90 degree). All peak intensities for gold nanoparticles doping NLCs are stronger than pure NLCs, as the rotational degree is smaller than 45° . As the rotational degree gradually increases to 90° , all peak intensities decay to a similar value. The ratio between the absorption of NLCs in the x- and y-axis, denoted as A_{0°/A_{90° , is around 3.21, and the ratio between the PL intensity in the x- and y-axis, denoted as $PL_{0^\circ}/PL_{90^\circ}$, is around 3.32. These results show that the absorption of the liquid crystal critically dominates PL intensity. However, the A_{0°/A_{90° is decreased; instead, the $PL_{0^\circ}/PL_{90^\circ}$ is increased by adding gold nanoparticles in the NLCs. This result shows that the doping of GNPs causes the reduction of the ordering state of NLCs, resulting in decreased absorption. As the added GNPs provide more scattering surface area, it results in the enhancement of PL intensity.

4. Conclusions

This work investigated the photoluminescence (PL) of the GNPs doped planar NLCs. The PL intensity gradually increased with the increased amount of GNPs per ml in NLCs. The results show 64% enhancement in PL intensity with doping suitable amounts of GNPs in liquid crystals 5CB. The enhanced PL intensity is attributed to the increased surface area from the GNPs, resulting in increased emissions due to the increase of the scattering of excitation. The subsequent decay of PL intensity was attributed to the aggregation of the GNPs, as it caused decreased surface area, resulting in the reduction of the energy transfer effect between NLCs and GNPs. The size effect of GNPs was discussed, and the results show that the peak intensity of PL emission was stronger for the 13 nm gold particles at the same concentration of gold nanoparticles (lower than 1.3×10^{10} particles/ml). This is because the smaller nanoparticles have larger surface area, which causes multiple reflections and scattering of the

excitation beam. By rotating the LCs' director, the results show that the absorption of the liquid crystal and the increased surface area critically dominate PL intensity.

Data Availability

The data used to support the findings of this study are included within the article.

Conflicts of Interest

The authors declare that they have no conflicts of interest.

Acknowledgments

This study was financially supported by Chung Shan Medical University Hospital (Contract no. CSH-2017-C-010).

References

- [1] G. H. Brown, *Advances in Liquid Crystals*, Academic Press, London, UK, 444th edition, 1976.
- [2] M. Čopič, J. E. Maclennan, and N. A. Clark, "Structure and dynamics of ferroelectric liquid crystal cells exhibiting thresholdless switching," *Physical Review E: Statistical, Nonlinear, and Soft Matter Physics*, vol. 65, no. 2, 2002.
- [3] A. Kumar, J. Prakash, D. S. Mehta, A. M. Biradar, and W. Haase, "Enhanced photoluminescence in gold nanoparticles doped ferroelectric liquid crystals," *Applied Physics Letters*, vol. 95, no. 2, p. 023117, 2009.
- [4] D. P. Singh, S. K. Gupta, T. Vimal, and R. Manohar, "Dielectric, electro-optical, and photoluminescence characteristics of ferroelectric liquid crystals on a graphene-coated indium tin oxide substrate," *Physical Review E: Statistical, Nonlinear, and Soft Matter Physics*, vol. 90, no. 2, Article ID 022501, 2014.
- [5] L. Calucci, G. Ciofani, D. De Marchi et al., "Boron nitride nanotubes as T 2-weighted MRI contrast agents," *The Journal of Physical Chemistry Letters*, vol. 1, no. 17, pp. 2561–2565, 2010.
- [6] F. V. Podgornov, A. M. Suvorova, A. V. Lapanik, and W. Haase, "Electrooptic and dielectric properties of ferroelectric liquid crystal/single walled carbon nanotubes dispersions confined in thin cells," *Chemical Physics Letters*, vol. 479, no. 4-6, pp. 206–210, 2009.
- [7] Y.-S. Ha, H.-J. Kim, H.-G. Park, and D.-S. Seo, "Enhancement of electro-optic properties in liquid crystal devices via titanium nanoparticle doping," *Optics Express*, vol. 20, no. 6, pp. 6448–6455, 2012.
- [8] Y. P. Piryatinskii and O. V. Yaroshchuk, "Photoluminescence of pentyl-cyanobiphenyl in liquid-crystal and solid-crystal states," *Optics and Spectroscopy*, vol. 89, no. 6, pp. 860–866, 2000.
- [9] J. W. Y. Lam, Y. Dong, J. Luo, K. K. L. Cheuk, Z. Xie, and B. Z. Tang, "Synthesis and photoluminescence of liquid crystalline poly(1-alkynes)," *Thin Solid Films*, vol. 417, no. 1-2, pp. 143–146, 2002.
- [10] Y. P. Piryatinskii, O. V. Yaroshchuk, L. A. Dolgov, T. V. Bidna, and D. Enke, "Photoluminescence of liquid-crystal azo derivatives in nanopores," *Optics and Spectroscopy*, vol. 97, no. 4, pp. 537–542, 2004.
- [11] S. Kaur, S. P. Singh, A. M. Biradar, A. Choudhary, and K. Sreenivas, "Enhanced electro-optical properties in gold nanoparticles

- doped ferroelectric liquid crystals,” *Applied Physics Letters*, vol. 91, no. 2, p. 023120, 2007.
- [12] T. Härtung, P. Reichenbach, and L. M. Eng, “Near-field coupling of a single fluorescent molecule and a spherical gold nanoparticle,” *Optics Express*, vol. 15, no. 20, pp. 12806–12817, 2007.
- [13] J. Zhang and J. R. Lakowicz, “Enhanced luminescence of phenyl-phenanthridine dye on aggregated small silver nanoparticles,” *The Journal of Physical Chemistry B*, vol. 109, no. 18, pp. 8701–8706, 2005.
- [14] K. Palewska, A. Miniewicz, S. Bartkiewicz, J. Legendziewicz, and W. Strek, “Influence of electric field on photoluminescence of lanthanide-doped nematic liquid crystal,” *Journal of Luminescence*, vol. 124, no. 2, pp. 265–272, 2007.
- [15] S.-Y. Huang, C.-C. Peng, L.-W. Tu, and C.-T. Kuo, “Enhancement of luminescence of nematic liquid crystals doped with silver nanoparticles,” *Molecular Crystals and Liquid Crystals*, vol. 507, pp. 301–306, 2009.
- [16] K. Tanabe, Y. Suzui, M. Hasegawa, and T. Kato, “Full-color tunable photoluminescent ionic liquid crystals based on tripodal pyridinium, pyrimidinium, and quinolinium salts,” *Journal of the American Chemical Society*, vol. 134, no. 12, pp. 5652–5661, 2012.
- [17] H. Lu, L. Qiu, G. Zhang et al., “Electrically switchable photoluminescence of fluorescent-molecule-dispersed liquid crystals prepared via photoisomerization-induced phase separation,” *Journal of Materials Chemistry C*, vol. 2, no. 8, pp. 1386–1389, 2014.

Research Article

Optical Modeling Analysis of Red, Green, and Yellow Phosphors with a Blue LED

Wen-Shing Sun¹ and Chuen-Lin Tien² 

¹Department of Optics and Photonics, National Central University, Chungli 32001, Taiwan

²Department of Electrical Engineering, Feng Chia University, Taichung 40724, Taiwan

Correspondence should be addressed to Chuen-Lin Tien; cltien@fcu.edu.tw

Received 21 January 2018; Accepted 12 March 2018; Published 1 August 2018

Academic Editor: Shuan-Yu Huang

Copyright © 2018 Wen-Shing Sun and Chuen-Lin Tien. This is an open access article distributed under the Creative Commons Attribution License, which permits unrestricted use, distribution, and reproduction in any medium, provided the original work is properly cited.

The luminous properties of red, green, and yellow phosphors with a blue LED are evaluated and a corresponding optical model is constructed using the optical simulation software LightTools®. According to the phosphor particle model, the desired chromaticity coordinate of the multicomponent light which is excited by a blue LED can be achieved by modifying the weight concentration of the phosphors. A comparison of the four types of LED package modules tested shows that the yellow phosphor encapsulated with a semispherical module takes up a lesser percentage of the total weight percentage of a constructed white light with a correlated color temperature of around 4000 K. The simulation and experimental results provide a cross-reference for better packaging and encapsulating designs for lumen improvement.

1. Introduction

The white light LED has become a popular choice to replace traditional lighting sources. Compared to incandescent and fluorescent lamps, white LEDs have many advantages, such as a long lifetime, high efficiency, and lower energy consumption [1]. Most white LEDs use phosphors excited by diode chips with short wavelengths (blue or violet) to reemit a broad spectrum light with a good color-rendering index [2–4]. Since the optical performance of LED lighting, including the correlated color temperature (CCT) values, is strongly dependent on the thickness, combination concentration, and geometrical distribution of the phosphors, the commercially available recipes for white LEDs usually require careful manipulation if they are to meet the CCT requirements. Any modification to the pattern of the package could change the volume, density, concentration, or uniformity of the luminescent phosphor film and cause variations in the CCT, chromaticity coordinates, and luminous efficacy.

To empirically determine the factors that dominate the optical properties of the white light LED, detailed experiments must be carried out. In terms of time savings and cost effectiveness, a proper optical model of phosphors is most

beneficial in reducing the trial-and-error process. In order to establish an LED model, experiments and simulations dealing with the relationships between the encapsulants, package structures, performance of the radiation power spectrum, CCT, and chromaticity coordinates must be conducted and the results analyzed. Further, some special LED package designs with higher uniformity but using lesser phosphor can be considered as an adjunct of the proposed model [5]. Yang et al. [6] demonstrated the accuracy feedback method of chromaticity coordinates and spectra. This feedback coating method offers an easy approach towards optimized spectra. Wang and Huang [7] also reported the chromaticity coordinates and spectra of phosphor-converted LEDs are well controlled by the feedback coating method. Our phosphor particle model was designed to simulate the scattering and absorbing process of light inside the phosphors. This model was based on the Mie theory, the ray tracing method, and Monte-Carlo algorithms [8–11]. A blue light LED was used to excite the phosphors, with the samples numbered R-645 and R-626 indicating red lights, G-531 and G-529 indicating green lights, and Y-561 yellow light. The number of the samples indicates the peak value of the emission spectrum in nanometers produced by the phosphor. For example, the

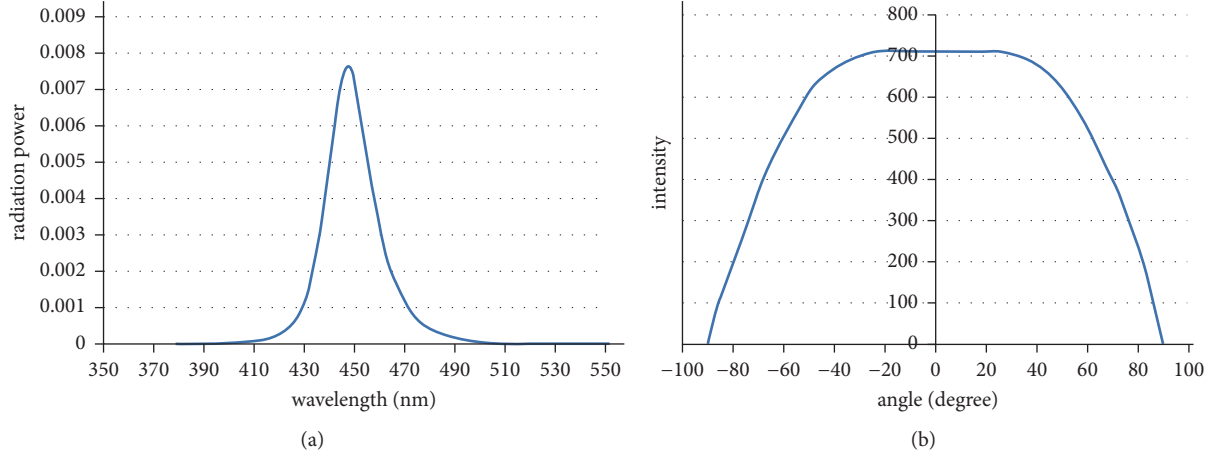


FIGURE 1: (a) Radiation power spectrum and (b) luminous intensity angular distribution curve of the blue LED light source.

peak value of the R-645 phosphor is 645 nm. The LED power efficiency at a CCT value of about 4000 K for the different package types was compared with this phosphor particle model. The simulation and experimental results should provide a reference to improve the luminous properties for better packaging and encapsulating designs.

2. Principle

The characteristic parameters of the blue LED, the spectra of the phosphors, and the power transform efficiency of the phosphor powders acting with blue light were established.

2.1. Blue LED Light Source. The dimensions of the blue LED chip were $0.97 \text{ mm} \times 0.51 \text{ mm} \times 0.11 \text{ mm}$. Figure 1(a) shows the radiation power distribution versus wavelength with a peak value of 447 nm; Figure 1(b) shows the angular distribution of the luminous intensity curve.

2.2. Blue LED Source Spectrum, Excitation, and Emission Spectra of the Phosphors. Figure 2 shows the excitation and emission spectra of the R-645, R-626, G-531, and G-529 phosphors and the spectra of the pumping source for the experimental results. The blue LED spectrum is indicated by the blue line with a peak value of 447 nm, the green lines indicate the excitation spectra of the phosphors, and the red lines show the reemission spectra of phosphors with a longer wavelength shift under the blue LED pumping.

2.3. Spectra Analysis of Different Weight Concentrations of Phosphor under the Blue LED Excitation. The radiation power and chromaticity coordinates of four monochromic phosphors, the red phosphors, R-645 and R626, and the green phosphors, G531 and G529, at different weight percentages were measured. Figure 3 shows the schematic structure of the blue LED with a uniformly distributed phosphor film used in this study. The weight concentrations of the four different phosphors are shown in Table 1.

TABLE 1: List of weight concentrations of the four different phosphors.

Type	Weight concentration of phosphors		
R-645	3%	5%	10%
R-626	0.83%	1.37%	2.11%
G-531	5%	10%	20%
G-529	8%	11.2%	15%

A normalized cross-correlation (NCC) formula was adopted to evaluate the fitness between the simulation and empirical data [12]. The NCC is given by

$$\text{NCC} = \frac{(1/N) \sum_{\lambda=380}^{\lambda=780} (A_{\lambda} - \bar{A})(B_{\lambda} - \bar{B})}{\sqrt{(1/N) \sum_{\lambda=380}^{\lambda=780} (A_{\lambda} - \bar{A})^2} \sqrt{(1/N) \sum_{\lambda=380}^{\lambda=780} (B_{\lambda} - \bar{B})^2}}, \quad (1)$$

where A_{λ} and B_{λ} are the values of the radiation power at certain wavelengths, λ ; \bar{A} and \bar{B} are the values of the average radiation power for the simulations and experiments, respectively; and N is the number of experiments and the number of wavelengths to be evaluated.

3. Simulation Results

The empirical and simulated data curves of the radiation power spectra of phosphors of different weight percentages under blue light excitation are discussed in Sections 3.1–3.4.

3.1. Comparison of the Radiation Power Spectra and CIE Chromaticity Locations of Phosphor R-645 with Different Weight Concentrations. Figure 4 shows the radiation power of phosphor R-645 with different weight concentrations (3%, 5%, and 10%) excited by a blue LED. The blue line indicates

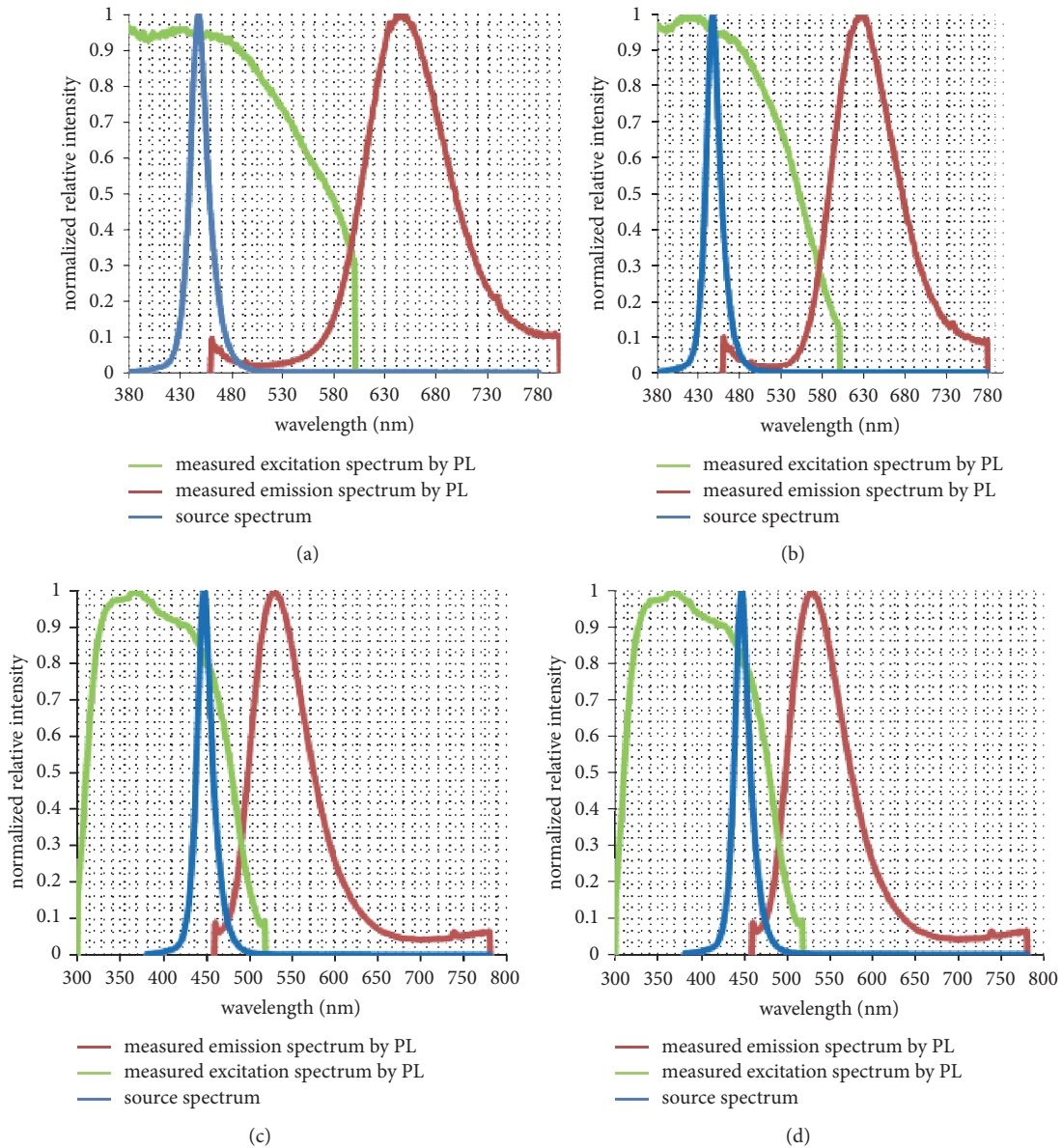


FIGURE 2: Empirical emission spectrum of the blue LED and the excitation and emission spectra corresponding to phosphors (a) R-645, (b) R-626, (c) G-531, and (d) G-529.

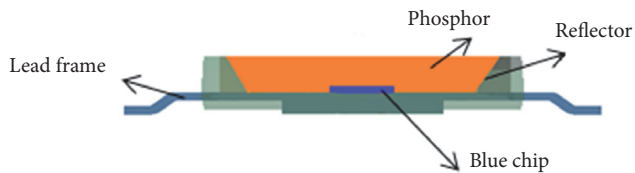


FIGURE 3: Schematic representation of the package with phosphors and a blue LED chip used in the simulation.

the empirical data measured by an integrating sphere and the red lines show the simulation data. A comparison of these curves shows that the higher the weight concentration, the

higher the emission spectra intensity, although the deviations between the simulation and the empirical data were small. The CIE chromaticity coordinates of the five concentrations are listed in Table 2. The location points with values are in terms of the CIE 1931 chromaticity diagram, as shown in Figure 5. It can be seen that a weight concentration of 5% was the best choice for obtaining a magenta-colored light.

3.2. Comparison of the Blue LED Excited Radiation Power Spectrum and CIE Index for Phosphor R-626 of Different Weight Concentrations. Figure 6 shows the radiation power spectra of R-626 phosphors with weight concentrations of 0.83%, 1.37%, and 2.11%, when excited by the blue LED. The intensity of the emission spectra showed a tendency to

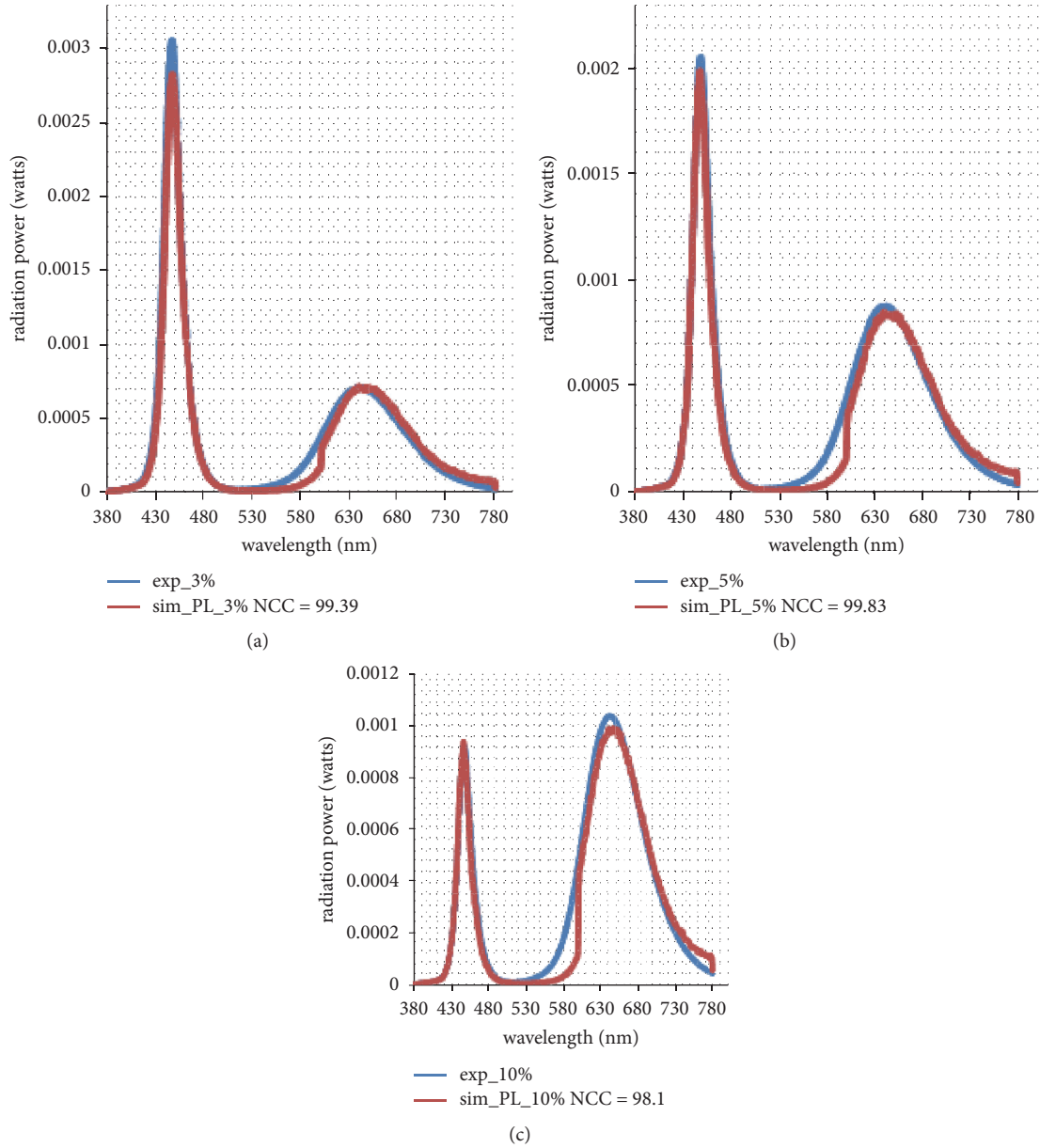


FIGURE 4: Radiation power of phosphor R-645 at three weight concentrations: (a) 3.0 wt%; (b) 5.0 wt%; and (c) 10.0 wt% with blue LED excitation.

TABLE 2: Empirical and simulated chromaticity coordinates of R-645 phosphor with three different weight concentrations with blue LED excitation.

Wt%	Exp- CIE (x, y)	Sim_PL CIE (x, y)
3.0%	(0.2739, 0.1065)	(0.2638, 0.0884)
5.0%	(0.3309, 0.1444)	(0.3138, 0.1151)
10.0%	(0.4412, 0.2114)	(0.4247, 0.1727)

TABLE 3: Empirical and simulated chromaticity coordinates of R-626 phosphor with three different weight concentrations with blue LED excitation.

Wt%	Exp- CIE (x, y)	Sim_PL CIE (x, y)
0.83%	(0.2481, 0.0946)	(0.2416, 0.0847)
1.37%	(0.2912, 0.1267)	(0.2801, 0.1111)
2.11%	(0.3305, 0.1568)	(0.3231, 0.1399)

increase as the concentration increased. The CIE coordinates are listed in Table 3. Figure 7 shows the distributions for the

different concentrations as illustrated in the CIE chromatic diagram. As can be seen in this figure, if magenta light

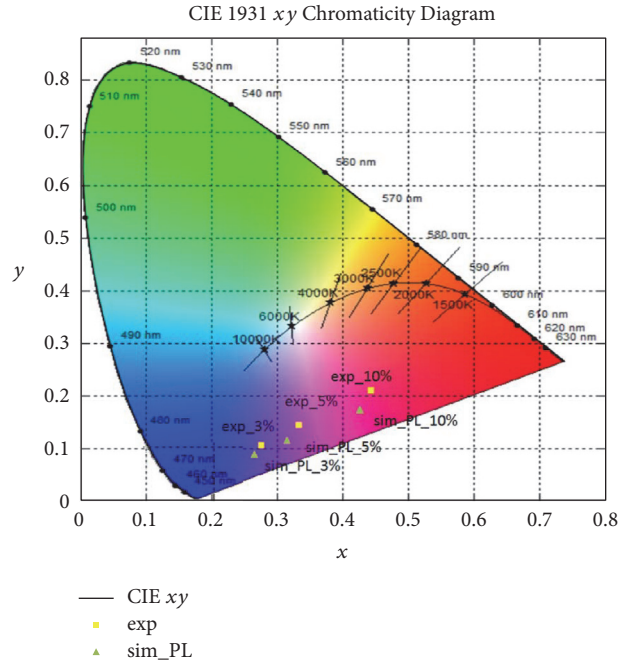


FIGURE 5: Location points on CIE 1931 chromaticity diagram for three different concentrations of phosphor R-645 excited by a blue LED.

TABLE 4: Empirical and simulated chromaticity coordinates of phosphor G-531 with three different weight concentrations under the blue LED excitation.

Wt%	Exp_ CIE (x, y)	Sim_PL CIE (x, y)
5%	(0.1988, 0.2047)	(0.2022, 0.1857)
10%	(0.2158, 0.2783)	(0.2321, 0.2792)
20%	(0.2460, 0.3957)	(0.2745, 0.4017)

TABLE 5: Empirical and simulated chromaticity coordinates of phosphor G-529 with three different weight concentrations under the blue LED excitation.

Wt%	Exp_ CIE (x, y)	Sim_PL CIE (x, y)
8%	(0.2669, 0.3361)	(0.2804, 0.3124)
11.2%	(0.2862, 0.3876)	(0.3101, 0.3740)
15%	(0.3013, 0.4268)	(0.3413, 0.4354)

is required, then the 2.11 wt% would be a good choice for this design. Also, as discussed in Section 3.1, if light with a magenta color (R-645 phosphor at 5 wt%) was required, only the 2.11 wt% of R-626, for a 2.89 wt% reduction, would be used.

3.3. Comparison of the Radiation Power Spectrum and CIE Index of G-531 Phosphor with Different Weight Concentrations under the Blue LED Excitation. Figure 8 shows the radiation power spectra of the G-531 phosphors with weight concentrations of 5%, 10%, and 20% under the blue LED excitation. The intensity of the emission spectra increased with the increases in the concentration. The CIE coordinates are shown in Table 4, and the distributions for the different concentrations in the CIE chromatic diagram are shown in Figure 9. As can be seen in the figure, if a design with cyanic light were demanded, then the concentration of the G-531 phosphor should be near 15%.

3.4. Comparison of the Radiation Power Spectrum and CIE Index of G-529 Phosphors with Different Weight Concentrations under the Blue LED Excitation. Figure 10 shows the radiation power spectra of G-529 phosphors under the blue LED excitation with weight concentrations of 8%, 11.2%, and 15%. The intensity of the emission spectra also increased as the concentration increased. The CIE chromaticity coordinates are listed in Table 5, and the distributions of the different concentrations in the CIE chromatic diagram are shown in Figure 11. When cyanic light is required, the concentration of G-529 phosphor should be about 8%. Compared with the results discussed in Section 3.3, where the concentration was 15%, this design reduced the weight concentration by 7% and produced mixed light located at the cyan region.

3.5. Weight Concentrations of Phosphor and Luminal Efficiency Analysis for Four Types of Packages at a Color Temperature of 4000 K. Figure 12 depicts the absorption and emission spectra of Y-561 phosphors and the source spectrum of the

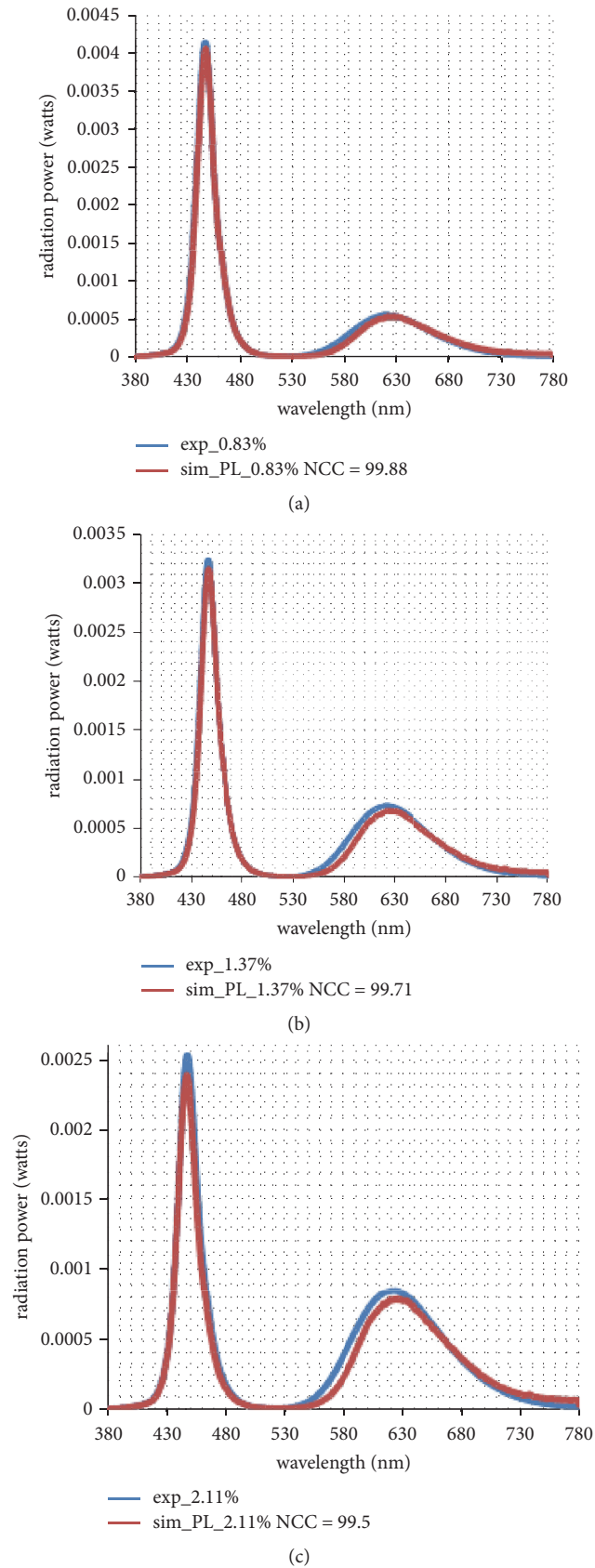


FIGURE 6: Radiation power of R-626 phosphor at three weight concentrations: (a) 0.83 wt%; (b) 1.37 wt%; and (c) 2.11 wt% with the blue LED excitation.

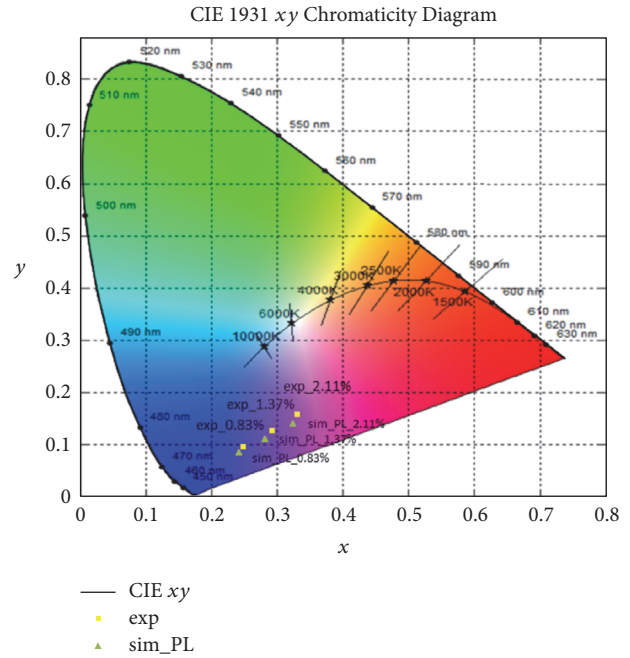


FIGURE 7: CIE chromaticity diagram from empirical and simulation data for R-626 phosphor (with three different weight concentrations) under blue LED excitation.

blue LED. Since white light can be obtained by mixing blue and yellow light, we combined a blue LED, with a spectrum peak value of 447 nm, and adjusted the weight percentage of the Y-561 phosphor under excitation to obtain white light of the desired color temperature.

If we want the color temperature of the mixed light to be 4000 K, we must calculate the weight concentration of Y-561 phosphor from the coordinates of the cross point of the black locus at 4000 K and a line connecting the location points of the blue LED and phosphor emission spectra on the CIE chromaticity diagram, as shown in Figure 13.

Figure 14 shows the four types of packages adapted in our simulation models. The weight percentages of the Y561 phosphor in these packages were manipulated to ensure that the chromaticity points were at the locus of blackbody radiation of 4000 K for simulation purposes; the percentages corresponding to the four types of packages, dispensing, conformal, remote, and semispherical, were 7.6%, 64.0%, 24.1%, and 24%, respectively. The weights of the epoxy encapsulants were 15.13 mg (dispensing), 0.24 mg (conformal), 6.20 mg (remote), and 0.77 mg (semispherical). Based on this data, the amount of phosphors used by the four types of packages could be calculated. The weights were 1.24 mg for the dispensing type, 0.42 mg for the conformal type, 1.97 mg for the remote type, and 0.24 mg for the semispherical type, as shown in Figure 15.

It was found that the Y-561 phosphor was excited by a blue LED with a power spectrum having a peak wavelength of 447 nm and that the semispherical type of package had a lower weight percentage than the other types for a color temperature of around 4000 K.

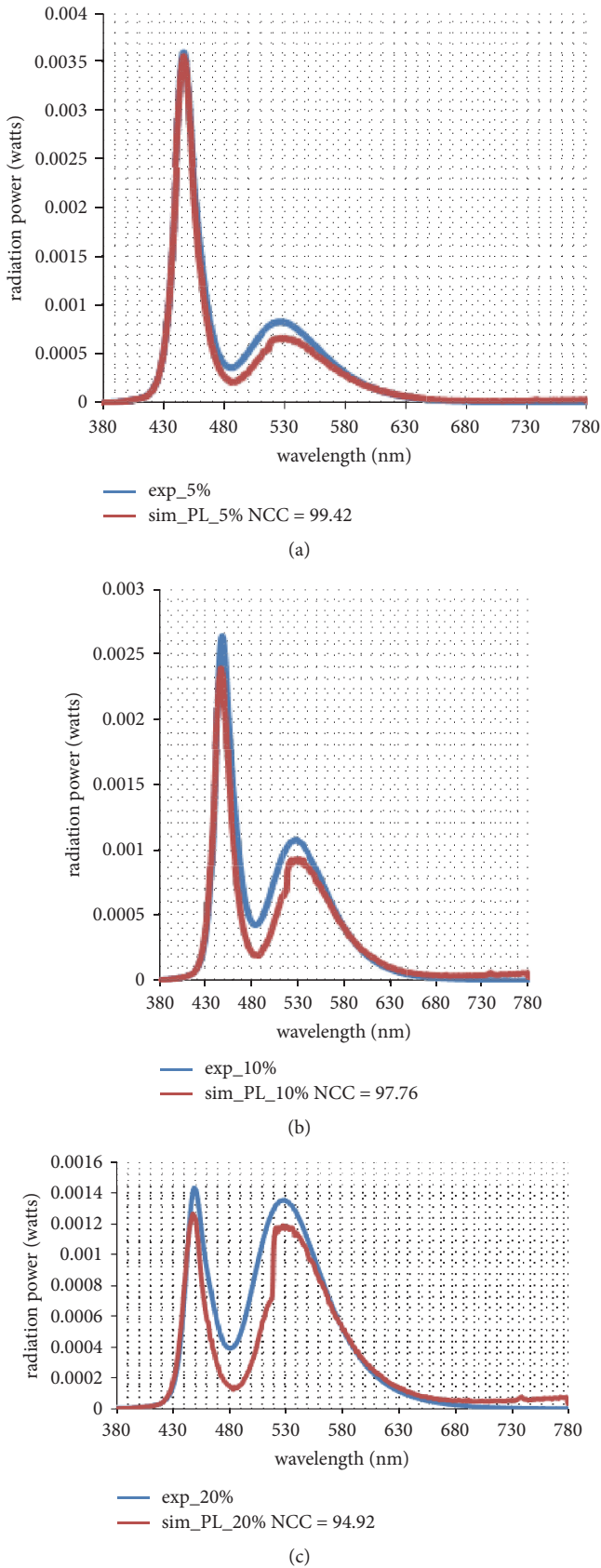


FIGURE 8: Radiation power of phosphor G-531 with three weight concentrations: (a) 5 wt%; (b) 10 wt%; and (c) 20 wt% with the blue LED excitation.

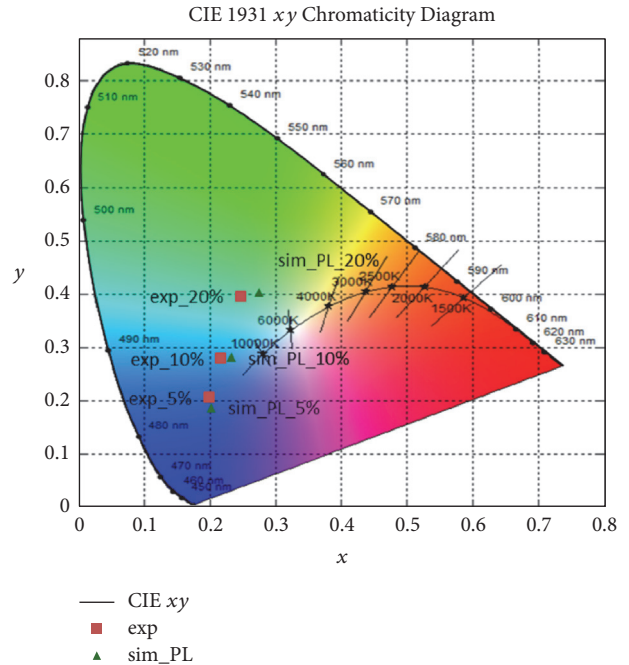


FIGURE 9: Chromaticity diagram of empirical and simulated data for G-531 phosphor with three different weight concentrations excited by a blue LED.

4. Conclusions

In this study, all the phosphors were excited under a blue LED with a peak power spectrum value of 447 nm. The power of the emission spectra of the red phosphors (R-645, R-626) and green phosphors (G-531, G-529) increased with an increase in the phosphor concentration. However, the deviations between the simulation and empirical curves tended to increase as the weight percentages increased, and further studies are needed to improve the results. When a 5% weight concentration of R-645 phosphor or a 2.11% weight concentration of R-626 phosphor was combined with the blue LED, chromaticity coordinates near the magenta area were obtained. When an 8% weight concentration of G-529 phosphor was combined with a blue LED, the mixed light was within the cyan spectrum.

To produce a mixed white light with a color temperature of around 4000 K with phosphor Y-561 and the blue LED, the concentration of phosphors was calculated from the intersection coordinates of the two lines on the CIE chromaticity diagram: the first being the locus of blackbody radiation at 4000 K; the other line being the connection points between the blue LED spectrum and the Y-561 phosphor emission spectrum. The chromaticity coordinates of this point were $x = 0.3804$ and $y = 0.3768$. The simulations for the least amount of Y-561 phosphor to achieve a color temperature of 4000 K.

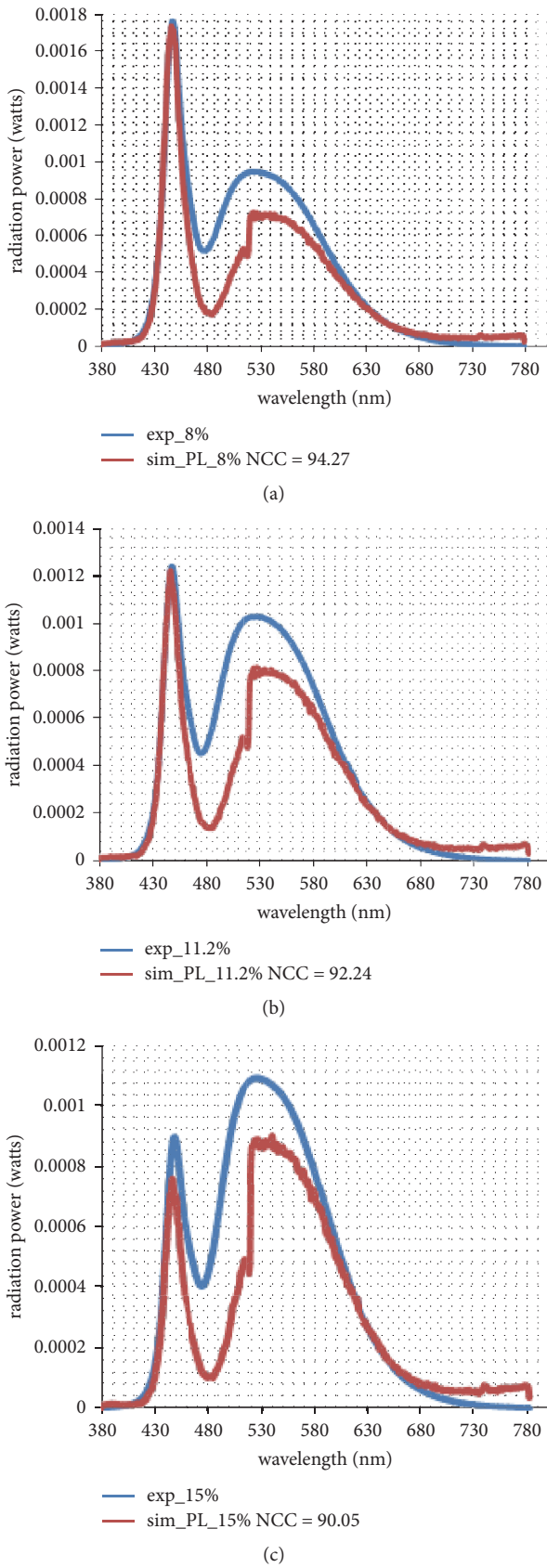


FIGURE 10: Radiation power of G-529 phosphor with three weight concentrations: (a) 8 wt%; (b) 11.2 wt%; and (c) 15 wt% excited by the blue LED.

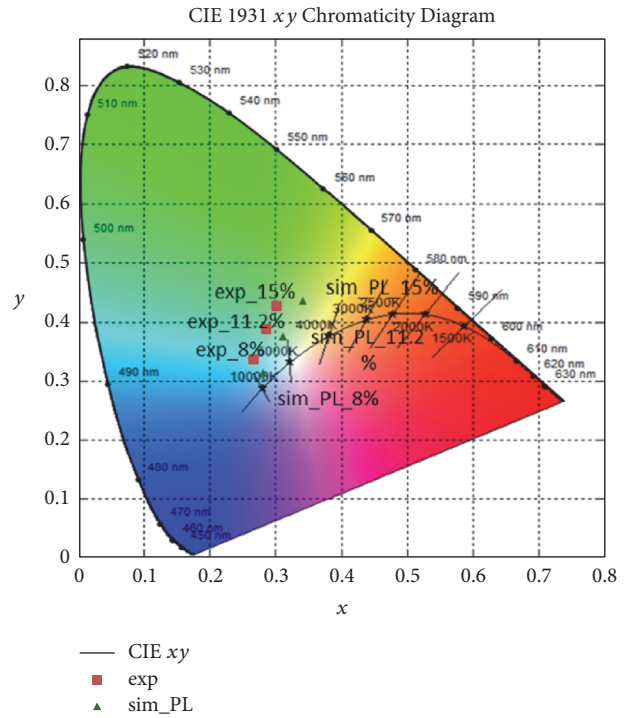


FIGURE 11: Chromaticity diagram of G-529 phosphors with three different weight concentrations excited by a blue LED.

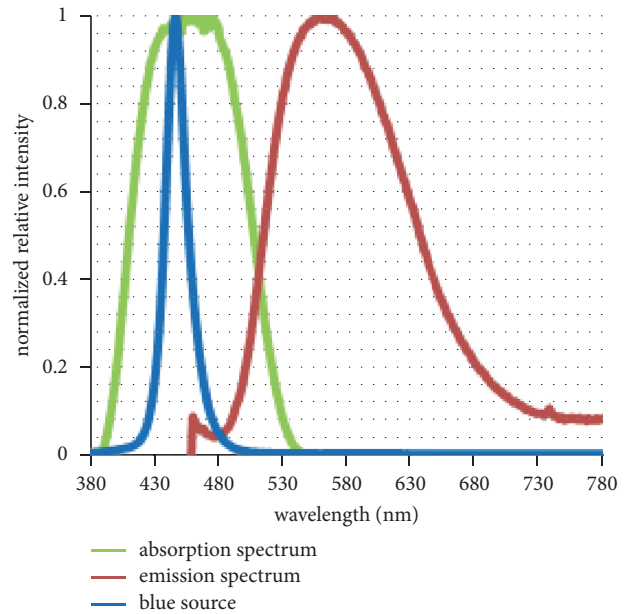


FIGURE 12: Power spectrum of the blue LED and the emission and absorption spectra of Y-561 phosphor.

Conflicts of Interest

The authors declare that there are no conflicts of interest regarding the publication of this paper.

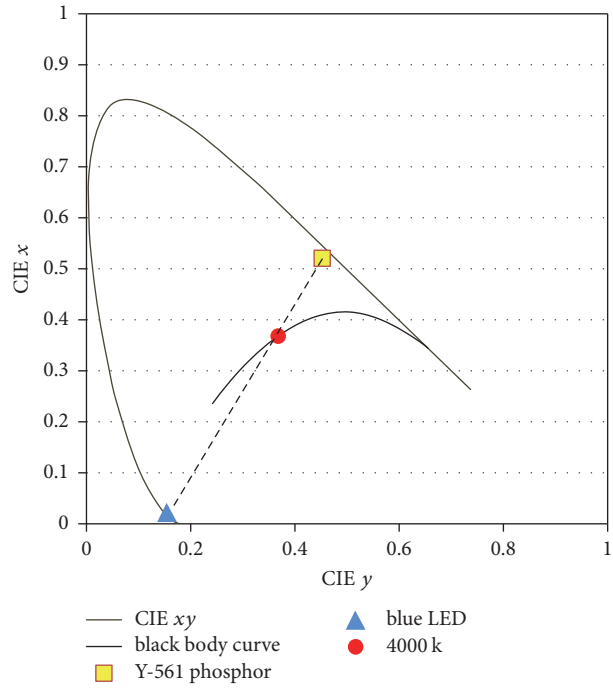


FIGURE 13: Schematic for location determination of white light from the points in the CIE chromaticity diagram of the blue LED and yellow Y-561 phosphor.

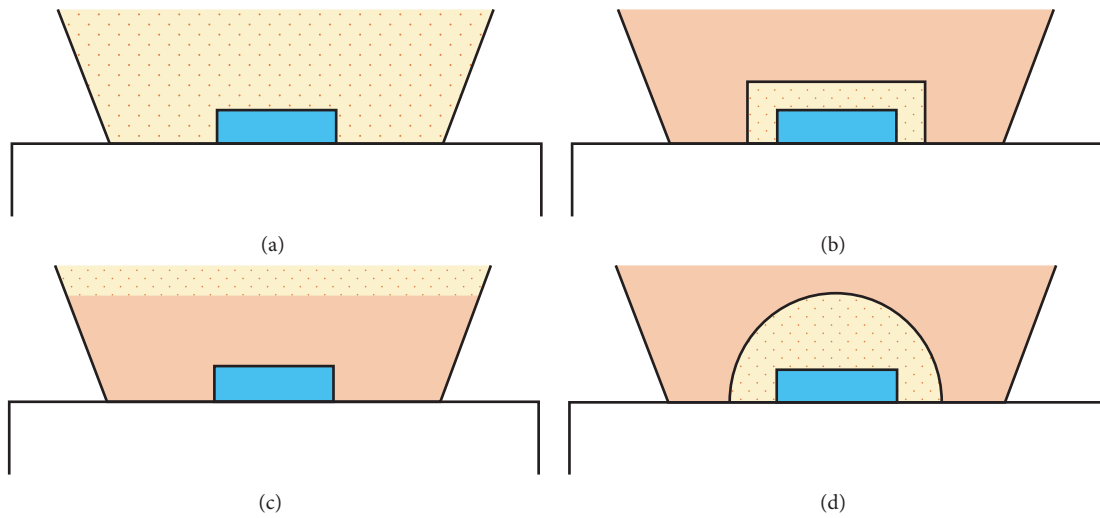


FIGURE 14: Four types of packages for simulation: (a) dispensing; (b) conformal; (c) remote; (d) semispherical.

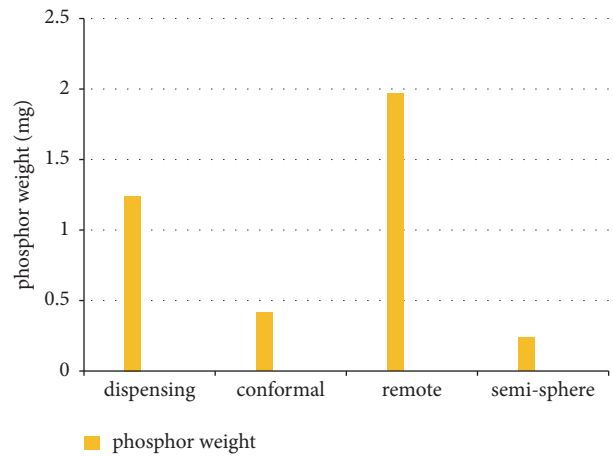


FIGURE 15: Comparison of light efficiency with phosphor weight for the four package types.

Acknowledgments

This study was sponsored by the Ministry of Science and Technology, Taiwan, under Contracts nos. MOST106-2221-E-008-075 and MOST 106-2221-E-035-072-MY2.

References

- [1] S. Pimputkar, J. S. Speck, S. P. Denbaars, and S. Nakamura, "Prospects for LED lighting," *Nature Photonics*, vol. 3, no. 4, pp. 180–182, 2009.
- [2] Y. Shimizu, K. Sakano, Y. Noguchi, and T. Moriguchi, U.S. patent 5998925, 1999.
- [3] A. A. Setlur, A. M. Srivastava, H. A. Comanzo, and D. D. Doxsee, U.S. patent 6685852, 2004.
- [4] Y. H. Won, H. S. Jang, K. W. Cho, Y. S. Song, D. Y. Jeon, and H. K. Kwon, "Effect of phosphor geometry on the luminous efficiency of high-power white light-emitting diodes with excellent color rendering property," *Optics Letters*, vol. 34, no. 1, pp. 1–3, 2009.
- [5] C.-Y. Chen, T.-H. Yang, C.-H. Hsu, and C.-C. Sun, "High-efficiency white LED packaging with reduced phosphor concentration," *IEEE Photonics Technology Letters*, vol. 25, no. 7, pp. 694–696, 2013.
- [6] T.-H. Yang, C.-Y. Chen, Y.-Y. Chang et al., "Precise Simulation of Spectrum for Green Emitting Phosphors Pumped by a Blue LED Die," *IEEE Photonics Journal*, vol. 6, no. 4, 2014.
- [7] M.-T. Wang and J.-M. Huang, "Accurate control of chromaticity and spectra by feedback phosphor-coating," *Optics Express*, vol. 23, no. 9, pp. 11576–11585, 2015.
- [8] S. A. Schafer, "Quasi-Monte Carlo methods: applications to modeling of light transport in tissue," in *Proceedings of the Laser-Tissue Interaction VII*, vol. 2681, pp. 317–324, SPIE Proceedings, 1996.
- [9] S. J. Lee, "Analysis of light-emitting diodes by Monte Carlo photon simulation," *Applied Optics*, vol. 40, no. 9, pp. 1427–1437, 2001.
- [10] G. Mie, "Beiträge zur Optik trüber Medien, speziell kolloidaler Metallösungen," *Annalen der Physik*, vol. 330, no. 3, pp. 377–445, 1908.
- [11] C.-C. Sun, T.-X. Lee, S.-H. Ma, Y.-L. Lee, and S.-M. Huang, "Precise optical modeling for LED lighting verified by cross correlation in the midfield region," *Optics Express*, vol. 31, no. 14, pp. 2193–2195, 2006.
- [12] J. Fox, *Applied Regression Analysis, Linear Models, and Related Methods*, SAGE Publications, Incorporated, 1997.

Research Article

Angle-Scanning Surface Plasmon Resonance System with 3D Printed Components for Biorecognition Investigation

ChenGuang Zhang,¹ Ching-Jung Chen ,^{1,2} Kalpana Settu,³ and Jen-Tsai Liu ⁴

¹School of Electronic, Electrical and Communication Engineering, University of Chinese Academy of Sciences, China

²School of Opto-Electronic Technology, University of Chinese Academy of Sciences, China

³Department of Electrical Engineering, National Taipei University, Sanxia, Taiwan

⁴College of Materials Science and Opto-Electronic Technology, University of Chinese Academy of Sciences, China

Correspondence should be addressed to Ching-Jung Chen; cjchen@ucas.ac.cn and Jen-Tsai Liu; jtliu@ucas.ac.cn

Received 7 April 2018; Revised 17 May 2018; Accepted 24 May 2018; Published 11 July 2018

Academic Editor: Shuan-Yu Huang

Copyright © 2018 ChenGuang Zhang et al. This is an open access article distributed under the Creative Commons Attribution License, which permits unrestricted use, distribution, and reproduction in any medium, provided the original work is properly cited.

Surface plasmon resonance (SPR) is a real-time, label-free, and high-sensitive detection technology. SPR has been widely used in many applications such as biomolecular interaction analysis, environmental monitoring, and medical diagnostics. However, conventional SPR sensor systems usually require expensive equipment and complicated optics. In this paper, we have demonstrated a rapid prototyping of angle-scanning SPR for bioanalytical investigation. Rapid prototyping was attained by utilizing the FDM (fused deposition modeling) based 3D (three-dimensional) printing technology. Two rotating platforms were employed to drive the laser source and photodiode, respectively. A temperature regulation unit was incorporated to maintain the system temperature in order to reduce the temperature effect. The proposed SPR rapid prototyping yielded a refractive index resolution of 6.4×10^{-6} RIU (refractive index unit), and the biotin-avidin system validated the kinetics parameters measurement capability. The obtained results indicated that the FDM 3D printing has great potential for developing rapid-prototyping SPR system.

1. Introduction

Surface plasmon resonance (SPR) is a surface-sensitive optical technique that is used to study a thin layer on a metal surface. When P-polarized light is projected onto metal film, it can excite the oscillation of the electrons on the surface of the film. This oscillation is called surface plasmon wave (SPW). When the wave vector of the incident light matches the wave vector of SPW, the reflected light intensity decays rapidly, and the corresponding angle of the incident light is called resonance angle. Surface plasmon resonance (SPR) is a powerful analytical technology. It can detect the thickness of the films absorbed onto the sensor surface and interactions between biomolecules such as antigen-antibody or protein-DNA [1–5]. In comparison with traditional detection methods, like X-ray, HPLC, and HPLC-MS, SPR technology can perform kinetics parameters (association and dissociation process) measurement, concentration measurement, and real-time

molecule detection. It has been widely used in chemical, biology, agriculture, environment, and food safety [6–12].

Traditional SPR systems usually require expensive equipment and complicated optics. The cost of commercial SPRs varies from \$10,000 to \$5,000,000, and the refractive index resolution ranges from 10^{-5} RIU (refractive index unit) to 10^{-7} RIU. Many optical-fiber based SPRs have been studied intensively in the literature [13–15]. The structure of these devices is relatively simple. However, the resolution and dynamic range are often sacrificed [16, 17]. To reach a high resolution of 10^{-6} RIU or 10^{-7} RIU, a spectrometer is always required for an optical-fiber SPR [18].

Compared with optical-fiber SPR, angle-scanning SPR has the capability of achieving high resolution and wide refractive index measurement range. A specific wavelength laser is irradiated on a metal film surface and scanned to achieve certain range of incident angle. However, angle-scanning SPR requires more mechanical components, and

also the optical path is more complicated. Typical angle-scanning SPRs are based on Kretschmann configuration. It involves many mechanical components manufacturing and complex optical path design. Therefore, constructing a compact home-made SPR is of great importance.

3D printing, also called additive manufacturing, since its origins in 1980s has been a tool for developing rapid-prototyping products. With the expiration of 3D printing technology patents, this field has witnessed a great growth [19]. FDM (fused deposition modeling) is one of the most popular 3D printing technologies. In FDM 3D printing, a heated nozzle is employed to melt raw material and extrude fused material onto a building platform, and it lays the fused material in layers. A wide range of materials can be printed, such as acrylonitrile butadiene styrene (ABS), polylactic acid (PLA), high-impact polystyrene (HIPS), and thermoplastic polyurethane (TPU). After the emergence of open source RepRap project, desktop fused deposition modeling (FDM) 3D printers have become more popular among users, manufacturers, and researchers. It is simple, cost effective, and versatile. Application of FDM 3D printing technology to toys, prototypes, scientific tools, and medical equipment becomes more and more common [19–23].

Using 3D printing technology to design an SPR is an interesting and attractive thing. Recently, some studies have demonstrated the use of 3D printing in SPR platform. Hasan et al. developed a smartphone based SPR imaging platform for on-site biodetection [16]. They utilized the 3D printing technique just to print the device holder. This system has a dynamic range less than 0.02 RIU, which limits the application for measuring large refractive index change. Bonyár et al. proposed an acrylic photopolymer material-based 3D printing to fabricate molds for PDMS (polydimethylsiloxane) casting and flow cell for SPR instrument. This method enabled the customization of SPR flow cell alone [24]. However, 3D printing technology could be further applied to SPR. The use of 3D printing technology simplifies the process of manufacturing, accelerates the design of prototype, and makes designs more flexible. Furthermore, complex equipment, such as lathes and milling machines, is not important any more, even nonexpert users can quickly copy and build a 3D printed project.

In this study, we have demonstrated a rapid-prototyping angle-scanning SPR utilizing FDM 3D printing technology. PLA filament was chosen for its relative high tensile strength (~50 MPa), good reproducibility, and low cost. With the help of 3D printing, the flow cell and optical path were designed to be modular and customizable. Refractive index resolution was found to be 6.4×10^{-6} RIU. To validate the bioanalytical capability, biotin-avidin system was used as target analyte.

2. Method

Biotin and Avidin were purchased from Macklin Biochemical Co. Ltd. (Shanghai, China). N-hydroxysulfosuccinimide sodium salt (sulfo-NHS) and 1-(3-dimethylaminopropyl)-3-ethylcarbodiimide hydrochloride (EDC) were purchased from Aladdin Chemistry Co. Ltd. (Shanghai, China). Cysteamine and Sodium dodecyl sulfate (SDS) were obtained

from Beijing Biotopped Science & Technology Co. Ltd. (Beijing, China). Absolute ethyl alcohol and NaCl were purchased from Beijing Chemical Works (Beijing, China). Deionized water obtained from a CCT-3300 water purification system was used in all the experiments. Matching oil series E (1.520) was purchased from Cargill Dow LLC. (USA). Polylactide (PLA) 3D printing filaments (1.75mm) were purchased from 3D Systems (USA).

The developed SPR system includes a 650nm laser source (Shenzhen Fuzhe Technology Co. Ltd. 150mW, Shenzhen, China), a photodiode (2DU 10 mm × 10 mm), a polarizer (F-PZP-001 ϕ 15 mm × 2mm), and a BK7 triangle prism (20mm × 20mm × 10mm). Au-coated glass slides (2mm × 8mm × 30mm) were prepared by coating 47.5 nm thickness of Au layer using sputtering deposition method. Prior to the deposition the Au film, the glass slide was precoated with 2 nm chromium layer to enhance the adhesion of the Au film. Cube 3 3D printer (3D Systems, USA) was used to print the necessary SPR system components (Fig S1). Silhouette Portrait (Silhouette America, Inc.) was used to cut the flow cell. Two rotating platforms (Beijing PDV Instrument Co., Ltd., China) were employed as the mechanical drivers. Open source boards (Arduino Mega 2560) accompanied with a self-made amplifier circuit comprise the hardware circuits. Two TECs (Thermoelectric Coolers) TESI-12704 (Hebei I.T. Co. Ltd., 3.3mm × 30mm × 30mm, Shanghai, China) were adapted as the temperature controller.

Schematic of rapid-prototyping angle-scanning SPR system block diagram is shown in Figure 1. Light from the laser source was first p-polarized by a polarizer and then projected onto the sensor surface via a triangle prism. The reflected light from the sensor surface was collected by a photodiode. The collected raw signal was amplified by a self-made amplifier circuit and sampled the built-in ADC (analog to digital converter) of the microcontroller unit ATmega2560 (Microchip Technology Inc., 8-bit AVR microcontroller, Chandler, Arizona, USA). Digital signals were eventually transmitted to the software on computer for analysis. The platform controller can drive the system to scan from 40° to 72°. When performing measurements, instead of scanning a whole SPR spectrum, an angle range of 3° around the resonance angle was scanned at a speed of 0.3°/s. For the temperature regulation unit, low temperature drift coefficient NTC (Negative Temperature Coefficient) resistors (SEMITEC Corporation, 103AT-4 Shape1, Japan) were employed to sense the system temperature and signals from NTC resistors were quantified by a 16-bit high-precision ADC ADS1115 (Texas Instruments Inc. USA). A microcontroller ATmega328 (Microchip Technology Inc., 8-bit AVR microcontroller, Chandler, Arizona, USA) was used to obtain the temperature information from ADS1115 via IIC (Inter-Integrated Circuit) communication protocol and control the heating or cooling of the flow cell through TECs. A PID (proportional-integral-derivative) controller algorithm was incorporated with ATmega328 to maintain a stable temperature circumstance.

The flow cell module consists of rubber flow cell and stainless part. Arrangement of the flow cell module is shown in Fig. S2. The rubber flow cell of volume 65 μ L and dimension 5.3 mm × 23 mm × 0.5 mm was designed and constructed

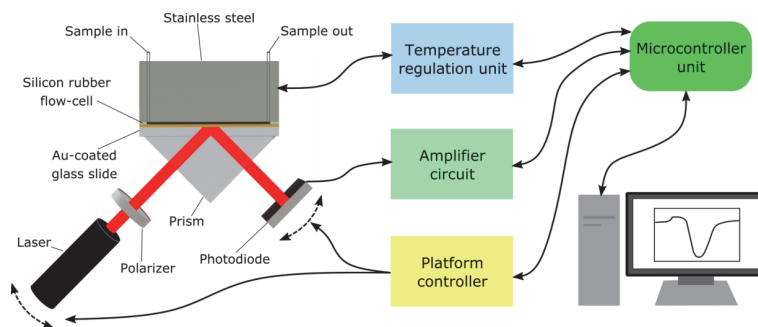


FIGURE 1: Schematic representation of the complete SPR system.

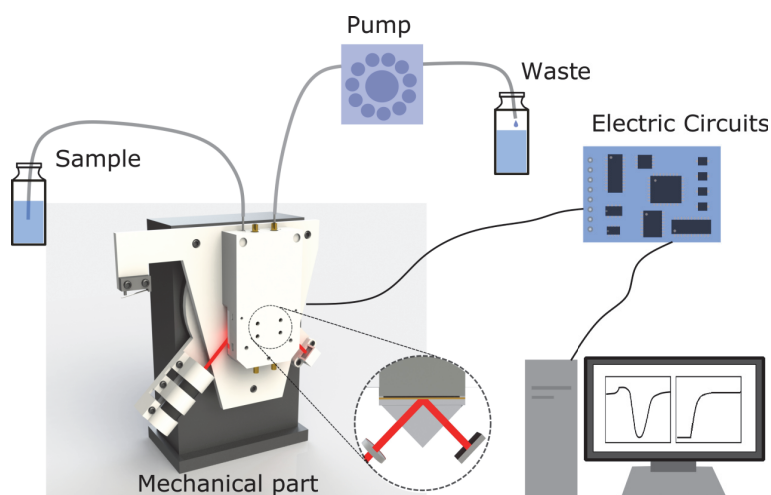


FIGURE 2: Overview of the designed SPR system by rapid-prototyping 3D printing.

using desktop cutter Silhouette Portrait. However, one can customize the shape of flow cell by modifying the digital design file and snip it in the rubber film with Silhouette Portrait.

Overview of the developed rapid-prototyping SPR system was depicted in Figure 2. The system was constructed with 3D printed components. Cube 3 desktop version 3D printer was used to print the components with PLA filaments. The component models were designed using SolidWorks 2012 software and saved as STL (Standard Triangle Language) file format. Then, these STL files were imported into the 3D printer's software Cubify version 3.9.0 (3D systems, USA). Two rotating platforms were employed and a 3D printed optical platform was installed onto the rotating platforms. The laser source and photodiode can be easily mounted onto the optical platform with the 3D printed holders. Unlike the laser and photodiode, the flow cell module was removable and customizable. Furthermore, the alignment of optical parts can be achieved effortlessly.

The SPR sensor functionalization process is shown in Figure 3. To functionalize the SPR sensor with biotin, Au-coated glass slide was first cleaned ultrasonically with 4% sodium dodecyl sulfate (SDS) solution and rinsed with deionized water. Then it was exposed to UV light for 20 minutes. Au-coated glass slide was then immersed in 10 mM

cysteamine solution for 2 hours and subsequently rinsed with deionized water to remove the residual cysteamine. The resulting sensor was then immersed in 0.2 mg/mL biotin solution containing 15 mM EDC and 5 mM sulfo-NHS. Then the sensor was rinsed in deionized water and absolute ethanol and dried under a stream of nitrogen for further use.

3. Experimental

We used Tianmin contact angle meter to measure water contact angle at each modification stage. SPR sensor chips were mounted on the plane of contact angle meter. 4 μL of deionized water was dropped onto the sensor chip surface. The droplet cross-section was recorded as image file by the camera on the contact angle meter. Open source software ImageJ was used to estimate the contact angle from recorded image files.

The most benefit of SPR biosensor technology is the determination of kinetics of biomolecular interactions. It can be determined that the interaction of analytic A and ligand B is immobilized on sensor surface. It usually uses the simplest case $A + B \rightarrow AB$. In this study, The kinetic parameters measurement capability of the developed system was validated using the biotin-avidin system. Affinity interactions between biotin and avidin were characterized by the association rate constant k_a , dissociation rate constant k_d , and equilibrium

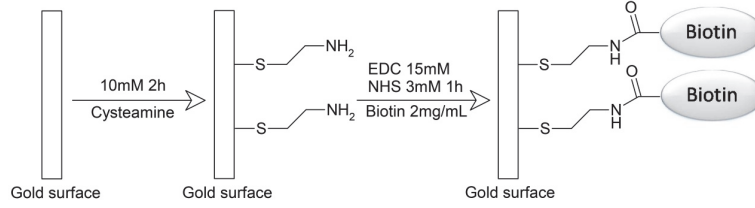


FIGURE 3: SPR sensor modification process.

association constant K_{eq} , where A is the injected analyte, B is the immobilized ligand, and AB is the analyte-ligand complex. The experiment data was fitted with $A + B \rightarrow AB$ interaction model. The interaction process can be described as (1). The response signal R of SPR system is proportional to the amount of [AB], k_{app} is the apparent reaction rate constant, t is the interaction time, and the maximum response signal R_{max} is proportional to the initial [B]. A series of concentrations of [A] solutions were used to derive the relationship between k_{app} and different concentrations of [A], and a regression curve was obtained from (2). Thus k_a is the slope of the regression, k_d is the intercept of the regression curve, and K_{eq} is computed as k_a / k_d .

$$R = \frac{k_a [A] R_{max}}{([A] k_a + k_d)} [1 - e^{-k_{app} t}] \quad k_{app} = [A] k_a + k_d \quad (1)$$

$$\begin{aligned} k_{app1} &= [A_1] k_a + k_d \\ k_{app2} &= [A_2] k_a + k_d \\ &\dots \\ k_{appn} &= [A_n] k_a + k_d \end{aligned} \quad (2)$$

For fast kinetics parameters measurement, affinity interactions between biotin and avidin were characterized by the association rate constant k_a , the dissociation rate constant k_d , and the equilibrium association constant K_{eq} . However, the interaction process is divided into association phase, equilibrium phase, and dissociation phase. The dissociation rate constant k_d was obtained from the dissociation phase by (3). Then it was substituted into (1) to obtain k_a from the association phase. Thus K_{eq} was computed as the ratio of association and dissociation rate constants.

$$\frac{dR}{dt} = -k_d R \quad (3)$$

4. Results and Discussion

Prior to conducting the biomedical experiment, effectiveness of the sensor surface modification should be verified. Contact angle measurement is a powerful tool to examine every step during the sensor functionalization. Results of contact angle measurement are shown in Figure 4. Bare Au surface exhibited a value of 88.378°. After 20 min of UV exposure, the contact angle decreased to 71.922°. This contact decrease indicates that the UV exposure could effectively

remove the impurities on the Au film. When the cysteamine self-assembled monolayers (SAMs) formed on Au film, the contact angle became 46.720°, which indicated that the cysteamine SAM is terminated with a hydrophilic domain $-NH_2$ [25]. Subsequently, after the immobilization of biotin onto the cysteamine SAM, the contact angle decreased to 21.911° from 46.720° of the cysteamine SAM. The reason was that the ureido- and tetrahydrothiophene-rings of biotin are more hydrophilic than $-NH_2$ terminated cysteamine SAM [26]. The contact angle of biotin SAM was smaller than the previously reported one in study [27], and this may be due to the well-organized biotin SAM. Thus, the above results showed that the SPR sensor chip was prepared successfully.

The interactions between biotin and different concentrations of avidin solution are plotted in Figure 5. A higher concentration of avidin showed a faster association rate. Biotin SAM on the sensor surface was saturated in a short time. Meanwhile, at lower concentration of avidin, the association process occurred slowly, and it took a longer time to reach equilibrium. After the saturation of biotin on the sensor surface, the binding of biotin and avidin reaches equilibrium, and the SPR response signal reaches R_{max} . The relationship between k_{app} and various concentrations of avidin was plotted as shown in Figure 6. The linear regression equation was obtained as $k_{app} = 4.9 \times 10^4 \times [C] + 5.4 \times 10^{-5}$, where C is the avidin concentration. Thus the kinetic parameter k_d was first obtained as $5.4 \times 10^{-5} \text{ s}^{-1}$, k_a was obtained as $4.9 \times 10^4 \text{ M}^{-1} \text{ s}^{-1}$, and the K_{eq} was computed as $9.8 \times 10^8 \text{ M}^{-1}$, which is close to the K_{eq} reported by Zhao et al. [28].

For fast kinetic parameters measurement, 73.2 nM avidin was used. The interaction process during the association phase, equilibrium phase, and dissociation phase was recorded as in Figure 7. For the dissociation phase, k_d was derived as 0.0012 s^{-1} . After substituting k_d into (1), we obtain $k_a = 3.551 \times 10^4 \text{ M}^{-1} \text{ s}^{-1}$ and $K_{eq} = k_a / k_d = 2.96 \times 10^7 \text{ M}^{-1}$. The kinetics parameters obtained using the two above methods were different. However, the fast kinetics parameters measurement utilizes the association and dissociation phase of the interaction process at only one concentration. Comparing these two methods, the results showed that the system has the capability to analyse the interaction between protein and ligands by different analytic concentrations.

5. Conclusions

This work presented the development of a rapid-prototyping surface plasmon resonance utilizing FDM 3D printing

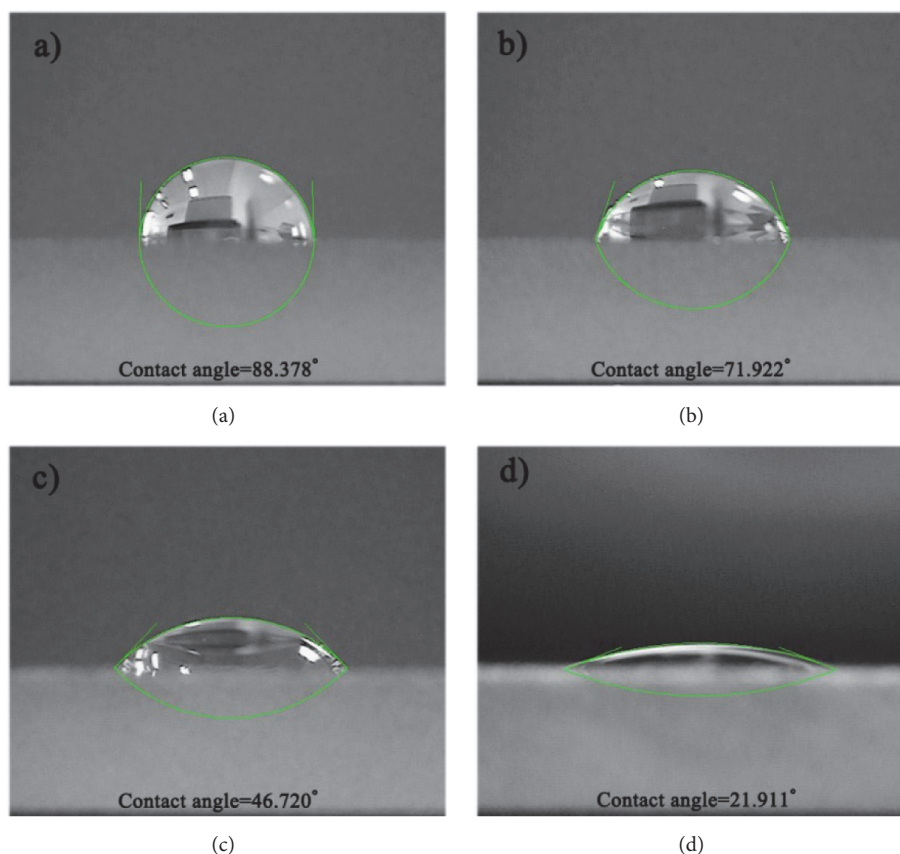


FIGURE 4: Contact angle measurement: (a) bare Au film; (b) Au film after 20 min UV exposure; (c) Au/cysteamine SAM; (d) Au/cysteamine/ biotin film.

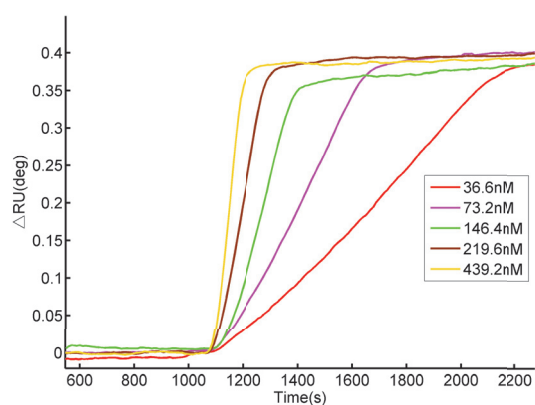


FIGURE 5: Association curve of biotin and avidin.

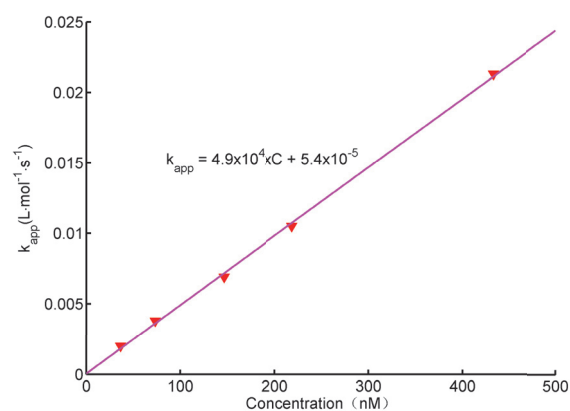


FIGURE 6: k_{app} versus different concentrations of avidin.

technology. The developed device was modular and the optical path and flow cell were customizable. The system performance was validated with a series of experiments, and our system showed a high resolution of 6.4×10^{-6} RIU. Furthermore, kinetics parameters measurement capability was validated by biotin-avidin system. In the future, we will aim to develop our 3D-SPR to be more modular and easier

to construct, so that many institutes or researchers can build their own 3D-SPR.

Data Availability

The data used to support the findings of this study are included within the article.

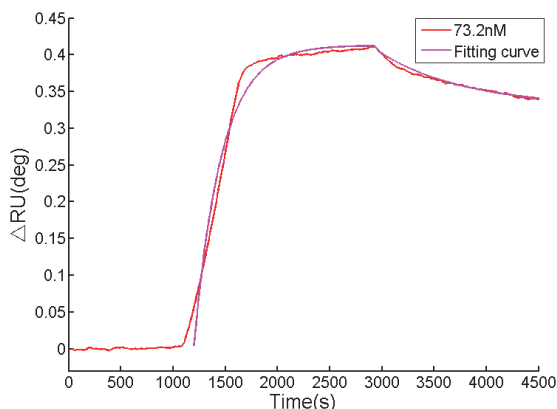


FIGURE 7: Interaction curve for 73.2nM avidin.

Conflicts of Interest

The authors declare that they have no conflicts of interest.

Acknowledgments

This work was supported by Beijing Natural Science Foundation (Z160002), the State Key Project of Fundamental Research (Grant 2014CB931900), UCAS Young Teacher Research Fund (Grants Y55103NY00, Y55103EY00, Y65201FY00, and Y25102TN00), and the Chinese Academy of Sciences Key Project Foundation (KFZD-SW-202).

Supplementary Materials

Figure S1 is mainly used to replace metal manufactured parts, including the optical base, holders, and fitting parts. 3D printing enables the rapid assembly of scattered devices such as laser, photodiode, prism, and Au-coated glass slide into a complete system. Figure S2 is the flow cell module which consists of rubber flow cell and stainless part. (*Supplementary Materials*)

References

- [1] I. Stojanović, R. B. M. Schasfoort, and L. W. M. M. Terstappen, "Analysis of cell surface antigens by Surface plasmon resonance imaging," *Biosensors & Bioelectronics*, vol. 52, pp. 36–43, 2014.
- [2] K. M. Byun, N.-H. Kim, Y. H. Ko, and J. S. Yu, "Enhanced surface plasmon resonance detection of DNA hybridization based on ZnO nanorod arrays," *Sensors and Actuators B: Chemical*, vol. 155, no. 1, pp. 375–379, 2011.
- [3] J. R. Wayment and J. M. Harris, "Biotin-avidin binding kinetics measured by single-molecule imaging," *Analytical Chemistry*, vol. 81, no. 1, pp. 336–342, 2009.
- [4] T. Hiragun, Y. Yanase, K. Kose et al., "Surface plasmon resonance-biosensor detects the diversity of responses against epidermal growth factor in various carcinoma cell lines," *Biosensors and Bioelectronics*, vol. 32, no. 1, pp. 202–207, 2012.
- [5] A. Kausaite, M. Van Dijk, J. Castrop et al., "Surface plasmon resonance label-free monitoring of antibody antigen interactions in real time," *Biochemistry and Molecular Biology Education*, vol. 35, no. 1, pp. 57–63, 2007.
- [6] C. Wu, F. U. Rehman, J. Li et al., "Real-Time Evaluation of Live Cancer Cells by an in Situ Surface Plasmon Resonance and Electrochemical Study," *ACS Applied Materials & Interfaces*, vol. 7, no. 44, pp. 24848–24854, 2015.
- [7] Z. Zhu, M. Feng, L. Zuo et al., "An aptamer based surface plasmon resonance biosensor for the detection of ochratoxin A in wine and peanut oil," *Biosensors and Bioelectronics*, vol. 65, pp. 320–326, 2015.
- [8] H. Vaisocherová, H. Šípová, I. Víšová et al., "Rapid and sensitive detection of multiple microRNAs in cell lysate by low-fouling surface plasmon resonance biosensor," *Biosensors and Bioelectronics*, vol. 70, pp. 226–231, 2015.
- [9] F. Fernández, K. Hegnerová, M. Piliarik, F. Sanchez-Baeza, J. Homola, and M.-P. Marco, "A label-free and portable multi-channel surface plasmon resonance immunosensor for on site analysis of antibiotics in milk samples," *Biosensors and Bioelectronics*, vol. 26, no. 4, pp. 1231–1238, 2010.
- [10] X. Wang, S. Zhan, Z. Huang, and X. Hong, "Review: Advances and applications of surface plasmon resonance biosensing instrumentation," *Instrumentation Science and Technology*, vol. 41, no. 6, pp. 574–607, 2013.
- [11] B. Liedberg, C. Nylander, and I. Lunström, "Surface plasmon resonance for gas detection and biosensing," *Sensors and Actuators*, vol. 4, pp. 299–304, 1983.
- [12] S. Baumgarten and R. Robelek, "Surface plasmon resonance (SPR) sensors for the rapid, sensitive detection of the cellular response to osmotic stress," *Sensors and Actuators B: Chemical*, vol. 156, no. 2, pp. 798–804, 2011.
- [13] Y. Liu, Q. Liu, S. Chen, F. Cheng, H. Wang, and W. Peng, "Surface plasmon resonance biosensor based on smart phone platforms," *Scientific Reports*, vol. 5, p. 12864, 2015.
- [14] C.-W. Wu, C.-Y. Chiang, C.-H. Chen, C.-S. Chiang, C.-T. Wang, and L.-K. Chau, "Self-referencing fiber optic particle plasmon resonance sensing system for real-time biological monitoring," *Talanta*, vol. 146, pp. 291–298, 2016.
- [15] D. Michel, F. Xiao, and K. Alameh, "A compact, flexible fiber-optic Surface Plasmon Resonance sensor with changeable sensor chips," *Sensors and Actuators B: Chemical*, vol. 246, pp. 258–261, 2017.
- [16] H. Guner, E. Ozgur, G. Kokturk et al., "A smartphone based surface plasmon resonance imaging (SPRi) platform for on-site biodetection," *Sensors and Actuators B: Chemical*, vol. 239, pp. 571–577, 2017.
- [17] S. Dutta, K. Saikia, and P. Nath, "Smartphone based LSPR sensing platform for bio-conjugation detection and quantification," *RSC Advances*, vol. 6, no. 26, pp. 21871–21880, 2016.
- [18] Z. Liu, Y. Wei, Y. Zhang et al., "A novel surface plasmon resonance sensor based on fiber butt-joint technology," *Sensors and Actuators B: Chemical*, vol. 221, pp. 1330–1334, 2015.
- [19] M. George, K. R. Aroom, H. G. Hawes, B. S. Gill, and J. Love, "3D Printed Surgical Instruments: The Design and Fabrication Process," *World Journal of Surgery*, vol. 41, no. 1, pp. 314–319, 2017.
- [20] G. Gaal, M. Mendes, T. P. de Almeida et al., "Simplified fabrication of integrated microfluidic devices using fused deposition modeling 3D printing," *Sensors and Actuators B: Chemical*, vol. 242, pp. 35–40, 2017.
- [21] K. D. D. Willis, E. Brockmeyer, S. E. Hudson, and I. Poupayrev, "Printed optics: 3D printing of embedded optical elements for

- interactive devices,” in *ACM Symposium on User Interface Software and Technology*, 2012.
- [22] T. L. Newcomb, A. M. Bruhn, B. Giles, H. M. Garcia, and N. Diawara, “Testing a Novel 3D Printed Radiographic Imaging Device for Use in Forensic Odontology,” *Journal of Forensic Sciences*, vol. 62, no. 1, pp. 223–228, 2017.
- [23] M. Sadia, A. Sośnicka, B. Arafat et al., “Adaptation of pharmaceutical excipients to FDM 3D printing for the fabrication of patient-tailored immediate release tablets,” *International Journal of Pharmaceutics*, vol. 513, no. 1-2, pp. 659–668, 2016.
- [24] A. Bonyár, H. Sántha, B. Ring, M. Varga, J. G. Kovács, and G. Harsányi, “3D Rapid Prototyping Technology (RPT) as a powerful tool in microfluidic development,” *Procedia Engineering*, vol. 5, pp. 291–294, 2010.
- [25] J. W. Zhao, Y. U. Hua Zhong, Y. Q. Wang, and Z. Liu, “Real time Characterization for Surface Wettibility of Cysteamine Self assembled Monolayers on Gold,” *Chemical Research in Chinese Universities*, vol. 19, pp. 464–468, 1998.
- [26] E. H. Williams, A. V. Davydov, A. Motayed et al., “Immobilization of streptavidin on 4H-SiC for biosensor development,” *Applied Surface Science*, vol. 258, no. 16, pp. 6056–6063, 2012.
- [27] V. H. Pérez-Luna, M. J. O’Brien, K. A. Opperman et al., “Molecular recognition between genetically engineered streptavidin and surface-bound biotin,” *Journal of the American Chemical Society*, vol. 121, no. 27, pp. 6469–6478, 1999.
- [28] S. Zhao and W. M. Reichert, “Influence of Biotin Lipid Surface Density and Accessibility on Avidin Binding to the Tip of an Optical Fiber Sensor,” *Langmuir*, vol. 8, no. 11, pp. 2785–2791, 1992.

Research Article

Electrically Tunable Diffraction Grating Based on Liquid Crystals

Chuen-Lin Tien ^{1,2}, Rong-Ji Lin,² Shu-Hui Su,² and Chi-Ting Horng ^{3,4}

¹Department of Electrical Engineering, Feng Chia University, Taichung 40724, Taiwan

²Ph.D. Program of Electrical and Communications Engineering, Feng Chia University, Taichung 40724, Taiwan

³Department of Ophthalmology, Fooyin University Hospital, Pingtung, Taiwan

⁴Department of Pharmacy, Tajen University, Pingtung, Taiwan

Correspondence should be addressed to Chi-Ting Horng; chitinghorng@gmail.com

Received 6 February 2018; Accepted 3 April 2018; Published 20 June 2018

Academic Editor: Daniel Ho

Copyright © 2018 Chuen-Lin Tien et al. This is an open access article distributed under the Creative Commons Attribution License, which permits unrestricted use, distribution, and reproduction in any medium, provided the original work is properly cited.

A periodic electric field is generated in the grating-like electrodes cell by an applied voltage and results in the reorientation of liquid crystals. The linearly polarized probe beam experienced periodic distribution of refractive index and formed a phase grating. He-Ne laser was used as the probe beam to detect the zeroth-order (o) and first-order (+1) diffraction intensities. The experimental results showed that the diffraction grating can be switched on by applying a small voltage. The optimal first-order diffraction efficiency is about 12%. The dependence of the first-order diffraction efficiency on the polarization of the probed beam is also discussed herein.

1. Introduction

Liquid crystal (LC) phase grating has numerous applications, such as laser beam steering, beam shaping, fiber-optic communications, highly efficient projection displays, wide-viewing and direct-view displays, and other modifications of light intensity or phase [1–9].

For nematic liquid crystals (NLCs) based phase grating, because the operation voltage changing the orientation of the molecular director is usually lower, depending on the dielectric anisotropy ($\Delta\epsilon$) of LCs, an effective refractive index (Δn) of the medium is experienced by a propagating beam and has become an ideal candidate as an electrically controllable device due to the large optical birefringence [3, 10–15].

There are several ways to fabricate the liquid crystals diffraction gratings. Gibbons et al. have shown liquid crystal grating by exposing a dye-doped polymer layer to an ultraviolet interference pattern. Chen et al. have shown a hybrid liquid crystal configuration to create a double-rubbed polyimide layer for polarization-independent grating [16–20]. Honma et al. have demonstrated multidomain alignment regions liquid crystal gratings through a microrubbing technique [12, 13]. Wen et al. have shown a dual-domain

polarization grating which consists of right- and left-handed twisted regions created from scribing a polyimide layer [5].

In this paper, we propose a simple phase grating with tunable diffraction efficiency by applying a small voltage. The grating-like patterning of the electric field for the alignment of liquid crystals is easy to achieve and results in the periodic distribution of refractive index. The physical mechanisms for the first-order diffraction efficiency versus polarization angles of the probed beam are also discussed.

2. Experiment

We studied the liquid crystals phase grating in 25 μm -thick LC cell containing homogeneously aligned E7. The cell is with grating-like electrode width $w = 15 \mu\text{m}$. An LC mixture (E7) with $\Delta\epsilon = 14.4$ (dielectric constants at 1kHz) and $\Delta n = 0.218$ (refractive indices difference at $\lambda = 633 \text{ nm}$ and $T = 20^\circ\text{C}$) was injected into the cell via capillary flow. Figure 1(a) shows the experimental setup for characterizing the liquid crystals phase grating. He-Ne laser ($\lambda = 633 \text{ nm}$) was used as the probe beam. The transmission axis of the linear polarizer was set in the x-direction. An AC power supply ($\sim 1 \text{ kHz}$) applied voltage to the grating-like electrode cell and produced the periodic electric field on the cell and resulted in the periodic

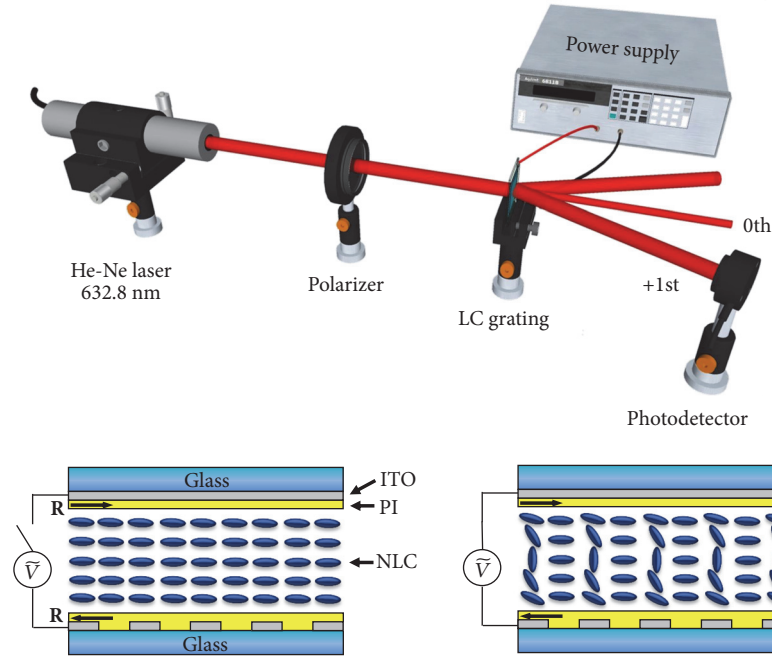


FIGURE 1: (a) Experimental setup for characterizing the performance of the phase grating. (b) The periodic distribution of refractive index of liquid crystals with an external ac voltage.

distribution of the refractive index of liquid crystals, as shown in Figure 1(b). The measured diffraction signals for the zeroth and the first order were detected by the photodetectors and recorded by the computer.

3. Results and Discussions

First, the diffraction intensities of the liquid crystal gratings in the zeroth and the first orders were recorded as a function of time, with an applied voltage of $\sim 4.0V$, as shown in Figure 2. The x -linearly polarized light from a He-Ne laser light source is normally incident on the sample; the zeroth-order diffraction rapidly decayed and the first-order diffraction was raised as the voltage was in “on” state. The diffraction intensities rise or decay to a stable level at $t=250$ ms. Next, the voltage was in “off” state at $t=3250$ ms; the zeroth-order diffraction was gradually increased and the first-order diffraction was gradually raised to an initial state at $t=\sim 3800$ ms.

Figure 3(a) plots the first-order diffraction intensity versus voltage for a liquid crystal phase grating formed from the periodic grating-like electrodes cell. The threshold voltage occurred at 2.0 V. After 2.0 V, the diffraction intensity gradually grew. The shape of the first-order diffraction versus voltage curve was indicated; as the voltage is increased to 4.0 V, the liquid crystal director orientation may tend to be homeotropically aligned in the electrical field, and the linearly polarized probe beam in the x -direction experienced the difference in refractive index modulation between electrode and nonelectrode stripes zones, which was significant. From 4.0 V to 10.0 V, the diffraction intensity gradually decays. The phenomenon is speculated to be the result of the disordering of the alignment of liquid crystals in

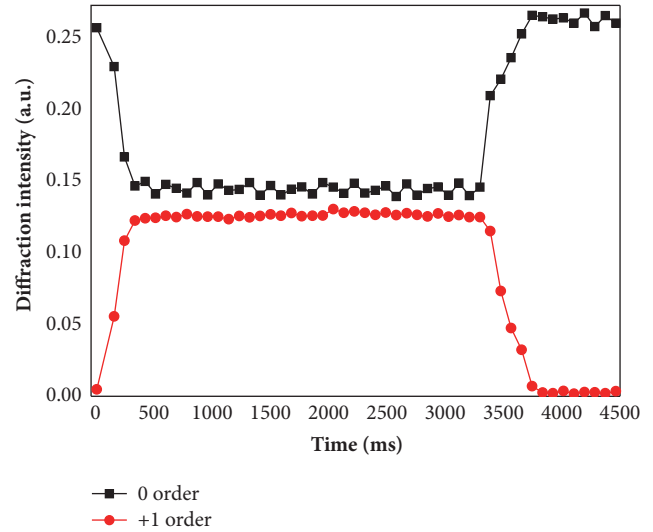


FIGURE 2: The diffraction intensities of the liquid crystal gratings in zeroth and the first orders were recorded as a function of time, using an applied voltage of $\sim 4.0V$.

the nonelectrode domains due to the edge effect of the electric field, reducing the difference in the refractive index modulation. After 10.0V, the first-order diffraction decays to a stable level. Figure 3(b) shows the images of the diffraction signals taken at 0, 2, 4, 10, and 20 V. At 0 V, only the zeroth-order diffraction signal exists; at 2 V, the first-order diffraction appears and the high order diffraction signals (4^{th} -order diffraction) can be observed; at 4 V, the first-order diffraction becomes the brightest and the 6^{th} -order diffraction signals can be observed; at 10.0 V and 20.0V, the

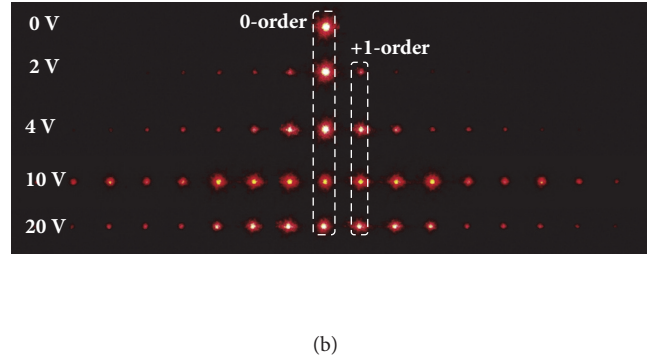
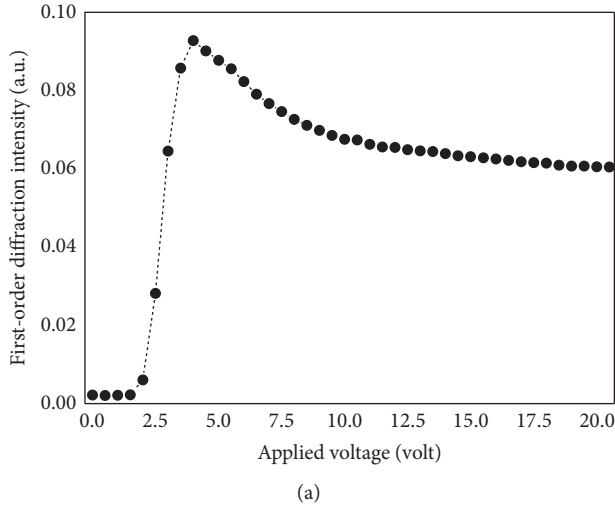


FIGURE 3: (a) The first-order diffraction intensity versus voltage for a liquid crystal phase grating formed from the periodic grating-like electrodes cell. (b) Diffraction patterns at different applied voltages: 0, 2, 4, 10, and 20 V, respectively.

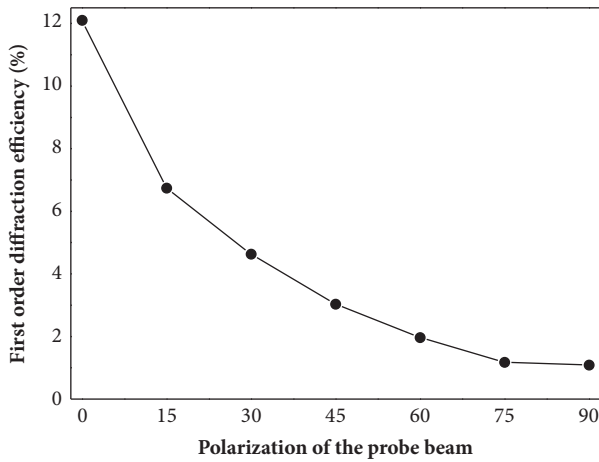


FIGURE 4: The diffraction efficiency of the first-order beams versus polarization of the probe beam with applied voltage $\sim 4.0V$.

first-order diffraction signal decays, and 8th-order diffraction signals can be observed.

Figure 4 shows the measured diffraction efficiency of the first-order beams with various polarization of the probe beam with applied voltage $\sim 4.0V$. The first-order diffraction efficiency η_1 is defined as the ratio between the intensity of 1st diffracted order and the total intensity at $V = 0$, described by

$$\eta_1 = \frac{I_1}{I_0} \quad (1)$$

The polarization of the probed beam is adjusted by rotating a polarizer from 0° to 90° corresponding to the adjustment of the polarization of the probe beam from x polarized to y polarized. The intensity of the probe beam maintains a constant value as the polarization is adjusted. The polarization angles of the probed beam are 0° , 15° , 30° , 45° , 60° , 75° , and 90° , respectively. When the polarization angle is at 0° , the

probe beam experiences ordinary (n_o) and extraordinary (n_e) refractive indices in the regions with and without the grating-like electrode stripes of the liquid crystal grating, respectively. The modulation of the refractive indices $\Delta n = n_e - n_o$ causes the phase grating effect in liquid crystals. The first diffraction efficiency η_1 is $\sim 12.0\%$. In considering the polarization angle other than the x polarization (0°), the effective refractive index experienced by the probed beam is a function of the polarization angle, according to [21]

$$n_{\text{eff}}(\theta) = \left(\frac{n_o n_e}{n_o^2 \cos^2 \theta} + n_e^2 \sin^2 \theta \right)^{1/2} \quad (2)$$

where θ is the angle between the x -axis and the polarization of the probe beam. As the polarization angle is adjusted from 0° to 90° , the effective refractive index n_{eff} experienced by the beam in the regions without the electrode stripe is reduced; the refractive index is constant in the regions with the electrode stripe. The modulation of the refractive index influences the phase grating. Therefore, the decrease in the anisotropy of the refractive index weakens the phase grating effect. The phase grating effect gradually decays as the polarization angle is increased. When the probe beam is linearly polarized in the y direction (90°) it experiences almost the same ordinary refractive index in the regions with and without the electrode stripe. The first diffraction efficiency η_1 is $\sim 1.1\%$. The results reveal that the phase grating effect is directly influenced by the polarization of the probe beam and can be switchable by adjusting the polarization of the probe beam.

4. Conclusions

In summary, the reorientation of liquid crystals can be obtained by applying external voltage in the grating-like electrodes cell; the linearly polarized probe beam experienced periodic distribution of refractive index, resulting in the

liquid crystal phase grating. The zeroth-order and the first-order diffraction intensities were probed by a He-Ne laser. The diffraction grating can be switched on by applying a small voltage (~ 2.0 V). The optimal first-order diffraction efficiency is about 12%. The first-order diffraction efficiency can also be tuned from 12.0% to 1.1% by adjusting the polarization of the probe beam.

Data Availability

The data used to support the findings of this study are available from the corresponding author upon request.

Conflicts of Interest

The authors declare that they have no conflicts of interest.

Acknowledgments

This work was supported by the Ministry of Science and Technology (MOST) of Taiwan under Grant MOST 106-2221-E-035-072-MY2. The authors also appreciate the Precision Instrument Support Center of Feng Chia University for providing the measurement facilities.

References

- [1] D. J. Field, "Relations between the statistics of natural images and the response properties of cortical cells," *Journal of the Optical Society of America A: Optics, Image Science & Vision*, vol. 4, no. 12, p. 2379, 1987.
- [2] H. Murai, "Electro-optic properties of liquid crystal phase gratings and their simulation using a homogeneous alignment model," *Liquid Crystals*, vol. 15, pp. 627–642, 1993.
- [3] J. Chen, P. J. Bos, H. Vithana, and D. L. Johnson, "Electro-optically controlled liquid crystal diffraction grating," *Applied Physics Letters*, vol. 67, no. 18, pp. 2588–2590, 1995.
- [4] J. N. Eakin, Y. Xie, R. A. Pelcovits, M. D. Radcliffe, and G. P. Crawford, "Zero voltage Freedericksz transition in periodically aligned liquid crystals," *Applied Physics Letters*, vol. 85, no. 10, pp. 1671–1673, 2004.
- [5] B. Wen, R. G. Petschek, and C. Rosenblatt, "Nematic liquid-crystal polarization gratings by modification of surface alignment," *Applied Optics*, vol. 41, no. 7, p. 1246, 2002.
- [6] L. Komitov, G. P. Bryan-Brown, E. L. Wood, and A. B. Smout, "Alignment of cholesteric liquid crystals using periodic anchoring," *Journal of Applied Physics*, vol. 86, no. 7, pp. 3508–3511, 1999.
- [7] C. Rosenblatt, "Nanostructured surfaces: scientific and optical device applications," *Molecular Crystals and Liquid Crystals*, vol. 412, no. 1, pp. 117–134, 2004.
- [8] T. Shioda, B. Wen, and C. Rosenblatt, "Step-wise Fréedericksz transition in a nematic liquid crystal," *Journal of Applied Physics*, vol. 94, no. 12, p. 7502, 2003.
- [9] G. P. Sinha, C. Rosenblatt, and L. V. Mirantsev, "Disruption of surface-induced smectic order by periodic surface corrugations," *Physical Review E: Statistical, Nonlinear, and Soft Matter Physics*, vol. 65, no. 4, Article ID 041718, 2002.
- [10] S. Varghese, G. P. Crawford, C. W. Bastiaansen, D. K. de Boer, and D. J. Broer, "Microrubbing technique to produce high pretilt multidomain liquid crystal alignment," *Applied Physics Letters*, vol. 85, no. 2, pp. 230–232, 2004.
- [11] S. Varghese, S. Narayanankutty, C. W. M. Bastiaansen, G. P. Crawford, and D. J. Broer, "Patterned alignment of liquid crystals by μ -rubbing," *Advanced Material*, vol. 16, no. 18, pp. 1600–1605, 2004.
- [12] M. Honma and T. Nose, "Liquid-Crystal Reflective Beam Deflector with Microscale Alignment Pattern," *Japanese Journal of Applied Physics*, vol. 43, no. 12, pp. 8151–8155, 2004.
- [13] M. Honma, K. Yamamoto, and T. Nose, "Periodic reverse-twist nematic domains obtained by microrubbing patterns," *Journal of Applied Physics*, vol. 96, no. 10, pp. 5415–5419, 2004.
- [14] D. J. Versteeg, C. W. M. Bastiaansen, and D. J. Broer, "Influence of laser writing of polyimides on the alignment of liquid crystals," *Journal of Applied Physics*, vol. 91, no. 7, pp. 4191–4195, 2002.
- [15] M. Schadt, H. Seiberle, and A. Schuster, "Optical patterning of multi-domain liquid-crystal displays with wide viewing angles," *Nature*, vol. 381, pp. 212–215, 1996.
- [16] W. M. Gibbons, P. J. Shannon, S. T. Sun, and B. J. Swetlin, "Surface-mediated alignment of nematic liquid crystals with polarized laser light," *Nature*, vol. 351, pp. 49–50, 1991.
- [17] B. W. Lee and N. A. Clark, "Alignment of liquid crystals with patterned isotropic surfaces," *Science*, vol. 291, p. 2576, 2001.
- [18] L. Nikolova and T. Todorov, "Diffraction efficiency and selectivity of polarization holographic recording," *Optica Acta: International Journal of Optics*, vol. 31, no. 5, p. 579, 1984.
- [19] S. G. Cloutier, D. A. Peyrot, T. V. Galstian, and R. A. Lessard, "Measurement of permanent vectorial photoinduced anisotropy in azo-dye-doped photoresist using polarization holography," *Journal of Optics A: Pure and Applied Optics*, vol. 4, p. S228, 2002.
- [20] P. S. Ramanujam, "Evanescence polarization holographic recording of sub-200-nm gratings in an azobenzene polyester," *Optics Letters*, vol. 28, p. 2375, 2003.
- [21] C. Kuo, S. Huang, I. Jiang, and M. Tsai, "Multiguide directional coupler using switchable liquid-crystalline optical channels," *Journal of Applied Physics*, vol. 97, no. 10, p. 103113, 2005.

Research Article

Voltage-Controllable Guided Propagation in Nematic Liquid Crystals

Hsin-Yu Yao¹ and Shang-Min Yeh ²

¹Department of Ophthalmology, Kaohsiung Armed Forces General Hospital, Kaohsiung 802, Taiwan

²Department of Optometry, Central Taiwan University of Science and Technology, Taichung 40601, Taiwan

Correspondence should be addressed to Shang-Min Yeh; optom.yap@gmail.com

Received 27 April 2018; Accepted 28 May 2018; Published 14 June 2018

Academic Editor: Jia-De Lin

Copyright © 2018 Hsin-Yu Yao and Shang-Min Yeh. This is an open access article distributed under the Creative Commons Attribution License, which permits unrestricted use, distribution, and reproduction in any medium, provided the original work is properly cited.

Voltage-controllable guided channels are formed in a planar nematic liquid crystals cell. The director of liquid crystals can be aligned by applying external voltage, which results in a difference of the refractive index between two adjacent channels; therefore, the incidence beam can be coupled from one channel to another. First, we discussed the propagation of the beam and the self-focusing in a single channel; then we discussed the propagation of the beam and the coupling effect in the two channels. The results showed that the propagation of the beam can be selected in each channel by applying voltages in the two individual electrode channels.

1. Introduction

Optical waveguide elements play an important role in the applications of optical communication, optical signal processing, integrated optical circuits, and optical networking [1, 2]. Many devices have been designed for the split, combine, couple, and phase modulation of the optical signal systems [1, 3]. Controlling the path of the propagating beam is the primary aim of the optical switching system, and the optical signals can be transferred to different guided channels. Somekh *et al.* proposed the concept of optical waveguide arrays [3], and the potential for optical switching applications has attracted much attention. Haus *et al.* theoretically predicted that the optical signal switch can be achieved by the external control of the waveguide arrays [4, 5]. Christodoulides *et al.* predicted the existence of solitary waves in arrays, and such unique properties have developed all-optical signal processing [6]. Gia Russo *et al.* investigated guided light and found the directional characteristics in the layered crystalline media [7, 8]. Channin *et al.* studied the waveguide characteristics and discussed the voltage-addressable optical properties in a liquid-crystal medium [9, 10]. Aligned nematic liquid crystals are a good choice for large changes in optical properties, which can be easily

driven by applying external voltage. Tsai *et al.* investigated a multiguided directional coupler based on planar-aligned nematic liquid crystals and discussed the dependence of the coupling effect on the external voltage, the polarization of the incident beam, and the temperature [11, 12].

This work discusses guided light in a single channel and two channels, where the propagation of the beam can be selected in each channel by applying different voltage in the individual electrode channels. In addition, self-focusing and the coupling effect are discussed.

2. Preparation of Sample and Experimental Setup

The nematic liquid crystal (NLC) in this experiment is E7 (ne = 1.7462 and no = 1.5216 at 20°C for $\lambda = 589$ nm; nematic phase ranges = -10 to 60.5°C, from Merck). An empty cell is constructed with two indium-tin-oxide (ITO) coated glass plates. One of the two plates is etched with a two-stripe ITO pattern as the upper electrode, and the other plate is used as the grounding electrode. The spacing between the etched region and the nonetched region is 15 μm . These two plates are coated with polyimide film and rubbed parallel to the ITO electrode stripes (z -axis). The glass slides are separated by two

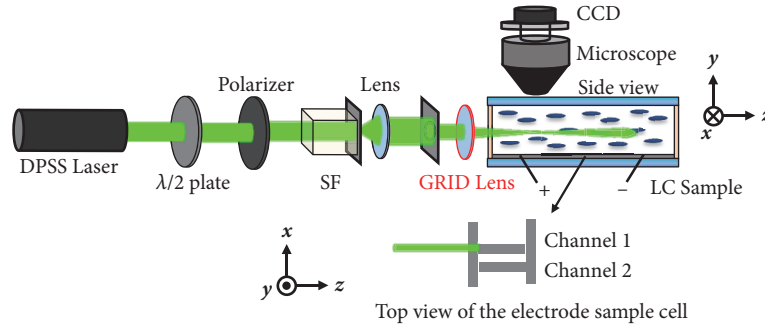


FIGURE 1: Experimental setup of voltage-controllable guided propagation in a nematic liquid crystals coupler.

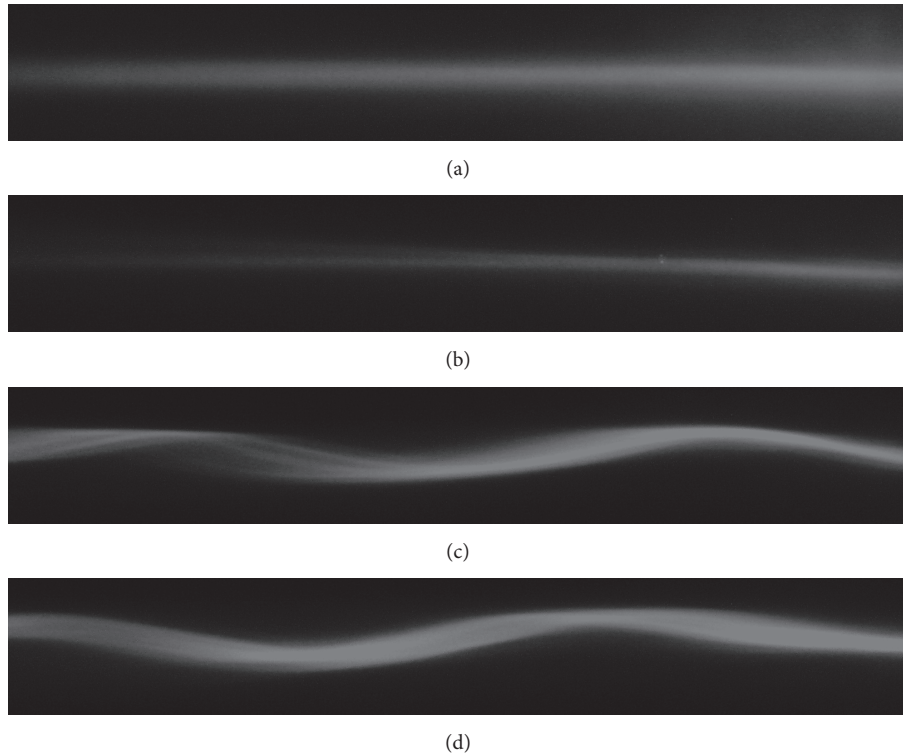


FIGURE 2: The guided light in a single channel by applying external voltages of (a) 0 V, (b) 1.5 V, (c) 2.2 V, and (d) 3.0 V.

25 μm thick plastic spacers, and the NLCs are injected into the empty cell to form a directional coupler.

Figure 1 presents voltage-controllable guided propagation in a nematic liquid crystals coupler. A linearly polarized (along the x -axis) beam of the 532 nm diode-pump solid-state laser (DPSS) impinges normally onto the side of the sample cell, which is focused on the cross-sectional region of the NLCs medium within the striped electrode of channel 1 using a grating singlet lens (GRID lens). The focal point is around 3.0 mm from the surface of the side glass, and the focus spot has a diameter of about 3.2 μm . A half-wave plate ($\lambda/2$ WP, for 532 nm) and a polarizer are inserted between the DPSS laser and the spatial filter (SF) in order to change the direction of polarization and the intensity of the incident beam. By applying an external voltage on the sample cell, the NLC molecules are reoriented, which results in the distribution of the refractive index in the medium, and the

optical channels are formed under a single or two electrode stripes.

Guided propagation, self-focusing, and the coupling effect are discussed in three different situations: guided light propagation (I) in a single channel, (II) in two channels by applying equal external voltages in each of the two electrode stripes, and (III) in two channels by applying the different external voltages in each of the two electrode stripes.

3. Results and Discussions

Figure 2 presents a guided light in a single channel by applying various external voltages. A laser beam, which is linearly polarized in the x -direction, is introduced into the channel from the left and propagates along the z -axis. With the applied voltage of $V_{\text{app}} = 0$ V, the guided light diverges after propagating distance $z = 25$ μm , as shown in Figure 2(a).

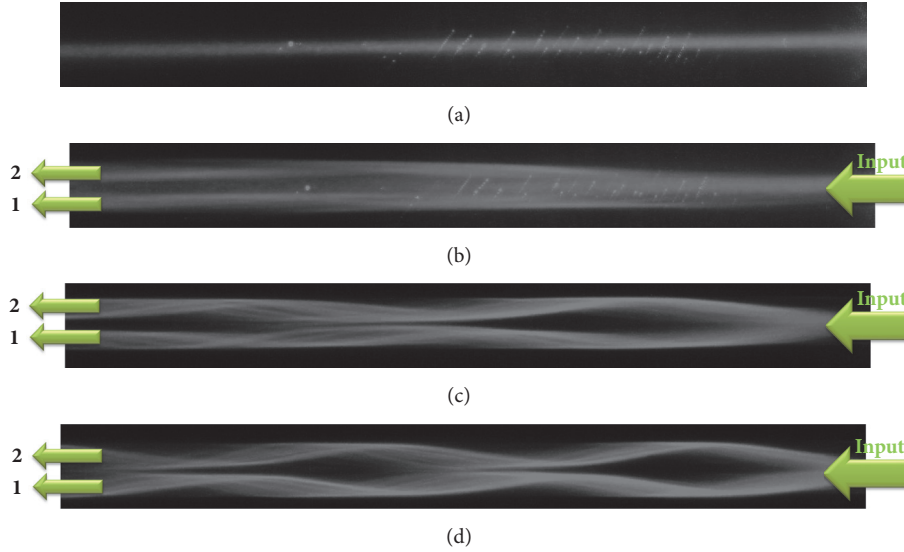


FIGURE 3: The guided light propagation by applying the same external voltages of (a) 0 V, (b) 1.5 V, (c) 2.2 V, and (d) 2.5 V in the two channels.

Initially, the liquid crystal molecules are horizontally aligned to the z -axis, while the x -direction polarized beam encounters the ordinary uniform refractive index distribution in the medium. With the increased applied voltage of $V_{\text{app}} = 1.5$ V, the guided light propagates in the channel, as shown in Figure 2(b). The liquid crystal molecules tend to align in the x -axis, while the x -direction polarized beam sees the extraordinary and ordinary refractive index of the liquid crystals in the guided channel and outside the channel, respectively, thus forming a waveguide-like structure. With the applied voltages of $V_{\text{app}} = 2.2$ V and 3.0 V, the self-focusing of the propagated beam is observed, as shown in Figures 2(c) and 2(d). The liquid crystal molecules around the channel can be reoriented due to the edge effect of the electric field, which forms an approximately gradient distribution of the refractive index around the channel in the medium.

Figure 3 presents the guided light propagation by applying the same external voltages of $V_{\text{app}} = 0$ V, 1.5 V, 2.2 V, and 2.5 V in the two channels. Initially, the incident beam is introduced into channel 1 with $V_{\text{app}} = 0$ V, as shown in Figure 3(a). With the applied voltage of $V_{\text{app}} = 1.5$ V, a part of the guided light gradually trends to channel 2, while part of the guided light still propagates in channel 1, as shown in Figure 3(b). Waveguide-like structures are formed, which results in total reflection in both channel 1 and channel 2. With $V_{\text{app}} = 2.2$ V and 2.5 V, each of the two beams travels back and forth in the vicinity of its channel, as shown in Figures 3(c) and 3(d). An approximate gradient distribution of the refractive index around the two channels is formed, which results in self-focusing in each channel.

Figure 4 presents the guided light propagation by applying fixed voltage $V_{\text{app}}(1) = 2.2$ V in channel 1 and applying voltage $V_{\text{app}}(2) = 0$ V, 1.5 V, 2.2 V, and 2.8 V in channel 2, which correspond to Figures 4(a)–4(d), respectively. Initially, the incident beam is introduced into channel 1, and self-focusing is observed, as shown in Figure 4(a). At $V_{\text{app}}(2)$

$= 1.5$ V (i.e., $V_{\text{app}}(1)$ is larger than $V_{\text{app}}(2)$), a small part of the guided light gradually couples to channel 2, as shown in Figure 4(b). In the condition of $V_{\text{app}}(2) = 2.2$ V (i.e., $V_{\text{app}}(1)$ is equal to $V_{\text{app}}(2)$), the coupling effect is clearly observed, and the propagation behavior seems to be the same in both channel 1 and channel 2, as shown in Figure 4(c). At $V_{\text{app}}(2) = 2.8$ V (i.e., $V_{\text{app}}(1)$ is smaller than $V_{\text{app}}(2)$), a large part of the guided light gradually couples to channel 2, as shown in Figure 4(d). The results show that the propagation of the incident beam can be easily tuned in channel 1 or in channel 2 due to the distribution of the refractive index when applying external voltage.

4. Conclusions

In summary, voltage-controllable guided channels are formed in a planar nematic liquid crystals cell. Nematic liquid crystal molecules can be easily reoriented by applying external voltage, which results in the difference of the refractive index between two neighboring channels. Therefore, the incidence beam can be coupled from one channel to another.

First, we discussed the propagation properties of the beam in a single channel. The self-focusing of the light can be observed at $V_{\text{app}} = 2.2$ V and 3.0 V. Then we discussed the guided light propagation by applying the voltages in the two channels; the beam coupled from one channel to another can be observed. The results show that the propagation of the incident beam can be easily tuned in each of the two channels, due to the distribution formation of the refractive index by applying external voltage.

Data Availability

The authors confirm that the data supporting the findings of this study are available within the article.

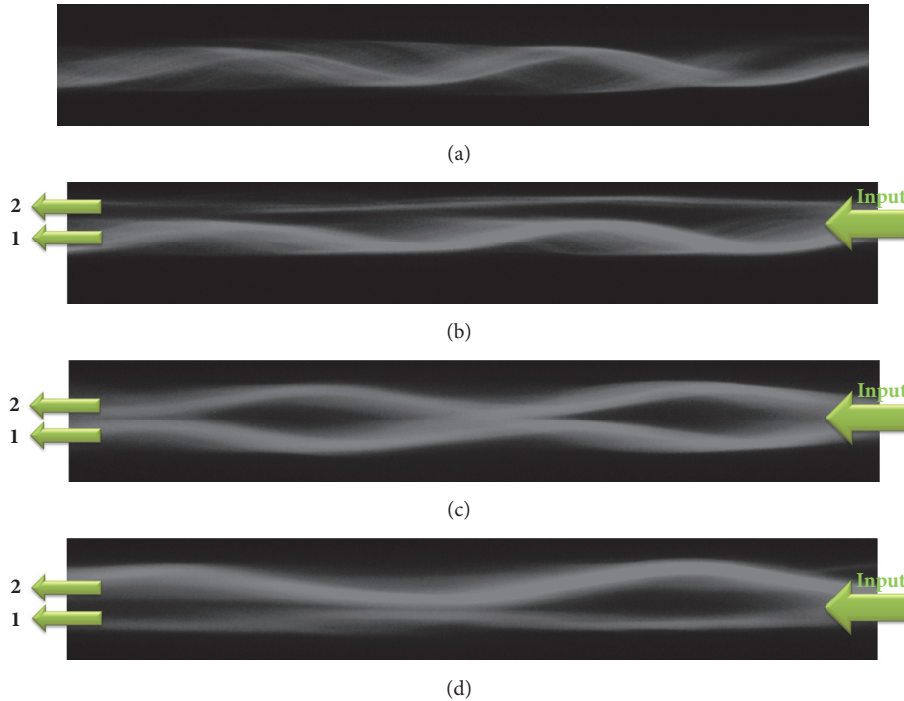


FIGURE 4: The guided light propagation by applying the fixed voltage of $V_{\text{app}}(1) = 2.2$ V in channel 1 and applying voltages of $V_{\text{app}}(2) = 0$ V, 1.5 V, 2.2 V, and 2.8 V in channel 2, which correspond to (a)–(d), respectively.

Conflicts of Interest

The authors declare that they have no conflicts of interest.

Acknowledgments

This study was financially supported by Clinical Research grants from Kaohsiung Armed Forces General Hospital, Taiwan (no. 106-17).

References

- [1] B. E. A. Saleh and M. C. Teich, *Fundamentals of Photonics*, Wiley, 2nd edition, 2007.
- [2] L. Wang, Y. Wang, and X. Zhang, “Embedded metallic focus grating for silicon nitride waveguide with enhanced coupling and directive radiation,” *Optics Express*, vol. 20, no. 16, pp. 17509–17521, 2012.
- [3] S. Somekh, E. Garmire, A. Yariv, H. L. Garvin, and R. G. Hunsperger, “Channel optical waveguide directional couplers,” *Applied Physics Letters*, vol. 22, no. 1, pp. 46–47, 1973.
- [4] S. F. Su, L. Jou, and J. Lenart, “A Review on Classification of Optical Switching Systems,” *IEEE Communications Magazine*, vol. 24, no. 5, pp. 50–55, 1986.
- [5] H. A. Haus and L. Molter-Orr, “Coupled Multiple Waveguide Systems,” *IEEE Journal of Quantum Electronics*, vol. 19, no. 5, pp. 840–844, 1983.
- [6] D. N. Christodoulides and R. I. Joseph, “Discrete self-focusing in nonlinear arrays of coupled waveguides,” *Optics Express*, vol. 13, no. 9, pp. 794–796, 1988.
- [7] D. P. Gia Russo and J. H. Harris, “Wave propagation in anisotropic thin-film optical waveguides,” *Journal of the Optical Society of America*, vol. 63, no. 2, pp. 138–145, 1973.
- [8] W. K. Burns and J. Warner, “Mode dispersion in uniaxial optical waveguides*,” *Journal of the Optical Society of America*, vol. 64, no. 4, p. 441, 1974.
- [9] D. J. Channin, “Optical waveguide modulation using nematic liquid crystal,” *Applied Physics Letters*, vol. 22, no. 8, pp. 365–366, 1973.
- [10] J. P. Sheridan, J. M. Schnur, and T. G. Giallorenzi, “Electro-optic switching in low-loss liquid-crystal waveguides,” *Applied Physics Letters*, vol. 22, no. 11, pp. 560–561, 1973.
- [11] M.-S. Tsai, C.-T. Kuo, S.-Y. Huang, C.-C. Shih, and I.-M. Jiang, “Voltage-controlled multiguide directional coupler formed in a planar nematic liquid crystal film,” *Applied Physics Letters*, vol. 85, no. 6, pp. 855–857, 2004.
- [12] C. Kuo, S. Huang, I. Jiang, and M. Tsai, “Multiguide directional coupler using switchable liquid-crystalline optical channels,” *Journal of Applied Physics*, vol. 97, no. 10, pp. 103–113, 2005.

Research Article

Light Leakage of Multidomain Vertical Alignment LCDs Using a Colorimetric Model in the Dark State

Chuen-Lin Tien ^{1,2}, Rong-Ji Lin,² and Shang-Min Yeh ³

¹Department of Electrical Engineering, Feng Chia University, Taichung 40724, Taiwan

²Ph.D. Program of Electrical and Communications Engineering, Feng Chia University, Taichung 40724, Taiwan

³Department of Optometry, Central Taiwan University of Science and Technology, Taichung 40601, Taiwan

Correspondence should be addressed to Shang-Min Yeh; optom.yap@gmail.com

Received 30 March 2018; Accepted 30 April 2018; Published 3 June 2018

Academic Editor: Jia-De Lin

Copyright © 2018 Chuen-Lin Tien et al. This is an open access article distributed under the Creative Commons Attribution License, which permits unrestricted use, distribution, and reproduction in any medium, provided the original work is properly cited.

Light leakage from liquid crystal displays in the dark state is relatively larger and leads to a degraded contrast ratio and color shift. This work describes a novel colorimetric model based on the Muller matrix that includes depolarization of light propagating through liquid crystal molecules, polarizers, and color filters. In this proposed model, the chromaticity can be estimated in the bump and no-bump regions of an LCD. We indicate that the difference between simulation and measurement of chromaticity is about 0.01. Light leakage in the bump region is three times that in no-bump region in the dark state.

1. Introduction

Many wide viewing-angle LCDs have been investigated and produced. In-Plane Switching (IPS) [1, 2] and Multidomain Vertical Alignment (MVA) [3–5] are widely used for high-end LCD products. The MVA LCD has a superior contrast ratio at normal viewing directions, wide viewing angle, and poor color dispersion. However, the light leakages in the dark state and color shift at an inclined angle have not yet been improved. Therefore, enhancing the contrast ratio and eliminating the light leakage in the dark state are important goals [6, 7]. Many conditions result in the light leakage such as light scattering from liquid crystals and the color filter, misalignment of crossed polarizers, and retardation of phase from liquid crystals [8, 9]. Polarization light scattering from the liquid crystals due to thermally excited orientation-based fluctuations of liquid crystal directors and light depolarization from the color filter due to pigment scattering have to be discussed [10, 11]. Investigating the colorimetric and photometric characteristics of LCDs, which include their major optical components, such as crossed polarizers, liquid crystals, color filters, and backlight modules, is interesting [12–14].

In this colorimetric model based on the Muller matrix, the transmission spectrum of each component is imported

and the light scattering from liquid crystals is ignored. The chromaticity coordinates can be estimated by measuring the degree of depolarization of the polarizer and the color filter. The error of chromaticity can be analyzed by introducing three backlight units and color resists. Finally, this work presents simulation and measurement results for a LCD module in the dark state, which demonstrate that a minimum difference exists in chromaticity, and light leakage in the bump region is three times larger than in no-bump region.

2. Analyzing Light Leakage in the Dark State

Figure 1 shows some LCD parts—the polarizer, analyzer, liquid crystal, and color filter. Two major parts in pixel design exist for an MVA: one is the bump region and the other is the no-bump region. In the bump region, due to the shape of the bump, the orientation of liquid crystal molecules is affected by the boundary condition. When linear polarized light passes through the bump region, phase retardation results in nonlinear polarization light. Finally, light leakage can exist in the bump region. Furthermore, transmittance in the bump region also influences chromaticity of an LCD. We should be concerned with calculating individually the optical performance of a pixel in the bump and no-bump region. Figure 2 presents vertical images of the subpixel

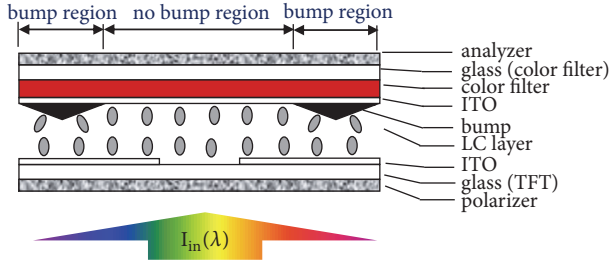


FIGURE 1: Scheme of MVA liquid crystal module.

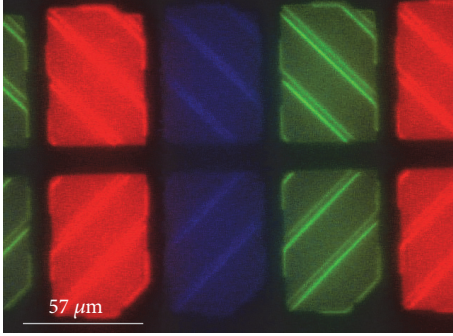


FIGURE 2: The vertical view images of subpixel color filter in dark state.

color filter at a normal direction in the dark state. The blue, green, and red lights are generated by the color filter with the existence of different color pigments. The oblique lines in each grid (subpixel) indicate the bump region, which is brighter than the no-bump region in the dark state due to light leakage. Light leakage can reduce colorimetric and photometric performance of liquid crystal displays in the dark state.

3. Colorimetric Calculation by Matrix Method

Depolarization occurs with the reduction in degree of polarization when light scatters through optical elements such as the polarizer or color filter. In (1), the light emanating out of the LCD through the polarizer, analyzer, liquid crystals, and color filter can be described using a matrix of optics.

$$P(\theta_1) D(d) P(\theta_2) \begin{pmatrix} I \\ Q \\ U \\ V \end{pmatrix} = \begin{pmatrix} I' \\ Q' \\ U' \\ V' \end{pmatrix}, \quad (1)$$

where $P(\theta)$ is the Muller matrix of polarizer; θ is the direction of the transmit axis and the subscript numbers of θ are the polarizer and analyzer, respectively; $D(d)$ is the Muller matrix of the depolarizer (including the polarizer and color filter); d is the degree of depolarization. Notably, I , Q , U , and V are known as stoke parameters of a quasimonochromatic plane wave that represents total intensity, horizontally or vertically polarized state, linear polarization along directions at angle

$\varphi = \pm 45^\circ$ to the x -axis, and the right or left circularly polarized state, respectively. Superscripts of stoke parameters describe the conditions of light propagating through the LCD module. Values of Q , U , and V vanish in the unpolarized state.

We assume the polarizer and analyzer comprise an ideal polarizer. The Muller matrix of the polarizer can be presented as follows:

$$p(\theta) = \frac{1}{2} \begin{pmatrix} 1 & \cos 2\theta & \sin 2\theta & 0 \\ \cos 2\theta & \frac{1 + \cos 4\theta}{2} & \frac{\sin 4\theta}{2} & 0 \\ \sin 2\theta & \frac{\sin 4\theta}{2} & \frac{1 - \cos 4\theta}{2} & 0 \\ 0 & 0 & 0 & 0 \end{pmatrix}, \quad (2)$$

where the Muller matrix in different directions of the transmit axes can be obtained by changing the value of θ .

Equation (3) derives the contrast ratio determined by the intensity of outgoing light with parallel polarizers ($\theta_1 = \theta_2 = 0$) divided by that with crossed polarizers ($\theta_1 = 0, \theta_2 = \pi/2$) in the dark state.

$$\text{CR}_{\text{PDP}} = \frac{I'_{//}}{I'_{\perp}} = \frac{(2-d)/4}{d/4} = \frac{2-d}{d}, \quad (3)$$

where $I'_{//}$ and I'_{\perp} are the total intensity of outgoing light with the polarization of polarizers parallel or orthogonally intersected with each other, respectively.

The colorimetric and photometric performance of LCDs depends on wavelength. That is, all mechanisms of light leakage should be determined in wavelength-related terms. Thus, considering the transmittance of color filters and polarizers, the degree of depolarization is function of wavelength. The $d(\lambda)$ can be estimated by (3) after measuring the contrast ratio. The intensity of outgoing light from the bump and no-bump regions is as follows:

$$\begin{aligned} I'_{\text{BUMP}}(\lambda) &= \frac{d(\lambda)}{4} \times T_{\text{CF}} \times T_{\text{BUMP}} \times T_{\text{LC.BUMP}} \\ &\quad \times T_{\text{PF}} \times T_{\text{TFT}} \times I_{\text{in}}(\lambda) \\ I'_{\text{No-BUMP}}(\lambda) &= \frac{d(\lambda)}{4} \times T_{\text{CF}} \times T_{\text{LC.No-BUMP}} \times T_{\text{PF}} \\ &\quad \times T_{\text{TFT}} \times I_{\text{in}}(\lambda), \end{aligned} \quad (4)$$

where T is transmittance of optical components, CF is the color filter, BUMP is the region with a bump, LC.BUMP is the region of the liquid crystal (LC) with a bump, PF is the polarizer or analyzer, TFT is thin-film transistors, and $I_{\text{in}}(\lambda)$ is light source spectrum.

To determine the chromaticity of the dark state, X_{bump} , Y_{bump} , and Z_{bump} tristimulus values of the Commission

International de l'Éclairage (CIE) XYZ color space through the bump region can be written in the following form [14]:

$$\begin{aligned}
X_{\text{bump}} &= k \int \frac{d(\lambda)}{4} \times T_{\text{CF}}(\lambda) \times T_{\text{BUMP}}(\lambda) \\
&\times T_{\text{LC.BUMP}}(\lambda) \times T_{\text{PF}}(\lambda) \times T_{\text{TFT}}(\lambda) \times \bar{x}(\lambda) \\
&\times I_{\text{in}}(\lambda) d\lambda \\
Y_{\text{bump}} &= k \int \frac{d(\lambda)}{4} \times T_{\text{CF}}(\lambda) \times T_{\text{BUMP}}(\lambda) \\
&\times T_{\text{LC.BUMP}}(\lambda) \times T_{\text{PF}}(\lambda) \times T_{\text{TFT}}(\lambda) \times \bar{y}(\lambda) \\
&\times I_{\text{in}}(\lambda) d\lambda \\
Z_{\text{bump}} &= k \int \frac{d(\lambda)}{4} \times T_{\text{CF}}(\lambda) \times T_{\text{BUMP}}(\lambda) \\
&\times T_{\text{LC.BUMP}}(\lambda) \times T_{\text{PF}}(\lambda) \times T_{\text{TFT}}(\lambda) \times \bar{z}(\lambda) \\
&\times I_{\text{in}}(\lambda) d\lambda,
\end{aligned} \tag{5}$$

where $\bar{x}(\lambda)$, $\bar{y}(\lambda)$, and $\bar{z}(\lambda)$ are the tristimulus values of the monochromatic stimuli and k is a constant.

Furthermore, the tristimulus values of light through the no-bump region $X_{\text{no.bump}}$, $Y_{\text{no.bump}}$, and $Z_{\text{no.bump}}$ can be written as follows:

$$\begin{aligned}
X_{\text{No.bump}} &= k \int \frac{d(\lambda)}{4} \times T_{\text{CF}}(\lambda) \times T_{\text{LC.NoBUMP}}(\lambda) \\
&\times T_{\text{PF}}(\lambda) \times T_{\text{TFT}}(\lambda) \times \bar{x}(\lambda) \times I_{\text{in}}(\lambda) d\lambda \\
Y_{\text{No.bump}} &= k \int \frac{d(\lambda)}{4} \times T_{\text{CF}}(\lambda) \times T_{\text{LC.NoBUMP}}(\lambda) \\
&\times T_{\text{PF}}(\lambda) \times T_{\text{TFT}}(\lambda) \times \bar{y}(\lambda) \times I_{\text{in}}(\lambda) d\lambda \\
Z_{\text{No.bump}} &= k \int \frac{d(\lambda)}{4} \times T_{\text{CF}}(\lambda) \times T_{\text{LC.NoBUMP}}(\lambda) \\
&\times T_{\text{PF}}(\lambda) \times T_{\text{TFT}}(\lambda) \times \bar{z}(\lambda) \times I_{\text{in}}(\lambda) d\lambda
\end{aligned} \tag{6}$$

When analyzing the colorimetric and photometric performance of LCDs, the X , Y , and Z values are difficult to interpret as the bump and no-bump regions coexist. The chromaticity coordinates x , y , and z have been developed and established by the Commission International de l'Éclairage (CIE). Equation (7) shows the relationship between chromaticity and tristimulus; as $x + y + z = 1$, describing chromaticity of the stimulus using chromaticity coordinates (x, y) is reasonable. To calculate optical performance of a pixel, the bump and no-bump regions should be investigated individually. This work sets ratio A , which is the bump area divided by the aperture area of a pixel, and the chromaticity (x, y) of module can be derived in the dark state using (8).

$$\begin{aligned}
x &= \frac{X}{X + Y + Z}, \\
y &= \frac{Y}{X + Y + Z}, \\
z &= \frac{Z}{X + Y + Z} \\
x &= \frac{X_{\text{bump}} \times A + X_{\text{No.bump}} \times (1 - A)}{(X_{\text{bump}} + Y_{\text{bump}} + Z_{\text{bump}}) \times A + (X_{\text{No.bump}} + Y_{\text{No.bump}} + Z_{\text{No.bump}}) \times (1 - A)} \\
y &= \frac{Y_{\text{bump}} \times A + Y_{\text{No.bump}} \times (1 - A)}{(X_{\text{bump}} + Y_{\text{bump}} + Z_{\text{bump}}) \times A + (X_{\text{No.bump}} + Y_{\text{No.bump}} + Z_{\text{No.bump}}) \times (1 - A)}
\end{aligned} \tag{7}$$

$$\tag{8}$$

4. Measurement

Figure 3 shows the measurement system, in which a pair of polarizers are superimposed onto both sides of the prepared sample; the polarization of polarizers is parallel or orthogonally intersected. The light source is a backlight unit with cold cathode fluorescent lamp (CCFL) (AUO, 59.23M01.002), which can provide luminance of $>7500 \text{ cd/m}^2$. The light from the backlight unit passes through the polarizer (Nitto, NPF-SEG1224DU), color resists (JSR Co., R874, G894, B877), analyzer, and spectrometer (Minolta, CS-1000), sequentially. The color filter is composed of three different color resists (R874, G894, B877 of R, G, and B, respectively). The distance between the first polarizer and backlight unit is 2cm such that the incident angle is $<10^\circ$, and the distance between

the two polarizers is 2cm. The colorimetric model can be implemented when the degree of depolarization $d(\lambda)$ is measured. This measurement must identify the contrast ratio that is equal to the luminance of the light passing through the parallel polarizers divided by that crossing the polarizers.

5. Simulation Results of Light Leakage in the Dark State

The degree of depolarization of RGB color resists is measured without addressing the transmittance of the black matrix. The contrast ratio of the color filter can be measured using various RGB color resists. If the liquid crystal and TFT layers are absent, the spectrum of outgoing light depends

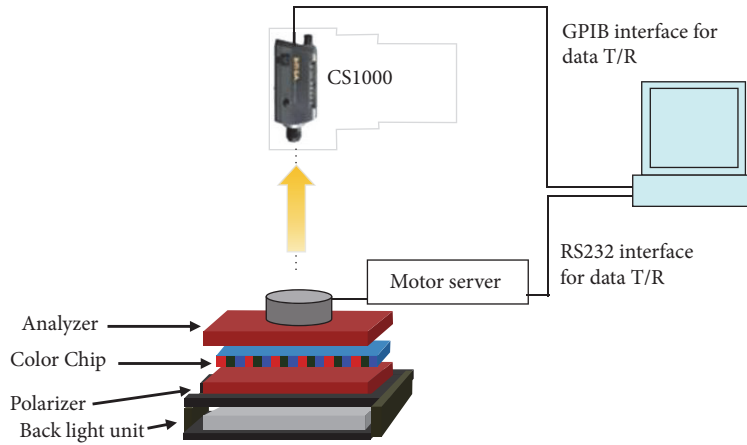


FIGURE 3: Auto-experimental system of measurement for contrast ratio of color resists.

BUMP	RED			GREEN			BLUE			White		
	x	y	Y	x	y	Y	x	y	Y	x	y	Y
	0.5711	0.3782	0.0093	0.2487	0.5269	0.0258	0.1454	0.0563	0.0040	0.253	0.271	0.013
No_BUMP	RED			GREEN			BLUE			White		
	x	y	Y	x	y	Y	x	y	Y	x	y	Y
	0.5015	0.4216	0.0054	0.1798	0.3679	0.0061	0.1552	0.0431	0.0009	0.251	0.245	0.004

FIGURE 4: Simulated result of chromaticity and photometry (Y) in bump and no-bump region.

on the transmission spectrum of the color filter, degree of depolarization, and spectrum of the backlight unit in (4). In the colorimetric model, the values of $Y_{parallel}$ and Y_{cross} are 14.05 and 0.002765, respectively, under the white point condition. This model indicates that the value of contrast ratio is 5110 for a color filter. The contrast ratio of modeling is close to the actual measurement result of 5500. It is a rapid way of evaluating optical performance of color filters when developing new color resists.

The colorimetric and photometric performance (x, y, Y) can be found (Figure 4) by considering the transmittance of the TFT, bump, and LC using (5) and (6). Without addressing the ratio of the bump area over a pixel area in this model, light leakage in the bump region is three times larger than no-bump region. By improving the contrast ratio of LCDs, light leakage caused by LC retardation in the bump region can be reduced.

Figure 5 shows the output spectra of measurement (solid line) and simulations (dotted line) of an LCD module in the dark state. The spectra peaks at about 440 nm, 550 nm, and 610 nm, represent the R, G, and B colors, respectively. The 485 nm and 585 nm peaks generated overlap transmission spectra between the B and G color filters. The 710 nm peak is from the backlight emitter, which has high transmittance in the R region. Figure 5 demonstrates that measurement and simulation results are similar. Figure 6 shows the measurement and simulation results for the colorimetric model in the dark state and bright state with three panel positions. The solid and dotted lines represent the measurement and simulation results, respectively. The points in the upper-right (down-left) side of figure are the bright state (dark

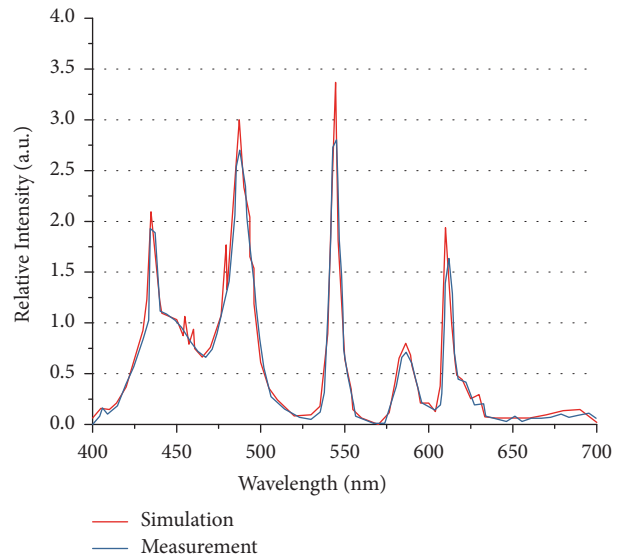


FIGURE 5: Output spectra of measurement and simulation of LCD module in the dark state.

state). In the bright state, the error of (x, y) chromaticity is about 0.003; in the dark state, chromaticity error is about 0.01. The large error in the dark state has two causes. One is the degree of depolarization in this colorimetric model. When the polarization of polarizers is crossed, light intensity is quite low, which results in fluctuations in the degree of depolarization in terms of wavelength. The other cause is error caused by manufacturing variation, such as polarizer

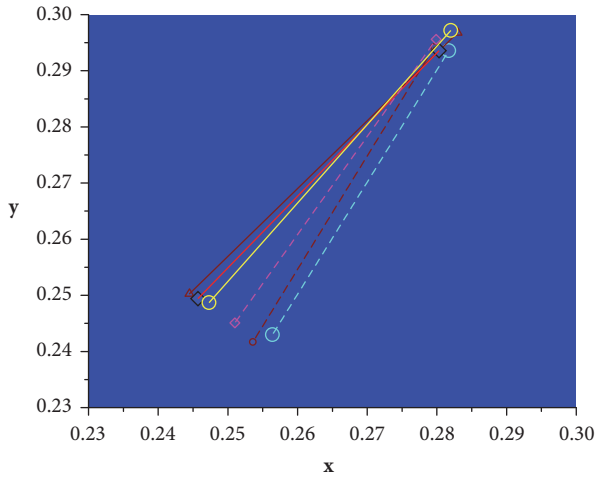


FIGURE 6: The chromaticity coordinates of measured and simulated results in the dark state and bright state.

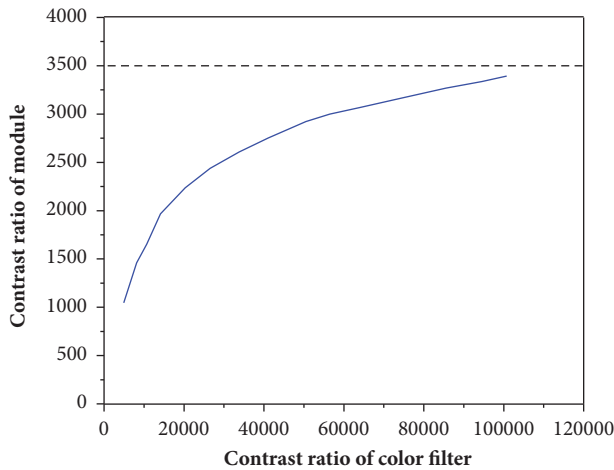


FIGURE 7: Simulation result for the contrast ratio performance of color filter and module.

misalignment or space in the cell gap variation. The low light intensity can be improved using a relatively brighter continuous light source. When degree of depolarization noise is minimized, estimating chromaticity of an LCD in the dark state is possible by measuring the degree of depolarization of color resists.

The contrast ratio is defined by $Y_{\text{bright}}/Y_{\text{dark}}$. Not only is the depolarization of the color filter an influential factor, but the light leakage in the bump area has an important role when calculating the contrast ratio. This model can evaluate the excellence of the contrast ratio of the LCD module when only improvements to the contrast ratio of the color filter are considered. Figure 7 shows the contrast ratio of the color filter, which increases with the contrast ratio of the LCD module when the extreme ratio of the LCD model is assumed to be about 3500. Actually, for a dispersion-type color filter, improving the contrast ratio of the color filter by 200% is difficult. Finally, the primary cause of contrast ratio deterioration of LCDs is light leakage from the bump region.

6. Conclusions

This work investigated the colorimetric and photometric properties of LCDs using a novel colorimetric model. This work demonstrates that the chromaticity coordinates of an LCD can be simulated accurately, and the proposed model can be utilized to optimize color LCDs with different optical components (excluding liquid crystals). Most importantly, this work thoroughly analyzes the colorimetric properties of LCDs and, in doing so, demonstrates that properly optimized LCDs use different backlights and color resists. Finally, the depolarization and retardation effects can be reduced to improve contrast ratio performance in an MVA-type LCD module.

Data Availability

The data used to support the findings of this study are available from the corresponding author upon request.

Conflicts of Interest

The authors declare that they have no conflicts of interest.

Acknowledgments

This research was supported by the Ministry of Science and Technology (MOST) of Taiwan under Grants MOST 106-2221-E-035-072-MY2.

References

- [1] S. Aratani, H. Klausmann, M. Oh-e et al., "Complete suppression of color shift in in-plane switching mode liquid crystal displays with a multidomain structure obtained by unidirectional rubbing," in *Proceedings of the 1997 Pacific Rim Conference on Lasers and Electro-Optics, CLEO/Pacific Rim*, p. 93, July 1997.
- [2] C.-H. Chen, F.-C. Lin, and H.-P. D. Shieh, "A Field Sequential Color LCD Based on Color Fields Arrangement for Color Breakup and Flicker Reduction," *Journal of Display Technology*, vol. 5, no. 1, pp. 34–39, 2009.
- [3] H. Chen, R. Zhu, M.-C. Li, S.-L. Lee, and S.-T. Wu, "Pixel-by-pixel local dimming for high-dynamic-range liquid crystal displays," *Optics Express*, vol. 25, no. 3, pp. 1973–1984, 2017.
- [4] H. Chen, G. Tan, M.-C. Li, S.-L. Lee, and S.-T. Wu, "Depolarization effect in liquid crystal displays," *Optics Express*, vol. 25, no. 10, pp. 11315–11328, 2017.
- [5] S. H. Hong, Y. H. Jeong, H. Y. Kim, H. M. Cho, W. G. Lee, and S. H. Lee, "Electro-optic characteristics of 4-domain vertical alignment nematic liquid crystal display with interdigital electrode," *Journal of Applied Physics*, vol. 87, no. 12, pp. 8259–8263, 2000.
- [6] T.-H. Yoon, G.-D. Lee, and J. C. Kim, "Nontwist quarter-wave liquid-crystal cell for a high-contrast reflective display," *Optics Express*, vol. 25, no. 20, pp. 1547–1549, 2000.
- [7] Q. Hong, T. X. Wu, X. Zhu, R. Lu, and S.-T. Wu, "Designs of wide-view and broadband circular polarizers," *Optics Express*, vol. 13, no. 20, pp. 8318–8331, 2005.
- [8] K. Okumoto, T. Tsuchiya, K. Yonemura et al., "A novel simulation method in In-Plane switching mode panel with

- considering light scattering behavior,” in *Proceedings of the 2015 SID International Symposium*, pp. 1555–1558, usa.
- [9] R. Lu, X. Zhu, S. Wu, Q. Hong, and T. Wu, “Ultrawide-View Liquid Crystal Displays,” *Journal of Display Technology*, vol. 1, no. 1, pp. 3–14, 2005.
- [10] M. Yoneya, Y. Utsumi, and Y. Umeda, “Depolarized light scattering from liquid crystals as a factor for black level light leakage in liquid-crystal displays,” *Journal of Applied Physics*, vol. 98, no. 1, Article ID 016106, 2005.
- [11] H. Chen, F. Peng, Z. Luo et al., “High performance liquid crystal displays with a low dielectric constant material,” *Optical Materials Express*, vol. 4, no. 11, pp. 2262–2273, 2014.
- [12] J. L. Pezzaniti, S. C. McClain, R. A. Chipman, and S.-Y. Lu, “Depolarization in liquid-crystal televisions,” *Optics Express*, vol. 18, no. 23, pp. 2071–2073, 1993.
- [13] M. Bass, *Handbook of Optics*, vol. 3, 1995.
- [14] G. Wyszecki and W. S. Stiles, *Color Science. Concepts and Methods, Quantitative Data and Formulae*, 2000.

Research Article

Green LED as an Effective Light Source for Curing Acrylate-Based Dental Resins in Combination with Irgacure 784

Katalin Bukovinszky,¹ Melinda Szalóki,¹ István Csarnovics,² Istvan Szabó,³ Sándor Kéki,⁴ Miklós Nagy ,⁴ and Csaba Hegedűs ¹

¹Department of Biomaterials and Prosthetic Dentistry, University of Debrecen, Debrecen, Hungary

²Department of Experimental Physics, University of Debrecen, Debrecen, Hungary

³Department of Solid State Physics, University of Debrecen, Debrecen, Hungary

⁴Department of Applied Chemistry, University of Debrecen, Debrecen, Hungary

Correspondence should be addressed to Csaba Hegedűs; hegedus.csaba.prof@dental.unideb.hu

Received 18 January 2018; Revised 5 March 2018; Accepted 15 March 2018; Published 23 April 2018

Academic Editor: Jia-De Lin

Copyright © 2018 Katalin Bukovinszky et al. This is an open access article distributed under the Creative Commons Attribution License, which permits unrestricted use, distribution, and reproduction in any medium, provided the original work is properly cited.

Low intensity green light emitting diodes (LED) were shown to be an effective light source to induce the photopolymerization of an acrylate-based photocurable dental restorative resin mixture of bisphenol A glycerolate dimethacrylate (BisGMA), triethylene glycol dimethacrylate (TEGDMA), and diurethane dimethacrylate (UDMA), in combination with fluorinated diaryl titanocene (Irgacure 784). Dental matrices were prepared by the LED light source at different intensities. The mechanical properties, such as Vickers microhardness, compressive strength, diametric tensile strength, flexural strength, and *E*-modulus of the created samples, were investigated. The kinetics of the photopolymerization was followed by Raman spectroscopy and conversion values were determined. It was found that, despite its narrow-emission range centered at a wavelength of 531 nm, the green LED light source is suitable for the preparation of dental matrices with good mechanical properties and high conversion values.

1. Introduction

Photopolymerization [1] has become an essential tool in three-dimensional (3D) printing [2] and photolithography [3], in the construction of polymer electronics [4], optical materials [5], membranes [6], and coatings, and in surface modifications. The most common photopolymerization monomers are cyclic or linear epoxides (cationic) and acrylate-based monomers (radical) [1]. Acrylate-based photopolymers are important materials for cardiovascular applications [7], for in vivo drug delivery [8], and for minimally invasive procedures. Dimethacrylate-based resins have many applications in restorative dentistry, being used as adhesives and pit-and-fissure sealants, can be combined with silane-coated glass fillers to render the most widely used esthetic direct restorative material, and can be used as cementation agents and veneering materials [9–12]. Photopolymerization starts with exposure to a light source, the operation

wavelength of which depends on the photoinitiator added. For the photopolymerization process to be effective, the spectral radiant power of the light-curing unit must fall within the spectral range required to activate the photoinitiator present in the resin [13].

Several types of light-curing units are available for photoactivation of photopolymerizable dental resins. The contemporary technologies include quartz-tungsten-halogen lights (QTH), plasma arc lights, high-intensity QTH lights, and light emitting diodes (LED). The most common photoinitiator in dental practice is camphorquinone (CQ) in combination with tertiary amines as coiniciators [14]. CQ has a relatively broad absorption in the ultraviolet (UV) region and an absorption band in the visible region with a maximum wavelength (λ_{\max}) of 468 nm [14, 15]. Unfortunately, CQ has a low molar absorption coefficient in the visible region of the spectrum. Normally, UV light would be used in combination with CQ, but due to the risk of tissue burning

and carcinogenic and photoallergic effects, the application of irradiation below 400 nm is restricted in dental applications, and visible light is favored [16].

To overcome the relatively low initiation efficiencies, other high-performance visible photoinitiators have been developed for resins used in specialty applications, such as direct laser imaging, holography, or photopolymerization color printing [17]. Fluorinated diaryl titanocene (Irgacure 784) proved to be effective for initiating the polymerization of acrylate monomers under visible light exposure, having high photosensitivity and absorbing light in a large wavelength region of up to 550 nm, meaning it may be suitable for use in dental composites [18]. Another advantage of Irgacure 784 is that it is not reliant on diffusion controlled electron transfer reactions because it undergoes unimolecular decomposition [19]. However, the application of Irgacure 784 may have the disadvantage of residual color when used in excess, but this issue is also present in CQ/amine initiator systems [20] and could be overcome by optimizing the amount of initiator or could be lowered by the application of fillers.

The degree of conversion of the dental resin, which is the marker of polymerization efficiency, depends on the correlation between the spectral distribution of the light source and the absorption spectra of the photoinitiator [21]. Essentially, QTH light sources have been used for the photopolymerization of dental resins, but their application is energetically inefficient, and their effective lifetime is limited by degradation [22]. On the other hand, LED have many intrinsic advantages making them ideally suited for the photopolymerization of oral biomaterials. Their first major advantage for photopolymerization is their high energy efficiency in terms of energy required for a cure cycle. LED have high durability, meaning a long lifetime with little degradation of light output. The second major advantage is that their typical spectral line width is 5–20 nm. So, as the photoinitiators present in oral biomaterials have light absorption spectra with distinct maxima, effective and rapid photopolymerization could result if the wavelength of the LED was chosen in this range [21].

While the photocuring of dimethacrylate-based dental resins in combination with Irgacure 784 and LED light source has many advantages, similar to other free-radical polymerizations, it may be strongly inhibited by free-radical scavengers such as oxygen. However, the inhibition effect of oxygen was studied in detail by Gauthier et al. for bisphenol A glycerolate dimethacrylate:triethylene glycol dimethacrylate-(Bis-GMA:TEGDMA-) based dental composites [23]. They showed that, with the proper selection of the monomer viscosity and polymerization temperature, oxygen inhibition only occurs in the surface layer, to a depth of about 20 μm , and below that approximately 90% conversion could be reached.

To the best of our knowledge, no studies have been published on the preparation of dental acrylate resins using Irgacure 784 as a photoinitiator in combination with a green LED light source. Herein, we report on our investigation into the effect of a LED light-curing unit on the mechanical properties and conversion rates of acrylate-based experimental resin containing Irgacure 784 photoinitiator.

2. Experimental Materials and Methods

2.1. Preparation of Experimental Resin Matrix. The photocurable resin matrix was a mixture of bisphenol A glycerolate dimethacrylate (BisGMA), triethylene glycol dimethacrylate (TEGDMA) (Sigma-Aldrich Co., St. Louis, MO, US), and diurethane dimethacrylate (UDMA) (Sigma-Aldrich Chemie GmbH, Steinheim, Germany) monomers in a 21.4 : 25.4 : 53.3 weight ratio, respectively, containing 2% (m/m) Irgacure 784 (BASF Hungary Ltd.) as a photoinitiator. Dimethylformamide (DMF, high-performance liquid chromatography (HPLC) grade) was obtained from Sigma-Aldrich. The materials were used without further purification.

2.2. Photopolymerization of the Samples. To exclude oxygen, the photocuring process was performed under laminate conditions. The experimental resin was inserted into a Teflon mold and the top surface was flattened by a polyester strip (to seal the surface from oxygen) as is shown in Figure 1(b). Light activation was performed for 30 s with the LED at light intensities of 0.7, 1.0, 1.2, 1.4, 2.0, 4.0, and 6.0 mW/cm^2 . The photopolymerizations were done in a dark room, without any backlights. The specimen disks were 2 mm thick and 10 mm in diameter.

2.3. Light-Curing Unit Description. In our experiments, we used a light emitting diode light source (LED) (Megaled, 3 W green power LED, Hungary) unit in order to polymerize the experimental resin matrix. The emission range of the LED light source is centered at a wavelength of 531 nm. The full width at the half maximum is 32 nm, while the half width at the half maximum is 16 nm for our LED light source. The size of the irradiated region was 3 \times 3 cm. Therefore, the samples were irradiated through a cuboid, a tube with both sides open, which was covered inside with a highly reflective coating to make the irradiation spot more homogenous. The optical spectrum of the light source was measured with a fiber optical spectrophotometer (Ocean Optics, USB650, US). The intensity of the light source was measured by a power meter setup (ThorLabs, PM100, US). In addition, the spectral irradiance distribution of the light source was detected with a spectroradiometer (EKO Instruments, LS-100, Japan). The UV-vis spectra of the photoinitiator in toluene were recorded on an Agilent Cary 60 spectrophotometer (Agilent, Santa Clara, CA, US) in a quartz cuvette with a 1.00 cm optical length. A 3.00 cm^3 solution was prepared from the sample.

2.4. Resin Density, Extraction, and Water Swelling Experiments. The densities of the cured samples were determined in a pycnometer at 25°C, using water as the medium. For the swelling studies, three of the samples at different light intensities, 0.7, 1.0, 1.2, 1.4, 2.0, 4.0, and 6.0 mW/cm^2 , were placed in excess deionized water and were allowed to reach equilibrium at ambient temperature for a week. The surfaces of the wet disks were cautiously wiped dry and their weights were measured immediately. After 24 h, the cured samples were extracted with DMF in a Soxhlet-type extractor overnight. The extracted samples were dried in vacuum at 50°C for 2 days and their weight was measured.

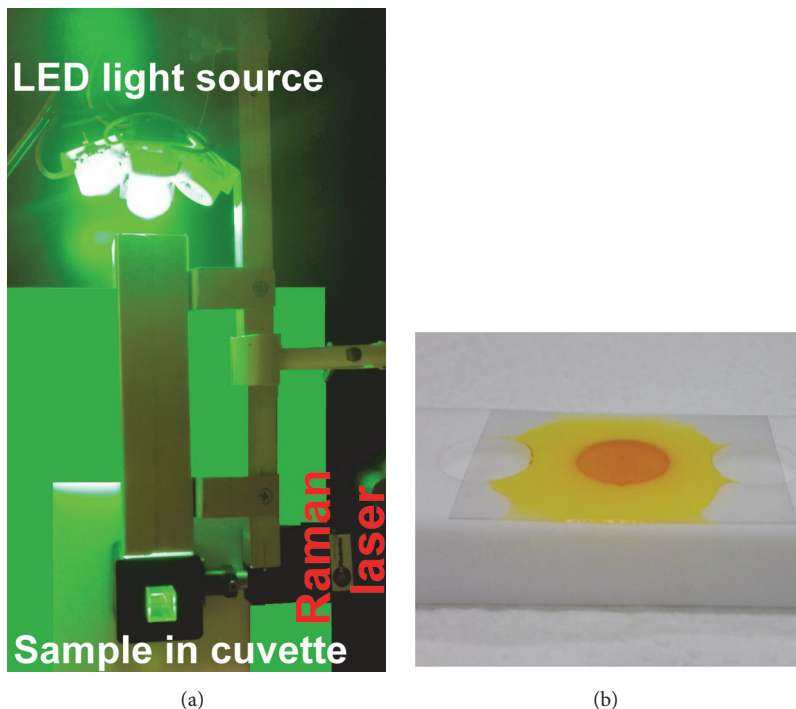


FIGURE 1: Experimental layout for Raman spectroscopy (a) and the laminated Teflon mold used for preparing the resins (b).

2.5. Characterization of Polymerization Kinetics of Experimental Resin with Raman Spectroscopy at Different Light Intensities. The Raman spectra were recorded with a system incorporating a waveguide spectrophotometer (Ocean Optics QE 6500, US), and the light source was a CW laser operating at 785 nm. As this wavelength is out of the absorption range of the photoinitiator, the laser light did not affect the photopolymerization process. The monomer was irradiated in a polystyrene cuvette and the spectra were taken before and after polymerization (Figure 1).

In addition, in situ investigation of the Raman spectra was completed; the spectra were recorded during the illumination every second. This measurement setting allows calculating and establishing the kinetics at different types of irradiation. With these measurements, the chosen light intensities varied between 0.7 and 10.0 mW/cm². The laser was focused to the center of the cuvette, so the spectral information was collected from the volume and not from the surface. The polymerization time was chosen as 250 s to allow for the front of the polymerization to reach the Raman source. The images, which display changes in composition and degree of conversion (α), were generated with OriginPro 8.0™ software.

2.6. Preliminary Vickers Microhardness Measurements. The specimens were prepared as described in Section and were stored at room temperature for 24 h before testing. At each light intensity, three samples were prepared ($n = 3$) and five microhardness indentations were made per specimen. Vickers microhardness measurements were made with a 100 g load for 20 seconds in a microhardness testing machine (Buehler Vickers Microhardness, Micromet 5103, US). In this

preliminary investigation, our aim was to choose the optimal light intensity for polymerization of the samples, where the Vickers microhardness data showed the best results. The subsequent mechanical measurements were performed at the chosen light intensity.

2.7. Diametral Tensile Strength Measurements. The uncured resin was placed in a Teflon mold and the samples were covered with a thin polyester foil. The polymerization of the samples was performed at a light intensity of 1.4 mW/cm² of the LED light source for 30 s. The size of the specimens was 3 mm thick and 6 mm in diameter. The diametral tensile stress (DTS) of the experimental resin was determined by a mechanical testing device (INSTRON 5544, US) equipped with 2-kN load cell at a crosshead speed of 1 mm/min. DTS was calculated from the maximum compression load (F) at the specimen fracture in a diametric position, with the following equation: $DTS = 2F/(\pi hd)$, where h is the height of the specimen, d is the diameter of the specimens, and π is a constant at 3.14.

2.8. Flexural Strength Measurements. The flexural strength of the experimental resin samples was investigated with a mechanical testing device (INSTRON 5544, US) equipped with 100-N load cell at a crosshead speed of 1 mm/min. The span distance was 18 mm. The three-point flexural strength tests were implemented on prismatic specimens. The samples were photopolymerized with the LED light source at 1.4 mW/cm² power density for 30 s in a Teflon mold. The cross section size of the specimens was 2 mm × 2 mm and 25 mm in length. In average, 14 specimens were prepared and stored at

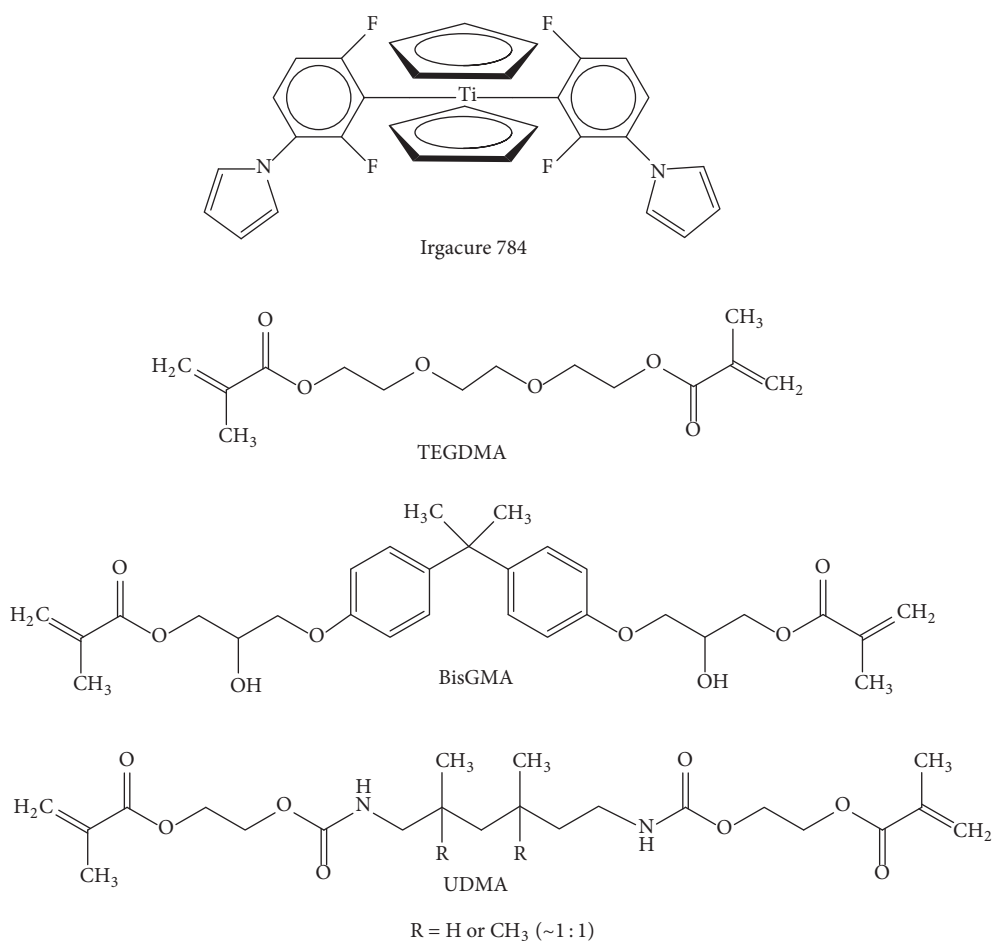


FIGURE 2: The chemical structure of the photoinitiator and acrylate monomers used in this study.

room temperature for 24 h before testing. The flexural stress and modulus (modulus of elasticity) data were calculated by MSZ EN ISO 178.

2.9. Compressive Strength Measurements. Compressive strength tests were performed with a mechanical testing analyzer (INSTRON 8874, High Wycombe, UK) equipped with 25-kN load cell. Fifteen cylindrical samples ($n = 15$) were created. The resin was inserted in a single increment into a Teflon mold, and the top surface was flattened by means of a polyester strip. For the sample preparation, the light activation was performed for 30 s at 1.4 mW/cm². The size of the specimens was 6 mm in height and 3 mm in diameter. The crosshead speed was 1 mm/min. The compressive data were calculated by MSZ EN ISO 604:2003.

3. Results and Discussion

3.1. Monomers and Light Source. Our resin contained a monomer mixture of BisGMA, TEGDMA, and UDMA (Figure 2) in a 21.4:25.4:53.3 weight ratio. Asmussen and Peutzfeldt [24] examined the influence of these monomers on the mechanical properties of experimental resin composites. They stated that for the designed mechanical properties of

dental composite resins it is best to apply monomers in this optimal ratio for that purpose. The aromatic monomer BisGMA is rigid compared to TEGDMA and UDMA. The urethane linkage in UDMA, the favorable stereochemistry, and the long chain in TEGDMA provide flexibility to these molecules. The application of more flexible monomers is expected to increase the conversion of polymerization.

The photoinitiator used was Irgacure 784, mixed to the matrix in 2% (m/m). In addition to the copolymer composition, the photoinitiator also influences the physical properties of the resins. Sabol et al. studied Irgacure 784 in an epoxy photopolymer and assumed that two absorptive photoproducts are generated during photoinitiation [25]. This photoinitiator does not require an electron donor to produce free radicals so it is suitable for the substitution of CQ in dental photopolymer systems. Irgacure 784 absorbs photons at the green exposing wavelength (λ) of 532 nm. The absorption of light quanta by Irgacure 784 causes reversible isomerization, resulting in an intermediary isomer with different absorption spectra, which can either relax and return to the original state or cause photocleavage, resulting in a stable acryl compound and an unstable titanocene diradical that can react with a reducing agent to form a stable transparent final product. Another possible method of forming a final

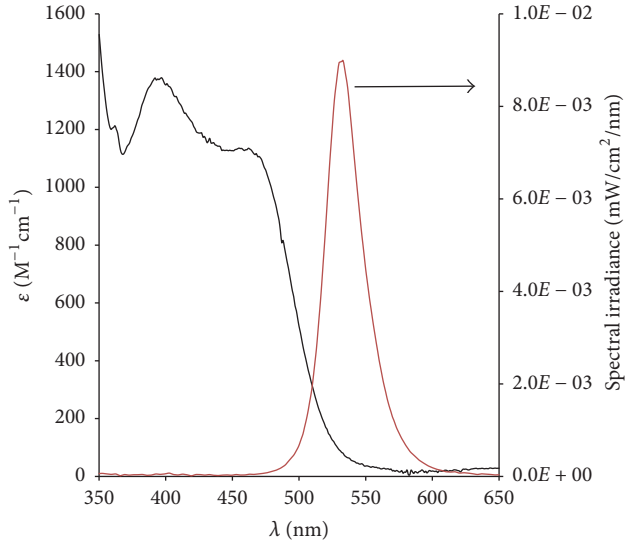


FIGURE 3: Ultraviolet-visible (Uv-vis) absorption spectrum of Irgacure 784 photoinitiator in toluene (left) and spectral irradiance distribution of the green LED light source.

stable product is the reaction of the isomer with a reactive component of the resin matrix [25].

Since we used a green LED light source to initiate the photopolymerization process, knowing the characteristics of the lamp and sensitivity of the initiator in the green region of visible light is important. The transmittance spectrum of the LED lamp and the absorption spectrum of Irgacure 784, recorded in toluene, are presented in Figure 3.

From Figure 3, the LED light source emits in a relatively narrow range (490–590 nm), which can be assigned to the green region of visible light. The peak of emission was found to be at 531 nm, while the full width of the half maximum is 32 nm. Irgacure 784 has high absorption below 500 nm, which drops rapidly above this wavelength and is practically transparent above 550 nm. However, the molar extinction coefficient is still approximately $\epsilon 90 \text{ M}^{-1} \text{ cm}^{-1}$ at the emission maximum of the light source; therefore, we concluded that Irgacure 784 can be effectively used in combination with a green LED light source.

3.2. Kinetic Investigation of the Photopolymerization. To gain insight into the photopolymerization process of our dental resin, kinetic measurements were performed. However, the chain polymerization of acrylate monomers during photopolymerization may involve very complex reactions; therefore, it is only possible to work with simplified models. The reaction rate ($d\alpha/dt$) of a theoretical radical chain polymerization is usually given by

$$\frac{d\alpha}{dt} = k_p \left(\frac{QI_a}{k_t} \right)^{1/2} (1 - \alpha), \quad (1)$$

where α is the degree of conversion, I_a is the intensity of absorbed light in moles of light quanta per liter-second, Q is the quantum yield of initiation, and k_p and k_t are the rate constants for propagation and termination, respectively.

Equation (1) is only valid if we assume steady-state conditions. However, during propagation, the reaction kinetics are affected by autoacceleration, which is a consequence of altered diffusion. Since (1) is no longer applicable, the rate of reaction must be rewritten as a function of the radical concentration, $[R]$:

$$\frac{d\alpha}{dt} = k_p (1 - \alpha) [R], \quad (2)$$

where $[r] = \sum_{i=0}^n [RM_i]$.

Unfortunately, (2) does not consider that the glass transition temperature (T_g) of the restorative material must be higher than the maximum temperature that can be reached in the oral cavity, in order to prevent failures of the restorations due to thermal fatigue. As the photocuring progresses, T_g of the network formed also increases, and the initially viscous liquid monomer mixture becomes a glassy solid. In this glassy network, the mobility of the monomers and radicals is greatly reduced, and due to this vitrification effect the reaction becomes diffusion controlled and the termination step of the polymerization is governed by the strong decrease in the molecular mobility. Maffezzoli and Terzi [26] proposed a simple expression, capable of describing the overall kinetic process by modelling the kinetic behavior of acrylates during photocuring conditions, using a simple pseudo-autocatalytic expression. According to Maffezzoli, (2) can be transformed to include the two effects of diffusion, autoacceleration and vitrification, as presented in

$$\frac{d\alpha}{dt} = k_{app} \alpha^m (\alpha_{\infty} - \alpha)^n (1 - \alpha), \quad (3)$$

where $k_{app} = k_{app,o} \sqrt{I_o}$ is the apparent rate constant of the polymerization, I_o is the initial light intensity, m and n are the fitting parameters, and α_{∞} represents the maximum degree of conversion. Notably, according to (3), the reaction rate converges to zero as the degree of conversion (α) approaches α_{∞} .

Raman spectroscopy is an appropriate technique to determine the degree of conversion (α) [27] for (3). Measurements were obtained before and after 150 s of irradiation, and the results are presented in the spectral range of 500–2000 cm^{-1} in Figure 4.

The vinyl double bonds (C=C) and aromatic ring quadrat stretching vibration (Ph), which were used to calculate the conversion [27, 28], are observed at 1639 and 1610 cm^{-1} , respectively, as indicated by the arrows. The highest intensity of the band, at 1639 cm^{-1} , was observed for the samples before irradiation. The monomer has the largest number of C=C bonds before polymerization. The intensity of the C=C band decreased upon irradiation due to the consumption of the double bonds in the polymerization reaction, whereas the intensity of the Ph band remained constant during the irradiation. The conversion (α) was calculated using the two-frequency technique, as a ratio between aliphatic C=C, at

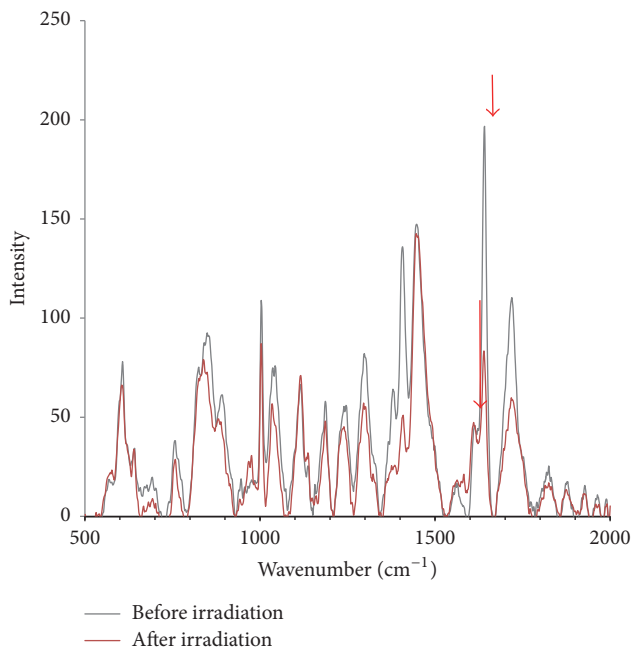


FIGURE 4: Representative Raman spectrum before and after irradiation with a LED light source.

1637 cm^{-1} — $I_{C=C}$, and aromatic, at 1610 cm^{-1} — I_{Ph} , carbon double bonds peaks based on

$$\alpha = \left[1 - \frac{(I_{C=C}/I_{Ph})_{\text{polymer}}}{(I_{C=C}/I_{Ph})_{\text{monomer}}} \right] \times 100\%. \quad (4)$$

Conversion data were calculated based on (4) from the Raman spectra recorded every second for 250 s in total, at light intensities between 0.7 and 10.0 mW/cm^2 . The measured reaction rates along with the calculated ones, per (3), were plotted as a function of the light intensity as shown in Figure 5.

From Figure 5, the experimental points can be well fitted using (3). The x variable has a power of 0.52 , which agrees with the square root dependency ($I_o^{1/2}$) of the reaction rate upon the light intensity. The applicability of the model, describing the overall kinetic behavior, was tested by comparing the theoretical conversion data with the experimental data. According to Figure 6, the conversion of photocuring shows a significant light intensity dependence.

Using a low value of 1.4 mW/cm^2 , only 50% conversion was obtained, taking more than 200 s to reach the final value. However, little difference was observed for I_o of 6 and 10 mW/cm^2 , where a conversion of more than 70% was achieved after 150 s . For dental applications, higher light intensities are favorable; however these values fall well below those previously reported for CQ [16].

3.3. Resin Density, Water Swelling Experiments, and Physical Properties of the Cured Resins. An increase in density is a good indicator of resin formation because the crosslinked 3D structure is more compact than the mixture of the unreacted monomers, as with acrylate polymerization. The density of

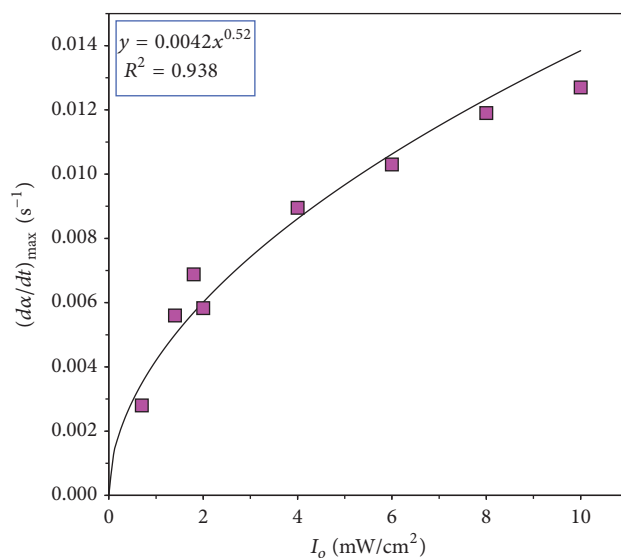


FIGURE 5: The reaction rates ($d\alpha/dt$) as a function of light intensity (I_o). The solid line represents the fitted curve based on (3).

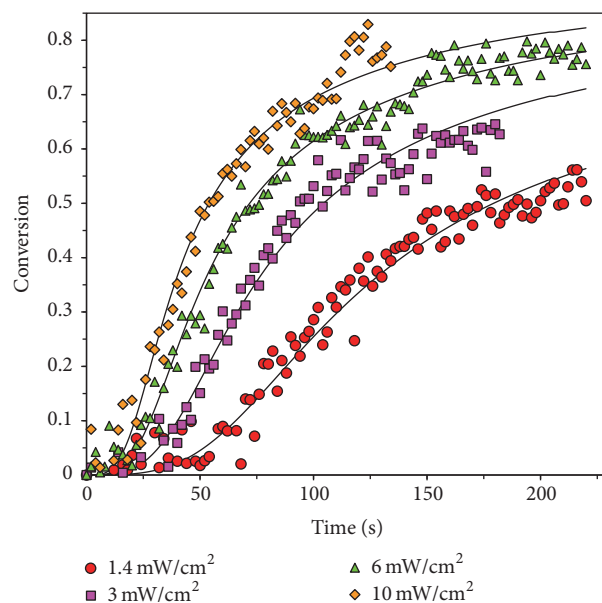


FIGURE 6: Comparison between the degree of conversion measured by Raman spectroscopy and that of calculated based on (3) at different light intensities.

the monomer mixture and that of the cured samples were measured in a pycnometer, relative to water. The density increased from $1.121 \pm 0.001\text{ g/cm}^3$ in the monomer mixture to 1.16 to 1.18 g/cm^3 (the error was less than 2.5% in each case), as seen in Figure 7.

The resin densities did not show any significant variation, indicating similar structural properties and conversion of the monomers. For practical applicability, swelling experiments were performed in deionized water for seven days at ambient temperature. The samples did not uptake water, with a mass increase of about 1% in each case, which is favorable for

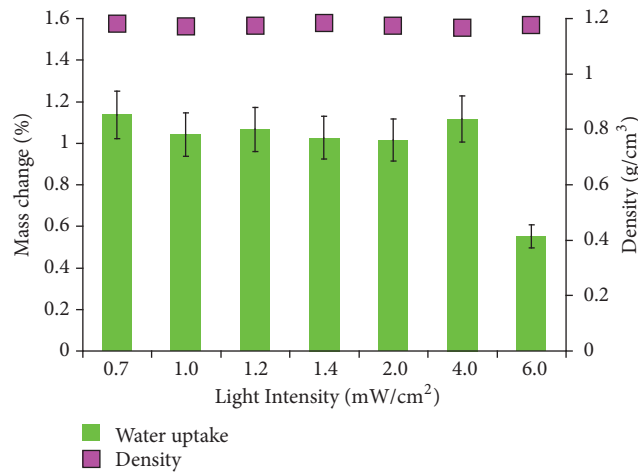


FIGURE 7: Densities and water uptake of the photocured resins irradiated at different intensities after an irradiation time of 30 seconds.

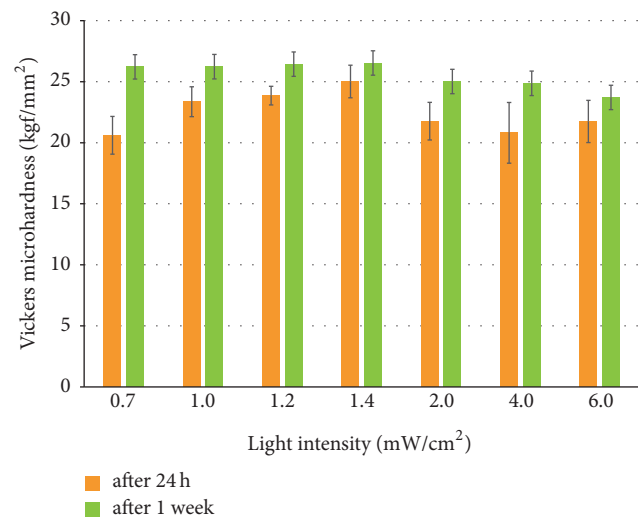


FIGURE 8: Vickers microhardness values for the samples cured by a LED light source at different intensities, with an irradiation time of 30 seconds, after storage for 24 hours and one week.

in vivo applications. The cured samples were extracted in DMF to determine the conversion of the monomers. In each case, the weight loss was approximately 9-10%, indicating a conversion close to 90%, even with a light intensity as low as 1 mW/cm². This result shows that Irgacure 784 can be considered effective when combined with the narrow-emission green LED.

Another important factor to consider for practical applications is the surface hardness of the material. Therefore, the Vickers microhardness of the resins was measured after 24 h and after one week. The results are presented in Figure 8. It is important to measure the hardness of the samples at two different times to account for the effect of postcuring. That is, while most of the polymerization reaction occurs during the first minutes after irradiation, a significant portion of reaction may take place after curing [29].

Based on Figure 8, the Vickers hardness versus light intensity does not show any significant variation. Good hardness data were measured even near a light intensity of 1 mW/cm². Notably, the increase in hardness after one-week storage is not significant, indicating high conversion at each intensity, which aligns well with the extraction results. Unfortunately, above an irradiation intensity of 6 mW/cm², the surface properties of the samples rapidly deteriorated and became gel-like, making the hardness measurements unreliable. This phenomenon may be accounted for by the large amount of Irgacure 784 photoinitiator (2% m/m) in the system. Although in the literature 2% (m/m) values can be found for both CQ and Irgacure 784 [30, 31], the latter is much more effective. Therefore, for further experiments, a 1.4 mW/cm² power density was used for the LED light source. At first glance, the maximum Vickers hardness of this resin, 20–25 kgf/mm², falls below that of the sound dentin, at 40 to 60 kgf/mm². However, the physical properties of dental filling materials differ in many aspects, such as type and amount of filler, type and amount of initiators, and salinization of the filler particles. These effects may be more determinative than the nature of the copolymer matrix. In this study, we only focused on the properties of the pure resin.

Hardness is not the only property affecting the practical applicability of dental restorative materials. Mechanical properties are a function of the degree of conversion and the 3D structure of the polymer network. As shown by Asmussen and Peutzfeldt [24], the diametral tensile strength, flexural strength, and modulus of the elasticity are also influenced by monomer composition. During sample preparation, we used the optimal composition [24] of BisGMA : TEGDMA : UDMA in a weight ratio of 21.4 : 25.4 : 53.3 and only one light intensity setting at 1.4 mW/cm², where the Vickers hardness value was found to be near the maximum. The measured mechanical properties are shown in Table 1. In addition, hypothesis tests, including independent sample *t*-tests and the nonparametric Mann–Whitney tests, were run.

Commercial dental composite restoratives have a flexural strength in the range of 60 to 180 MPa [32, 33]. Our data falls within this range and is in good agreement with our previously reported values obtained for BisGMA-based resins, using CQ as initiator [34]. The *E*-modulus of about 0.9 GPa was found to be a bit lower than that previously reported for similar compositions [24, 35]. However, this is the pure resin and for practical applications the *E*-modulus can be significantly enhanced by the addition of filler materials [35]. Compressive strength has a particularly important role in the mastication process, since most of the masticatory forces are of compressive nature. The compressive strength values of our copolymer matrix are, at around 300 Mpa, in the order of those published by Galvão et al. [36]. The high diametral tensile strength values may be attributed to the high degree of conversion of the methacrylate double bonds [37]. However, the diametral tensile test is only suitable for truly brittle materials. Materials that plastically deform would produce erroneous DTS values [38]. Without filler, our matrix may not be truly better and this could explain the high standard deviation values obtained during this measurement, whereas

TABLE 1: Mechanical properties of the photocured resins at 1.4 mW/cm² light intensity, with an irradiation time of 30 seconds. The sample size is denoted by n . We used IBM SPSS Statistics Version 22 for all statistical calculations.

	E -modulus (MPa)	Flexural strength (MPa)	Compressive strength (MPa)	Diametric tensile strength (MPa)
Number of samples	10	10	15	8
Mean value	876.4	61.7	348.8	46.1
Minimum value	771.7	55.5	316.7	33.1
Maximum value	979.6	70.7	376	64.4
Std. deviation	63.0	4.4	16.1	11.0

the other mechanical measurements resulted in errors less than 10%.

4. Discussion

The applicability of a narrow-emission green LED light source, in combination with Irgacure 784 during the photocuring of an acrylate-based dental resin, was studied. The resin contained a monomer mixture of BisGMA, TEGDMA, and UDMA in a previously reported 21.4 : 25.4 : 53.3 weight ratio for the best mechanical properties, and 2% m/m Irgacure 784 was used. Our LED light source emits in a relatively narrow range of 490 to 590 nm, with a peak emission at 531 nm. In this range, Irgacure 784 still has a molar extinction coefficient of approximately $\epsilon 90 \text{ M}^{-1} \text{ cm}^{-1}$ making it effective in combination with the green LED light source. The photopolymerization was performed at different light intensities ranging from 0.8 to 10 mW/cm² and was followed by Raman spectroscopy in a polystyrene cuvette. The conversion (α) was calculated using the two-frequency technique, as a ratio between aliphatic C=C and aromatic carbon double bond peaks. To handle the complex processes of photocuring for kinetic investigations, we used a modified version of Maffezzoli's equation, which is capable of describing the overall kinetic process by modelling the kinetic behavior of acrylates during photocuring conditions, using a simple pseudo-autocatalytic expression. By including autoacceleration and vitrification in the expression, we obtained very good agreement between the experimental and calculated kinetic values. The maximum conversion values were found to be about 70–80% after 150 s irradiation time at light intensities of 6–10 mW/cm².

For physical and mechanical investigations, specimen disks with dimensions of 2 mm by 10 mm were prepared using the same light intensities as used in the kinetic investigations. The density of the cured resins was found to increase compared to that of the monomers and was found to be nearly constant ($\rho \sim 1.17\text{--}1.19 \text{ g/cm}^3$) with light intensity. Extraction with DMF revealed a weight loss of less than 10% for each sample, indicating approximately 90% conversion for these thin disks even at a light intensity of about 1 mW/cm². The cured resins did not swell in water, took up less than 1% water in a week, and therefore may be suitable for dental applications.

Good Vickers microhardness values of 20–25 kgf/mm² were obtained, even at low light intensities. This intensity

value is more than one magnitude lower than those used in dental practice. However, at light intensities over 6 mW/cm², the hardness values deteriorated rapidly potentially due to the high concentration of Irgacure 784 and the thin disk samples. The compressive strength and diametric tensile strength of the resins, cured at 1.4 mW/cm² light intensity, were in the range of 300 MPa and 30 MPa, in good agreement with those of practically applied dental restorative composites. The flexural strength was found to be about 60 MPa and the E -modulus was approximately 0.9 GPa.

Conflicts of Interest

The authors declare no conflicts of interest.

Acknowledgments

This work was financially supported by NFKI (National Research, Development and Innovation Office, Hungary) (Grant K-116465), GINOP-2.3.2.-15-2016-00011, GINOP-2.3.2.-15-2016-00022, and GINOP-2.3.2.-15-2016-00041. The work/publication is supported by the EFOP-3.6.1-16-2016-00022 project. The project is cofinanced by the European Union and the European Social Fund. Furthermore, this paper was also supported by the János Bolyai Research Scholarship of the Hungarian Academy of Sciences (Miklós Nagy).

References

- [1] M. Tehfe, F. Louradour, J. Lalevée, and J. Fouassier, "Photopolymerization Reactions: On the Way to a Green and Sustainable Chemistry," *Applied Sciences*, vol. 3, no. 2, pp. 490–514, 2013.
- [2] B. C. Gross, J. L. Erkal, S. Y. Lockwood, C. Chen, and D. M. Spence, "Evaluation of 3D printing and its potential impact on biotechnology and the chemical sciences," *Analytical Chemistry*, vol. 86, no. 7, pp. 3240–3253, 2014.
- [3] M. C. Gather, A. Köhnen, A. Falcou, H. Becker, and K. Meerholz, "Solution-processed full-color polymer organic light-emitting diode displays fabricated by direct photolithography," *Advanced Functional Materials*, vol. 17, no. 2, pp. 191–200, 2007.
- [4] E. Suhir, Y. C. Lee, and C. P. Wong, *Micro- and Opto-Electronic Materials and Structures: Physics, Mechanics, Design, Reliability, Packaging*, Springer US, New York, NY, USA, 2007.
- [5] T. J. Trout, J. J. Schmieg, W. J. Gambogi, and A. M. Weber, "Optical photopolymers: Design and applications," *Advanced Materials*, vol. 10, no. 15, pp. 1219–1224, 1998.

- [6] H. Bian, J. Yang, N. Zhang, Q. Wang, Y. Liang, and D. Dong, "Ultrathin free-standing polymer membranes with chemically responsive luminescence via consecutive photopolymerizations," *Polymer Chemistry*, vol. 7, no. 5, pp. 1191–1196, 2016.
- [7] S. Baudis, F. Nehl, S. C. Ligon et al., "Elastomeric degradable biomaterials by photopolymerization-based CAD-CAM for vascular tissue engineering," *Biomedical Materials*, vol. 6, no. 5, Article ID 055003, 2011.
- [8] P. Bruno, G. Malucelli, B. Tylkowski, J. Ferré, and M. Giamberini, "Acrylic microspheres as drug-delivery systems: Synthesis through in situ microemulsion photoinduced polymerization and characterization," *Polymer International*, vol. 62, no. 2, pp. 304–309, 2013.
- [9] F. H. Coelho-de-Souza, D. S. Gonçalves, M. P. Sales et al., "Direct anterior composite veneers in vital and non-vital teeth: A retrospective clinical evaluation," *Journal of Dentistry*, vol. 43, no. 11, pp. 1330–1336, 2015.
- [10] U. Erdemir, H. S. Sancakli, B. C. Yaman, S. Ozel, T. Yucel, and E. Yildiz, "Clinical comparison of a flowable composite and fissure sealant: A 24-month split-mouth, randomized, and controlled study," *Journal of Dentistry*, vol. 42, no. 2, pp. 149–157, 2014.
- [11] K. L. Van Landuyt, J. Snauwaert, J. De Munck et al., "Systematic review of the chemical composition of contemporary dental adhesives," *Biomaterials*, vol. 28, no. 26, pp. 3757–3785, 2007.
- [12] Z. C. Li and S. N. White, "Mechanical properties of dental luting cements," *The Journal of Prosthetic Dentistry*, vol. 81, no. 5, pp. 597–609, 1999.
- [13] R. B. Price, J. L. Ferracane, and A. C. Shortall, "Light-Curing Units," *Journal of Dental Research*, vol. 94, no. 9, pp. 1179–1186, 2015.
- [14] W. D. Cook, "Photopolymerization kinetics of dimethacrylates using the camphorquinone/amine initiator system," *Polymer Journal*, vol. 33, no. 3, pp. 600–609, 1992.
- [15] Z. Kucybała, M. Pietrzak, J. Paczkowski, L.-Å. Lindén, and J. F. Rabek, "Kinetic studies of a new photoinitiator hybrid system based on camphorquinone-N-phenylglycine derivatives for laser polymerization of dental restorative and stereolithographic (3D) formulations," *Polymer Journal*, vol. 37, no. 20, pp. 4585–4591, 1996.
- [16] E. A. Kamoun and H. Menzel, "Crosslinking behavior of dextran modified with Hydroxyethyl methacrylate upon irradiation with visible light-effect of concentration, coinitiator type, and solvent," *Journal of Applied Polymer Science*, vol. 117, no. 6, pp. 3128–3138, 2010.
- [17] D. Zhou and Y. Ito, "Visible light-curable polymers for biomedical applications," *SCIENCE CHINA Chemistry*, vol. 57, no. 4, pp. 510–521, 2014.
- [18] C. Decker, "Photoinitiated crosslinking polymerisation," *Progress in Polymer Science*, vol. 21, no. 4, pp. 593–650, 1996.
- [19] H. Kitano, K. Ramachandran, N. B. Bowden, and A. B. Scranton, "Unexpected visible-light-induced free radical photopolymerization at low light intensity and high viscosity using a titanocene photoinitiator," *Journal of Applied Polymer Science*, vol. 128, no. 1, pp. 611–618, 2013.
- [20] D.-H. Shin and H. R. Rawls, "Degree of conversion and color stability of the light curing resin with new photoinitiator systems," *Dental Materials*, vol. 25, no. 8, pp. 1030–1038, 2009.
- [21] K. D. Jandt and R. W. Mills, "A brief history of LED photopolymerization," *Dental Materials*, vol. 29, no. 6, pp. 605–617, 2013.
- [22] W. J. Dunn and A. C. Bush, "A comparison of polymerization by light-emitting diode and halogen-based light-curing units," *The Journal of the American Dental Association*, vol. 133, no. 3, pp. 335–341, 2002.
- [23] M. A. Gauthier, I. Stangel, T. H. Ellis, and X. X. Zhu, "Oxygen inhibition in dental resins," *Journal of Dental Research*, vol. 84, no. 8, pp. 725–729, 2005.
- [24] E. Asmussen and A. Peutzfeldt, "Influence of UEDMA, BisGMA and TEGDMA on selected mechanical properties of experimental resin composites," *Dental Materials*, vol. 14, no. 1, pp. 51–56, 1998.
- [25] D. Sabol, M. R. Gleeson, S. Liu, and J. T. Sheridan, "Photoinitiation study of Irgacure 784 in an epoxy resin photopolymer," *Journal of Applied Physics*, vol. 107, no. 5, Article ID 053113, 2010.
- [26] A. Maffezzoli and R. Terzi, "Effect of irradiation intensity on the isothermal photopolymerization kinetics of acrylic resins for stereolithography," *Thermochimica Acta*, vol. 321, no. 1–2, pp. 111–121, 1998.
- [27] M. A. Gauthier, I. Stangel, T. H. Ellis, and X. X. Zhu, "A new method for quantifying the intensity of the C=C band of dimethacrylate dental monomers in their FTIR and Raman spectra," *Biomaterials*, vol. 26, no. 33, pp. 6440–6448, 2005.
- [28] Z. Okulus, T. Buchwald, M. Szybowicz, and A. Voelkel, "Study of a new resin-based composites containing hydroxyapatite filler using Raman and infrared spectroscopy," *Materials Chemistry and Physics*, vol. 145, no. 3, pp. 304–312, 2014.
- [29] M. Par, O. Gamulin, D. Marovic, E. Klaric, and Z. Tarle, "Effect of temperature on post-cure polymerization of bulk-fill composites," *Journal of Dentistry*, vol. 42, no. 10, pp. 1255–1260, 2014.
- [30] T. Guimarães, L. F. Schneider, R. R. Braga, and C. S. Pfeifer, "Mapping camphorquinone consumption, conversion and mechanical properties in methacrylates with systematically varied CQ/amine compositions," *Dental Materials*, vol. 30, no. 11, pp. 1274–1279, 2014.
- [31] Y. M. Chang, S. C. Yoon, and M. Han, "Photopolymerization of aromatic acrylate containing phosphine oxide backbone and its application to holographic recording," *Optical Materials*, vol. 30, no. 4, pp. 662–668, 2007.
- [32] S. M. Chung, A. U. J. Yap, S. P. Chandra, and C. T. Lim, "Flexural strength of dental composite restoratives: Comparison of biaxial and three-point bending test," *Journal of Biomedical Materials Research Part B: Applied Biomaterials*, vol. 71, no. 2, pp. 278–283, 2004.
- [33] S. Dos Santos, M. R. Moysés, C. E. P. Alcântara, J. C. R. Ribeiro, and J. G. R. Ribeiro, "Flexural strength of a composite resin light cured with different exposure modes and immersed in ethanol or distilled water media," *Journal of Conservative Dentistry*, vol. 15, no. 4, pp. 333–336, 2012.
- [34] M. Szaloki, J. Gall, K. Bukovinszki, J. Borbely, and C. Hegedus, "Synthesis and characterization of cross-linked polymeric nanoparticles and their composites for reinforcement of photocurable dental resin," *Reactive and Functional Polymers*, vol. 73, no. 3, pp. 465–473, 2013.
- [35] H. Zhang and B. W. Darvell, "Mechanical properties of hydroxyapatite whisker-reinforced bis-GMA-based resin composites," *Dental Materials*, vol. 28, no. 8, pp. 824–830, 2012.
- [36] M. R. Galvão, S. G. F. R. Caldas, S. Calabrez-Filho et al., "Compressive strength of dental composites photo-activated with different light tips," *Laser Physics*, vol. 23, no. 4, Article ID 045604, 2013.

- [37] E. ASMUSSEN and K. D. JORGENSEN, "Fatigue strength of some resinous materials," *European Journal of Oral Sciences*, vol. 90, no. 1, pp. 76–79, 1982.
- [38] R. W. Penn, R. G. Craig, and J. A. Tesk, "Diametral tensile strength and dental composites," *Dental Materials*, vol. 3, no. 1, pp. 46–48, 1987.

Research Article

Effect of Oxygen Flow Rate on the Optical, Electrical, and Mechanical Properties of DC Sputtering ITO Thin Films

Chuen-Lin Tien ^{1,2}, Hong-Yi Lin,² Chih-Kai Chang,² and Chien-Jen Tang³

¹Department of Electrical Engineering, Feng Chia University, Taichung 40724, Taiwan

²Ph. D. Program of Electrical and Communications Engineering, Feng Chia University, Taichung 40724, Taiwan

³Department of Photonics, Feng Chia University, Taichung 40724, Taiwan

Correspondence should be addressed to Chuen-Lin Tien; cltien@fcu.edu.tw

Received 17 November 2017; Accepted 9 January 2018; Published 7 February 2018

Academic Editor: Shuan-Yu Huang

Copyright © 2018 Chuen-Lin Tien et al. This is an open access article distributed under the Creative Commons Attribution License, which permits unrestricted use, distribution, and reproduction in any medium, provided the original work is properly cited.

This study presents the effect of oxygen flow rate on the optical, electrical, and mechanical properties of indium tin oxide (ITO) thin films prepared by the DC magnetron sputtering technique. The oxygen flow rate was varied from 10 to 50 sccm. The ITO thin films deposition under different oxygen flow rates exhibits different properties. We used an optical spectrometer to measure the optical transmittance and a four-point probe instrument to determine the resistivity. A home-made Twyman-Green interferometer was used to evaluate residual stress and a microscopic interferometer was used to measure the surface roughness of ITO thin films. The experimental results show that the average optical transmittance is larger than 85% in visible range; the electrical resistivity has a minimum 6.85×10^{-4} ohm-cm for the oxygen flow of 10 sccm. The residual stress is varied from -0.15 GPa to -0.34 GPa in the range of 10–50 sccm. The root-mean-square (rms) surface roughness is changed from 2.64 nm to 2.74 nm as the oxygen flow rate increases. The results show that the oxygen flow rate has significant influence on the electrical resistivity, residual stress, and surface roughness of the ITO thin film.

1. Introduction

The transparent conductive oxide films (TCO) had excellent physical and chemical properties, and the coating process parameters have significant influence on the optical, electrical, and structural properties and residual stress of the transparent conductive oxide films. Indium tin oxide (ITO) thin film is one kind of transparent conductive films. Due to its high transmittance and good physical and chemical properties [1, 2], it is widely used in optical devices like flat panel displays, solar cells, sensors, and so on [3–5]. There are many different methods for the fabrication of ITO thin films including the magnetron sputtering method [6, 7], thermal evaporation method [8], plasma ion-assisted evaporation [9], reactive electron-beam evaporation [10], and sol-gel method [11]. It is well known that almost all thin films, produced by the various deposition techniques, have residual stresses. Residual stress that develops during thin film growth is critical issue for many applications. Films stress causes many undesirable phenomena, for example, the cracking or

peeling of the film and the bending of the substrate. The precise measurement of residual stress in thin films is helpful to understand the stress behaviour and related effects. DC magnetron sputter deposition has generally been used in industrial production lines for the deposition of ITO films because this method yields homogeneous ITO films with low resistivity and good reproducibility. Therefore, in order to improve the quality of the ITO thin films, the surface characteristics, residual stresses, and optical and electrical properties of DC magnetron sputtering ITO thin films have been investigated experimentally.

There are many papers to explore the optical, electrical, and structural properties of ITO thin films prepared by different deposition methods. However, there are few studies to report the effect of oxygen flow rate on the residual stress and surface roughness of sputtering ITO thin films [12–14]. This study investigated the effect of oxygen flow rate on optical, mechanical, and electrical properties and the surface roughness of ITO thin films prepared by DC magnetron sputtering technique. The optical transmittance spectra of ITO films

were scanned by a UV-Visible spectrometer. The resistivity of these films was measured by a four-point probe instrument. The residual stress was evaluated by a home-made Twyman-Green interferometer. The surface roughness was determined by a Linnik microscopic interferometer.

2. Experimental Methods

2.1. DC Magnetron Sputtering. ITO thin films were deposited using DC magnetron reactive sputtering. The vacuum system consisted of a turbo molecular pump backed by a mechanical pump. A three-inch disk of In-10 wt% Sn alloy was used as a sputtering target. The spacing of the target to substrates was 80 mm. Before sputtering, the target was presputtered for about 10 min with a shutter covering the target in order to remove the adsorbed gas on the surface of the ITO target. The working gas consisted of a mixed gas of Ar and O₂, the flow rates of which were independently controlled by mass flow controllers. A DC discharge was sustained by a power supply operated under the constant-current mode with 150 mA. The constant-current mode can reduce spikes and arcing; thus plasma conditions are more stable in coating process. The base pressure of the system was 2.7×10^{-4} Pa. To minimize the oxidation of the target, Ar and O₂ were introduced near the target and the substrate, respectively. The flow rates of oxygen reactive gas were varied from 10 to 50 sccm. Both BK7 glass and silicon wafer were employed as coating substrates, where the former was used for measuring the transmittance and residual stress of ITO thin films and the latter for measuring the other properties. The coating substrates were not heated and were assumed to be at near room temperature during the film deposition.

2.2. Optical Properties. Analysis of the optical properties of deposited films was carried out. The relative transmittance spectra of ITO thin films deposited at different oxygen flow rates were measured. In this work, the UV-Visible spectrometer (Chrom Tech., CT-2200) was used to measure the transmission spectrum from 350 nm to 850 nm. The envelope method was used to determine three optical constants, namely, the refractive index (n), extinction coefficient (k), and physical thickness (d). These were determined from the transmittance spectrum with loss absorption [15].

2.3. Residual Stress Measurements. Stress in thin films is primarily composed of a thermal stress and an intrinsic stress [16]. The thermal stress is due to the difference in the thermal expansion coefficients between the coating and substrate materials. The intrinsic stress is induced during the deposition process, but the mechanisms are complex and not yet fully understood. To study thin film stress issues, it is necessary to understand the stress mechanisms and their effects. Therefore, the precise measurement of stress in thin films is of considerable importance in numerous industrial applications.

We used a home-made Twyman-Green interferometer associated with the fast Fourier transform (FFT) method to measure the radius of curvature of substrate before and after

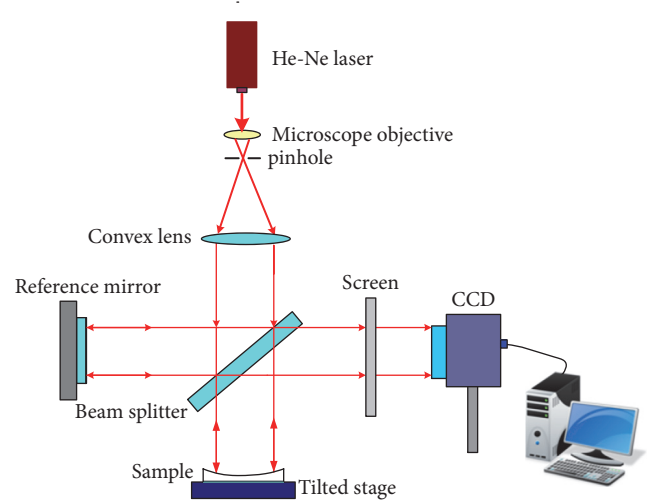


FIGURE 1: Stress measuring instrument based on Twyman-Green interferometer.

thin film deposition [17, 18]. The substrate was a circular BK7 glass with a diameter of 25.4 mm and thickness $t_s = 1.5$ mm. The schematic diagram of the stress measuring apparatus is shown in Figure 1. The laser beam passed through a spatial filter and then through a lens to form a plane wave front. The plane wave front was divided into different amplitudes by a beam splitter. The reflected beam and the transmitted beam traveled to a reference plate and a tested sample. The two beams were recombined and traveled toward a CCD camera after being reflected by both the reference plate and the tested sample. A digital CCD camera was used to record the interference fringe and the stress in the thin films was measured by the fast Fourier transform (FFT) method [18]. A thin film's surface deformation can be readily obtained by subtraction of the surface contours before and after film deposition. The residual stress of the thin films can be determined by the modified Stoney equation [19]:

$$\sigma = \frac{1}{6} \frac{E_s}{1 - \nu_s} \frac{t_s^2}{t_f} \left(\frac{1}{R} - \frac{1}{R_0} \right), \quad (1)$$

where σ is residual stress of the films; E_s is Young's modulus ($E_s = 81$ GPa) of the BK7 substrate; ν_s is Poisson's ratio ($\nu_s = 0.208$) of the BK7 substrate; R_0 is the radius of curvature of the BK7 substrate before coating; R is the radius of curvature of the BK7 substrate after coating; t_s is the thickness of the BK7 substrate; t_f is the thickness of the films. By convention, σ is negative for compressive stress and positive for tensile stress. Tensile stress is present in the film if the curvature of the substrate is concave; conversely, the stress is compressive if the curvature of the substrate is convex.

2.4. Surface Roughness Measurements. The surface morphology and microstructure of the thin films depended on the properties of the films and fabrication parameters. There are many ways to measure the roughness of the films. We usually use root-mean-square (rms) roughness to evaluate the surface roughness of the thin films. We used a home-made

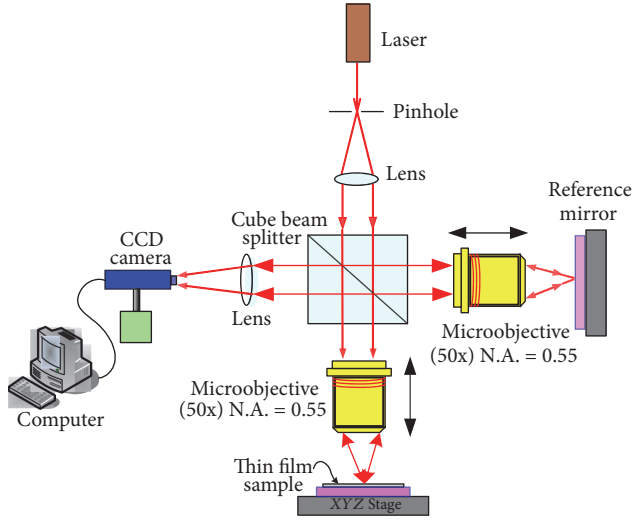


FIGURE 2: Measurement of surface roughness by using Linnik microscopic interferometer.

Linnik microscopic interferometer to evaluate the surface roughness of thin films [20]. The Linnik microscopic interferometer was combined with the fast Fourier transform method to build up a surface roughness measurement system, as shown in Figure 2. The interference patterns were captured by a CCD camera. The fast Fourier transform (FFT) technique was used for the phase extraction. A phase unwrapping algorithm is needed to remove the discontinuities by adding or subtracting multiples of 2π to a pixel until the difference between it and its adjacent pixel is less than π . A Gaussian filter is used to separate the roughness profile from the original profile. The mean surface profile is then subtracted from the surface height profile to obtain the roughness profile. The root-mean-square value of surface roughness is determined by the numerical analysis with MATLAB program.

3. Results and Discussion

The optical transmittance of the films was measured by a UV-Visible spectrophotometer in the wavelength range 350–750 nm. Figure 3 shows transmittance spectra of the ITO thin films deposited under different oxygen flow rates. The transmittance of the ITO thin films is not a function of the oxygen flow rate, but all samples are over 85% in the visible region. At oxygen flow rate of 30 sccm, the transmittance of the ITO thin films has a maximum value of 88.7% for the wavelength of 500 nm. The spectra of the ITO films were obtained by scanning from 350 nm to 850 nm. The thickness of ITO films in various conditions was determined by transmittance spectrum. The average refractive index (n) and the extinction coefficient (k) in visible range vary in range of 2.01–2.04 and 5.6×10^{-3} – 6.5×10^{-3} , respectively. However, no obvious correlation between n and k is observed. Figure 4 shows the ITO film thickness as a function of the oxygen flow rate.

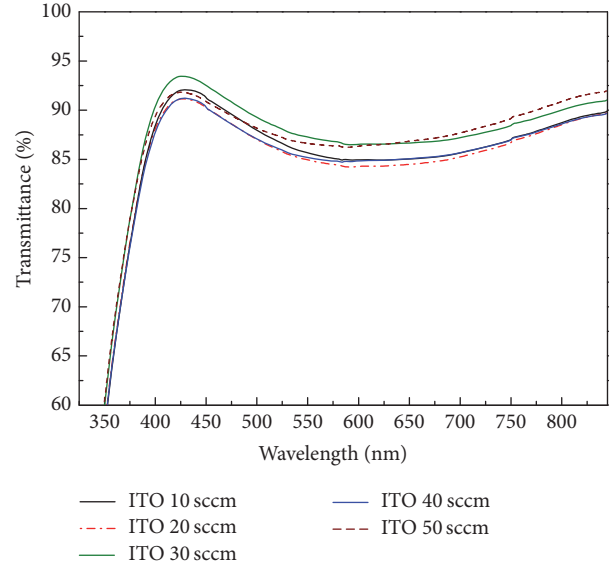


FIGURE 3: Transmittance spectra of ITO thin films deposited under different oxygen flow rates.

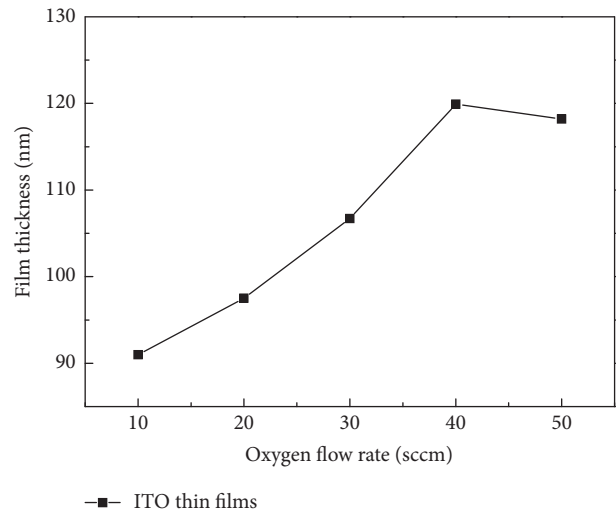


FIGURE 4: Film thickness as a function of oxygen flow rate.

In this study, a sheet resistance meter with four-point probe was used to measure the sheet resistance and resistivity of thin films. Figure 5 shows the resistivity and sheet resistance as a function of the oxygen flow rate. The resistivity and sheet resistance increase with increasing the oxygen flow rate from 10 to 30 sccm, and then both decrease as the oxygen flow rate is larger than 30 sccm. In the film deposition experiments, the oxygen flow rate was 10 sccm and the working pressure was maintained at 6.7×10^{-4} Pa; ITO thin films exhibit a lower resistivity and sheet resistance. A maximum resistivity of $1.56 \times 10^{-3} \Omega\text{-cm}$ is found at the oxygen flow rate of 30 sccm. The lowest resistivity of $6.85 \times 10^{-4} \Omega\text{-cm}$ and a minimum sheet resistance of $75.8 \Omega/\text{sq.}$ were achieved at the oxygen flow rate of 10 sccm. This low resistivity and sheet resistance may be attributed to a formation of SnO_2

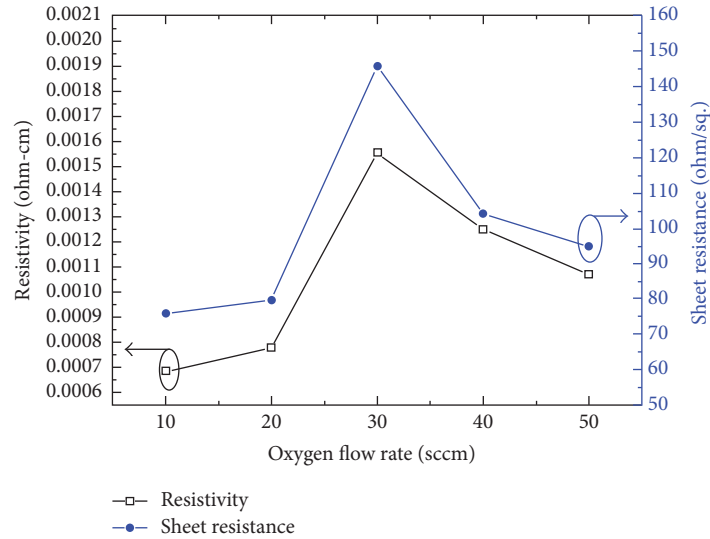


FIGURE 5: Resistivity and sheet resistance of ITO thin films deposited under different oxygen flow rates.

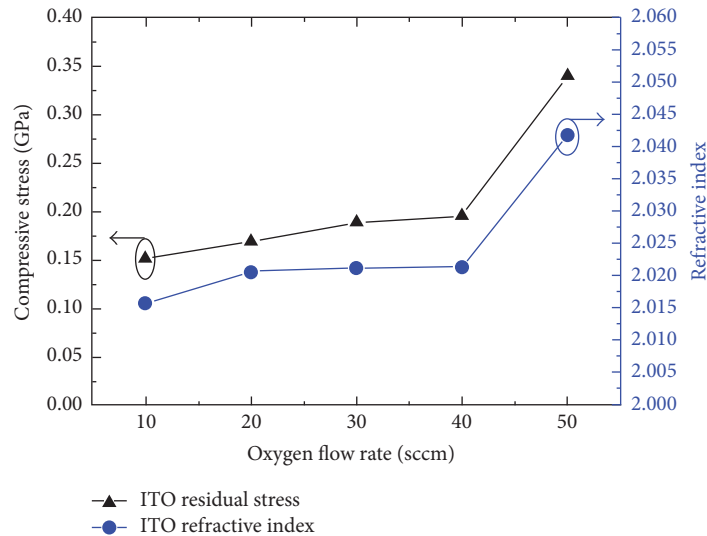


FIGURE 6: Residual stress and refractive index of ITO thin films as a function of oxygen flow rate.

in the films resulting in high carrier mobility. The electrical resistivity of the ITO films is considered to be sensitive to the oxygen flow rate in the mixture of the discharge gas (argon) and reactive gas (oxygen). At oxygen flow rates from 10 to 30 sccm, the increase in resistivity and sheet resistance was due to gradual decrease of the carrier mobility. The mobility was slightly enhanced with increasing oxygen flow rates from 30 to 50 sccm. It is well known for the ITO films that the electrons are released from the substitutional entered Sn atoms in the sublattice and from the doubly charged oxygen vacancies. Tin can exist as either SnO or SnO₂. The presence of SnO₂ would result in *n* doping of the lattice because the dopant would add electrons to the conduction band [21]. Furthermore, many studies have reported that the resistivity of ITO thin films is strongly dependent on the oxidation state during film deposition [22–25]. As pointed out above, the

charge carriers of the ITO thin films are either contributed by Sn⁺⁴ ion or oxygen vacancies. The incorporation of oxygen atoms into the ITO films causes the decrease of oxygen vacancies and then gives rise to higher resistivity of ITO films [26]. When the oxygen vacancies in ITO thin films are fully filled, it leads to thin films growing more dense. This cannot only decrease the defects, but slightly improve the mobility in ITO films [27].

Film stress is an important factor in the adhesion and stability of thin films. Figure 6 shows the residual compressive stress and refractive index as a function of the oxygen flow rate. Both values increase as the oxygen flow rate increases. The residual stress in all ITO thin films is a compressive stress with values ranging from -0.15 GPa to -0.34 GPa. In this work, the plasma bombardment energy increases as oxygen flow rate increases during thin film deposition; the

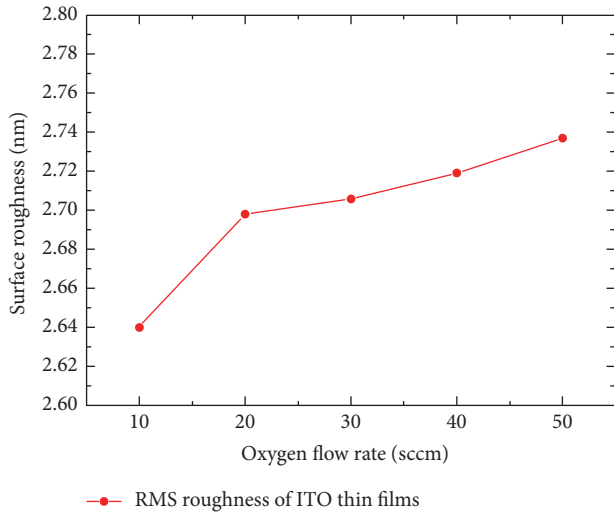


FIGURE 7: Surface roughness of ITO thin films as a function of oxygen flow rate.

ITO thin film growth becomes more dense (i.e., refractive index increasing) to form a compressive stress. Mattox [28] reported that energetic particle bombardment can introduce a compressive film stress. In a low-pressure sputtering deposition, energetic particle bombardment may induce high compressive film stress due to the recoil implantation of surface atoms. Besides, Windischmann [29] suggested that the compressive stress in sputtered films appears to be momentum rather than energy driven. However, no one model can explain all experimental data; the atomic peening model [30–32] appears to be more appropriate for sputtering deposition involving energy particle bombardment of the growing films leading to compressive stresses.

For the surface roughness measurements, the roughness can be characterized by several parameters and functions. The average roughness (R_a) is the most widely used because it is a simple parameter to obtain when compared to others. The root mean square (RMS) of roughness (R_q) is a function that takes the square of the measures. The surface roughness at a certain area is determined by the height differences of all the distinct points at this area. RMS roughness is the mean of the root for the deviation from the standard surface to the indicated surface. The measurement results show that the RMS surface roughness of ITO films increases with increasing of the oxygen flow rate, as shown in Figure 7. The RMS surface roughness is changed from 2.64 nm to 2.74 nm in the range of 10–50 sccm. It is clear that the ITO film prepared with low oxygen flow rate had a low RMS roughness value (2.64 nm) than that of the ITO films prepared in the high oxygen flow rate under the same deposition conditions. The reason may be due to bombardment of the more energetic particles on the growing film which causes the rough surface. We also found that the RMS surface roughness of ITO thin films increased with a corresponding increase in film thickness (Figure 4), while a relatively small surface roughness was obtained for the ITO films that were deposited at oxygen flow rate of 10 sccm. The lower flow rate helps in producing a smooth ITO film with suitable opto-electrical properties on substrates without

heating during deposition and/or additional post-annealing treatments.

4. Conclusions

This work demonstrates the influence of the oxygen flow rate on optical, electrical, and mechanical properties and surface roughness of DC sputtering ITO thin films. The ITO thin films were deposited on glass substrates and silicon wafer by DC magnetron sputtering technique under different oxygen flow rates. The ITO films prepared under the optimal deposition conditions had an optical transmittance of $\sim 85\%$ in the visible spectrum. The experimental results show that ITO thin films are not a function of the oxygen flow rate, but optical transmittance of all ITO films is over 85% in the visible region. At oxygen flow rate of 30 sccm, the transmittance of the ITO thin film has a maximum value of 88.7% for the wavelength of 500 nm. The electrical resistivity measurements reveal that the sheet resistance values of the ITO thin films increase with the increasing oxygen flow rate, and the electrical resistivity has a minimum of 6.85×10^{-4} ohm-cm for the oxygen flow rate of 10 sccm. The residual stress and surface roughness increase as the oxygen flow rate increases in the range of 10–50 sccm. In this study, the optimum depositing parameter is the oxygen flow rate of 10 sccm which results in a high transmission of 88%, the lowest resistivity of 6.85×10^{-4} ohm-cm, a lower residual stress of -0.15 GPa, and the RMS surface roughness of 2.64 nm.

Conflicts of Interest

The authors declare that they have no conflicts of interest.

Acknowledgments

This work was supported by the Ministry of Science and Technology (MOST) of Taiwan under Grants MOST 103-2221-E-035-032 and MOST 104-2221-C-035-058-MY2. The authors appreciate the Precision Instrument Support Center of Feng Chia University for providing the fabrication and measurement facilities.

References

- [1] M. Bender, W. Seelig, C. Daube, H. Frankenberger, B. Ocker, and J. Stollenwerk, "Dependence of oxygen flow on optical and electrical properties of DC-magnetron sputtered ITO films," *Thin Solid Films*, vol. 326, no. 1-2, pp. 72–77, 1998.
- [2] A. Salehi, "The effects of deposition rate and substrate temperature of ITO thin films on electrical and optical properties," *Thin Solid Films*, vol. 324, no. 1-2, pp. 214–218, 1998.
- [3] D. V. Morgan, Y. H. Aliyu, R. W. Bunce, and A. Salehi, "Annealing effects on opto-electronic properties of sputtered and thermally evaporated indium-tin-oxide films," *Thin Solid Films*, vol. 312, no. 1-2, pp. 268–272, 1998.
- [4] L.-J. Meng and M. P. dos Santos, "Structure effect on electrical properties of ITO films prepared by RF reactive magnetron sputtering," *Thin Solid Films*, vol. 289, no. 1-2, pp. 65–69, 1996.

- [5] O. J. Gregory, Q. Luo, and E. E. Crisman, "High temperature stability of indium tin oxide thin films," *Thin Solid Films*, vol. 406, no. 1-2, pp. 286–293, 2002.
- [6] K. Zhang, F. Zhu, C. H. A. Huan, and A. T. S. Wee, "Effect of hydrogen partial pressure on optoelectronic properties of indium tin oxide thin films deposited by radio frequency magnetron sputtering method," *Journal of Applied Physics*, vol. 86, no. 2, pp. 974–980, 1999.
- [7] H.-Y. Yeom, N. Popovich, E. Chason, and D. C. Paine, "A study of the effect of process oxygen on stress evolution in d.c. magnetron-deposited tin-doped indium oxide," *Thin Solid Films*, vol. 411, no. 1, pp. 17–22, 2002.
- [8] F. Zhu, C. H. A. Huan, K. Zhang, and A. T. S. Wee, "Investigation of annealing effects on indium tin oxide thin films by electron energy loss spectroscopy," *Thin Solid Films*, vol. 359, no. 2, pp. 244–250, 2000.
- [9] S. Laux, N. Kaiser, A. Zöller, R. Götzelmann, H. Lauth, and H. Bernitzki, "Room-temperature deposition of indium tin oxide thin films with plasma ion-assisted evaporation," *Thin Solid Films*, vol. 335, no. 1-2, pp. 1–5, 1998.
- [10] K. R. Narasimha, "Optical and electrical properties of indium-tin oxide films," *Indian Journal of Pure & Applied Physics*, vol. 42, no. 3, pp. 201–204, 2004.
- [11] R. Bel Hadj Tahar, T. Ban, Y. Ohya, and Y. Takahashi, "Electronic transport in tin-doped indium oxide thin films prepared by sol-gel technique," *Journal of Applied Physics*, vol. 83, no. 4, pp. 2139–2141, 1998.
- [12] L.-J. Meng, J. Gao, R. A. Silva, and S. Song, "Effect of the oxygen flow on the properties of ITO thin films deposited by ion beam assisted deposition (IBAD)," *Thin Solid Films*, vol. 516, no. 16, pp. 5454–5459, 2008.
- [13] Y. J. Kim, S. B. Jin, S. I. Kim, Y. S. Choi, I. S. Choi, and J. G. Han, "Effect of oxygen flow rate on ITO thin films deposited by facing targets sputtering," *Thin Solid Films*, vol. 518, no. 22, pp. 6241–6244, 2010.
- [14] A. Chen, K. Zhu, H. Zhong, Q. Shao, and G. Ge, "A new investigation of oxygen flow influence on ITO thin films by magnetron sputtering," *Solar Energy Materials & Solar Cells*, vol. 120, pp. 157–162, 2014.
- [15] J. C. Manificier, J. Gasiot, and J. P. Fillard, "A simple method for the determination of the optical constants n , k and the thickness of a weakly absorbing thin film," *Journal of Physics E: Scientific Instruments*, vol. 9, no. 11, pp. 1002–1004, 1976.
- [16] J. A. Thornton and D. W. Hoffman, "Stress-related effects in thin films," *Thin Solid Films*, vol. 171, no. 1, pp. 5–31, 1989.
- [17] C.-L. Tien and H.-D. Zeng, "Measuring residual stress of anisotropic thin film by fast Fourier transform," *Optics Express*, vol. 18, no. 16, pp. 16594–16600, 2010.
- [18] C.-L. Tien, K.-C. Yu, T.-Y. Tsai, and M.-C. Liu, "Effect of RF power on the optical, electrical, mechanical and structural properties of sputtering Ga-doped ZnO thin films," *Applied Surface Science*, vol. 354, pp. 79–84, 2015.
- [19] G. G. Stoney, "The tension of metallic films deposited by electrolysis," *Proceedings of the Royal Society A Mathematical, Physical and Engineering Sciences*, vol. 82, no. 553, pp. 172–175, 1909.
- [20] C.-L. Tien, K.-C. Yu, T.-Y. Tsai, C.-S. Lin, and C.-Y. Li, "Measurement of surface roughness of thin films by a hybrid interference microscope with different phase algorithms," *Applied Optics*, vol. 53, no. 29, pp. H213–H219, 2014.
- [21] L.-J. Meng, A. Maçarico, and R. Martins, "Study of annealed indium tin oxide films prepared by rf reactive magnetron sputtering," *Vacuum*, vol. 46, no. 7, pp. 673–680, 1995.
- [22] H. Kim, C. M. Gilmore, A. Piqué et al., "Electrical, optical, and structural properties of indium-tin-oxide thin films for organic light-emitting devices," *Journal of Applied Physics*, vol. 86, no. 11, pp. 6451–6461, 1999.
- [23] F. Kurdesau, G. Khripunov, A. F. da Cunha, M. Kaelin, and A. N. Tiwari, "Comparative study of ITO layers deposited by DC and RF magnetron sputtering at room temperature," *Journal of Non-Crystalline Solids*, vol. 352, no. 9–20, pp. 1466–1470, 2006.
- [24] V. Teixeira, H. N. Cui, L. J. Meng, E. Fortunato, and R. Martins, "Amorphous ITO thin films prepared by DC sputtering for electrochromic applications," *Thin Solid Films*, vol. 420–421, pp. 70–75, 2002.
- [25] K.-S. Tseng and Y.-L. Lo, "Effects of cumulative ion bombardment on ITO films deposited on PET and Si substrates by DC magnetron sputtering," *Optical Materials Express*, vol. 4, no. 4, pp. 764–775, 2014.
- [26] T. C. Gorjanc, D. Leong, C. Py, and D. Roth, "Room temperature deposition of ITO using R.F. Magnetron sputtering," *Thin Solid Films*, vol. 413, no. 1-2, pp. 181–185, 2002.
- [27] J.-H. Gu, J.-L. Si, J.-X. Wang, Y.-Y. Feng, X.-Y. Gao, and J.-X. Lu, "Indium-tin oxide films obtained by DC magnetron sputtering for improved Si heterojunction solar cell applications," *Chinese Physics B*, vol. 24, no. 11, Article ID 117703, 2015.
- [28] D. M. Mattox, "Particle bombardment effects on thin-film deposition: A review," *Journal of Vacuum Science & Technology A*, vol. 7, no. 3, pp. 1105–1114, 1989.
- [29] H. Windischmann, "Intrinsic stress in sputtered thin films," *Journal of Vacuum Science & Technology A*, vol. 9, no. 4, pp. 2431–2436, 1991.
- [30] F. M. D'Heurle, "Aluminum films deposited by rf sputtering," *Metallurgical and Materials Transactions B: Process Metallurgy and Materials Processing Science*, vol. 1, no. 3, pp. 725–732, 1970.
- [31] C. A. Davis, "A simple model for the formation of compressive stress in thin films by ion bombardment," *Thin Solid Films*, vol. 226, no. 1, pp. 30–34, 1993.
- [32] M. Ohring, *Materials Science of Thin Films: Deposition and Structure*, Academic Press, San Diego, Calif, USA, 2nd edition, 2002.

Research Article

High Sensitivity Refractive Index Sensor by D-Shaped Fibers and Titanium Dioxide Nanofilm

Chuen-Lin Tien ^{1,2}, Hong-Yi Lin,² and Shu-Hui Su²

¹Department of Electrical Engineering, Feng Chia University, Taichung 40724, Taiwan

²Ph. D. Program of Electrical and Communications Engineering, Feng Chia University, Taichung 40724, Taiwan

Correspondence should be addressed to Chuen-Lin Tien; cltien@fcu.edu.tw

Received 17 November 2017; Accepted 7 December 2017; Published 5 February 2018

Academic Editor: Shuan-Yu Huang

Copyright © 2018 Chuen-Lin Tien et al. This is an open access article distributed under the Creative Commons Attribution License, which permits unrestricted use, distribution, and reproduction in any medium, provided the original work is properly cited.

This paper presents a high sensitivity liquid refractive index (RI) sensor based on lossy mode resonance (LMR) effect. The D-shaped fibers coated with nanosized titanium dioxide (TiO_2) thin film as a sensing head were submerged into different refractive index solutions. The variations in the optical spectrum of the proposed RI sensor with different refractive index solutions were measured. The LMR resonance peaks were used to determine the wavelength shifts with different refractive index solutions. The results show that the optical spectrum peaks shifted towards the longer wavelength side with increasing the refractive index. For the proposed fiber sensing head with a polishing residual thickness of $72\ \mu\text{m}$, the maximum shift of the absorption peak was 264 nm. The sensitivity of the proposed RI sensor was 4122 nm/RIU for the refractive index range from 1.333 to 1.398.

1. Introduction

Many fiber-optic sensors for refractive index (RI) sensing have been developed due to some advantages such as small size, high sensitivity, light weight, and immunity to external electromagnetic interference. Various fabrication methods for fiber-based RI sensors have been reported in the literature [1], including surface plasmon resonance (SPR) [2, 3], evanescent field [4], fiber gratings [5, 6], and optical fiber interferometry [7]. However, the sensitivity of the traditional sensing techniques needs to be improved in practical applications. Iadicco et al. [5] reported an etched fiber Bragg grating RI measurement, while etching can also be applied to a long period of grating to increase sensitivity to external refractive indices [6]. Optical fiber sensors based on evanescent wave generate a strong interaction between the guided wave and the surrounding materials. However, most of the reported sensors showed a low-sensitivity or low-detection range. To overcome this problem, we proposed a D-shaped optical fiber coated with a high refractive index titanium dioxide (TiO_2) nanofilm to enhance the sensitivity and to extend the detection range of the sensor.

In the last decades, thin film coated onto a fiber-optic has become a widely explored technique in the field of sensors.

The effects of depositing a thin, highly refractive index (RI) layer onto the cladding over the grating region have been reported [8, 9]. Since titanium dioxide (TiO_2) is one of the highly refractive index materials, TiO_2 is known to be a good photocatalytic material under UV radiation. In this study, we present the fabrication of high sensitivity refractive index fiber-optic sensors based on D-shaped fibers and nanosized TiO_2 coatings. From the optical point of view, TiO_2 nanofilm deposited on D-shaped fibers can generate lossy mode resonance (LMR) effect under particular conditions [10]. In this work, we fabricate a new liquid refractive index fiber-optic sensor called a D-LMR (D-shaped fiber with lossy mode resonance) sensor that combines with the D-shaped fibers and nanosized TiO_2 coatings to achieve a high sensitivity sensor with a wide range of liquid refractive indices. We also utilized a DC magnetron sputtering technique to deposit TiO_2 nanofilms on the polished surface of D-shaped fibers for the fabrication of liquid refractive index fiber sensors. The proposed D-shaped fiber sensor structure includes a low index upper cladding (about $3\text{--}5\ \mu\text{m}$ thick) between the fiber core and the TiO_2 layer that is different from an uncladded fiber structure in the literature [10–12]. Our fiber structure design will help in giving the D-shaped fiber good mechanical support after side-polishing. This paper demonstrates the

D-LMR type RI sensors with a high sensitivity for liquid refractive index measurements. The characteristics of the resonance-based fiber-optic sensors could be extensively used as refractometers to detect the refractive index changes in liquids.

2. Method

If a side-polished optical fiber is coated with a thin film, the propagation of the guided wave is affected. The thin film coatings combined with side-polished optical fibers can produce two different resonance types: one is surface plasmon resonances (SPRs) [8] and the other is lossy mode resonances (LMRs) [9–11]. The surface plasmon resonance (SPR) occurs when the real part of the thin film permittivity is negative and higher in magnitude than both its own imaginary part and the permittivity of the material surrounding the thin films. The LMR effect can be generated by the metal oxide films whose real part of the permittivity is positive and higher in magnitude than both the imaginary part of the permittivity and the permittivity of the surrounding material. The LMR effect is achieved for metal oxide films with low imaginary part of the complex refractive index. In general, a specified thin film coated onto a D-shaped fiber can generate LMR effect based on a modified Kretschmann configuration [10]. LMR phenomenon has been observed with metal oxides, such as indium tin oxide (ITO) [12], titanium oxide [13], and indium oxide [14]. Apart from this, LMR effect appears for both TM and TE polarized light, and the generation of multiple resonances without modifying the optical fiber geometry is also possible [15]. According to the mode coupling theory, an LMR is the result of light coupling between evanescent waves and lossy modes guided in the absorbing thin films. Thus, the analysis of the evolution of the modal effective refractive index is helpful in understanding the generation of the resonance.

Since all of the materials are characterized by their relative permittivity, titanium dioxide thin films can be characterized by a complex form of relative permittivity. The oscillatory model represents the dielectric constant of TiO₂ thin films and it can be expressed as follows [16]:

$$\varepsilon(\omega) = \varepsilon_{\infty} - \frac{\omega_p^2}{\omega^2 + i(\omega/\tau)}, \quad (1)$$

where ε_{∞} is the dielectric constant of the high electron density region in the film, τ is the Drude damping time for free electrons, ω is the incident light frequency, and ω_p is the plasma frequency. It should be noted that the dielectric constant was predicted by the Drude model [17]. The plasma frequency is determined by the following formula:

$$\omega_p^2 = \frac{Ne^2}{\varepsilon_0 m^* m}, \quad (2)$$

where N is the electron density, e is the electron charge, ε_0 is the dielectric constant, m is the electron mass, and m^* is the optical effective mass for carriers [18].

As mentioned above, the generation of LMR is based on D-shaped fibers coated with absorbing thin films which

modified the well-known Kretschmann configuration. If TiO₂ films are deposited on the polishing surface of D-shaped fibers, then the real part of the refractive index of TiO₂ films will always be higher than that of the D-shaped fiber in the wavelength region of our study. Besides, when the index of the surrounding medium above the TiO₂ nanolayer is 1.333, the structure will support guided modes. These modes will be lossy because of the imaginary part of the index of TiO₂ films. Thus, the dispersion curves for the proposed sensor structure (D-shaped fiber/TiO₂ layer/surrounding medium) will be similar to the dielectric waveguides [19]. The number of modes supported by this waveguide increases with increasing the film thickness. Batchman and McWright [20] studied the light propagation through semiconductor cladded waveguides. The attenuation maxima of the light propagating through the optical waveguide can be obtained for specific thicknesses and at certain wavelengths. This effect can be explained as a periodic coupling between the guided modes of the lossless structure and the lossy modes supported by the high refractive index material. Therefore, the mode loss is maximal if the thickness of the coating layer corresponds to the cut-off thickness for that particular mode. Carson and Batchman [21] reported that a thin film is deposited on the single mode waveguide; the mode losses for either TE or TM become maximal at its particular thickness. This happens due to the lossy nature of the thin film and the phase matching between the guided mode supported by a lossless dielectric waveguide and the lossy mode supported by the thin film.

In this work, the proposed D-LMR fiber sensor can be fabricated by using the D-shaped fiber and thin film coating technique. It is a challenging work to keep a uniform thickness of the TiO₂ nanolayer coated on a side-polished surface of the single mode fibers. A DC magnetron sputtering technique is an efficient approach to obtain a uniform nanolayer coating of TiO₂ films with a low surface roughness. The performance of the proposed RI sensor is evaluated in terms of wavelength sensitivity and linearity.

3. Experimental

Using a side-polishing technique to make D-shaped fiber, we modified the motor-driven polishing method [22] to suspend the optical fibers and to control the polishing surface depth. To ensure correct polishing depth, a PC-based measuring system with a photometer was used to monitor and control the polishing process in real time. A large increase of power loss during polishing indicates that the cladding is thin enough for the light to radiate from the fiber core and that the polishing should be stopped.

A high sensitivity fiber-optic sensor is reached by thinning the optical fiber enough to obtain an evanescent wave interaction of the guided light with the surrounding mediums. For D-shaped optical fibers, the core is very close to the flat surface of the structure. As a direct consequence, an optical fiber thinning is enough to allow evanescent wave interaction of the guided light with the surrounding mediums. The D-shaped fiber section is sensitive to the surrounding medium refractive index allowing the measurement of different refractive indices in liquids.

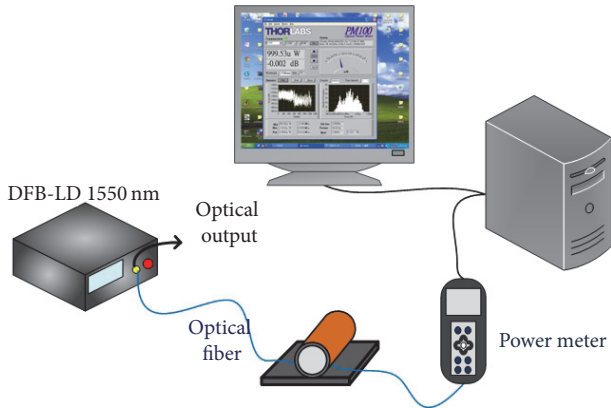


FIGURE 1: Schematic diagram of optical fiber polishing arrangement.

A single mode fiber (SMF-130V) was used to fabricate the sensing devices. Before the thin film deposition, the cladding was partially removed, and the resultant portion was ultrasonically cleaned. After this cleaning process, the fabrication of the sensors involved two different steps. First, we used the single mode fiber, ground/polished by using a home-made side-polishing machine. During the process of polishing the fiber, we need to monitor the polishing depth by checking the transmission light power levels, as shown in Figure 1. This measurement can confirm when the polished surface reaches the near fiber core region. The polished length was altered by changing the contact angle of the optical fiber on the wheel or by using a polishing wheel of different diameter. Under the optical fiber polishing conditions, where the wheel rotated at 15 rpm, the tension force on the optical fiber was approximately 0.2–0.3 N and the wheel was lubricated with liquid paraffin; the radial force on the wheel from the optical fiber was essentially uniform over the contact length and the optical fiber was polished uniformly over that length. The polished fiber diameter was also further measured by an optical microscope to precisely obtain the polished depth. The thickness and polishing length of the side-polished fibers were also measured by using an optical microscope. Figure 2 shows the microscopic image of the D-shaped fiber. The residual thickness of the side-polished fiber was about $72\ \mu\text{m}$ (including a $5\ \mu\text{m}$ -thick cladding layer), and the polishing length of the D-shaped fiber was 30 mm. Then, TiO_2 nanofilm was deposited on the D-shaped fiber surface by using a DC magnetron sputtering system. TiO_2 has the advantages of nontoxicity, environmental compatibility, high refractive index, and low price; therefore, we choose TiO_2 as the coating material.

Prior to the deposition, the coating substrates (including silicon wafers and the D-shaped fibers) had been ultrasonically cleaned in acetone and ethanol and then had been dried by a dryer. In a high-vacuum sputtering chamber, D-shaped fibers and silicon wafer were mounted onto a substrate holder 200 mm in diameter that rotated at a speed of 30 rpm. The flat side of D-shaped optical fibers offers a unique substrate on which thin films can be deposited. The D-shaped optical fibers were embedded in V-shaped

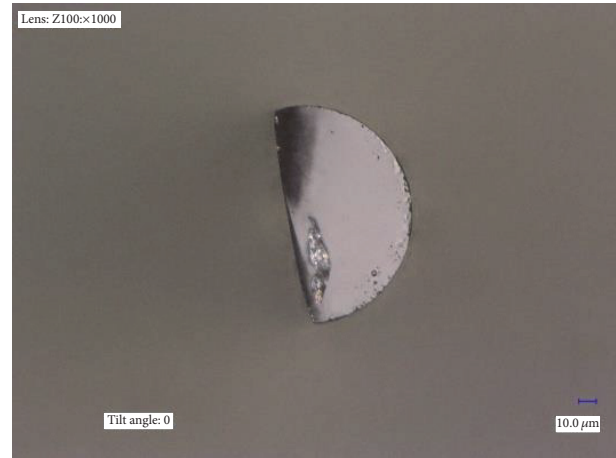


FIGURE 2: Microscopic image of the D-shaped fiber.

groove of a special fiber holder and the flat side of D-shaped fibers was parallel mounted to the surface of the substrate holder to keep the coating thickness uniform. For the DC sputtering depositions, titanium targets with purity of 99.99% and diameter of 76.2 mm were used. The target to substrate distance was 120 mm, the total pressure being set at 1.5×10^{-3} Torr. The reactive gas partial pressure was kept constant at 4.5×10^{-4} Torr during the deposition. For the preparation of the nanosized TiO_2 films, a mixture of argon and oxygen gases was used. The DC power and heating temperature were controlled to be 100 W and 80°C , respectively. Thin film was simultaneously deposited on the silicon wafers and the side-polished surfaces of the single mode fibers (SMF). The TiO_2 film's thickness of 84 nm was measured by using an ellipsometer.

To characterize the optical response of the D-LMR sensing device, a typical transmission setup was used. A portion of the coated optical fiber was cleaved at both ends and spliced to optical fiber patch cords. The spectral response of the sensor was obtained by using a typical optical transmission setup. Figure 3 shows that this setup consisted of a halogen white light source (Ocean Optics, HL-2000) connected at the input of the optical fiber, and the other end was attached to a near-infrared spectrometer (Ocean Optics, NIR 512). Thus, the light coupled to the side-polished fiber passed through the cladding removed sensitive region, which is located in the optical transmission pathway.

4. Results and Discussion

The absorption peaks generated by the LMR phenomenon can be observed in optical transmission spectrum. The wavelength interrogation method along with D-LMR type optical fiber sensors was considered in our analysis. The LMR wavelengths were determined from the normalized transmittance versus wavelength plot for different sensing liquid refractive indices. The data analysis for the proposed sensor was done by using MATLAB® software. The different sets of sensing medium (NaCl solutions) refractive indices

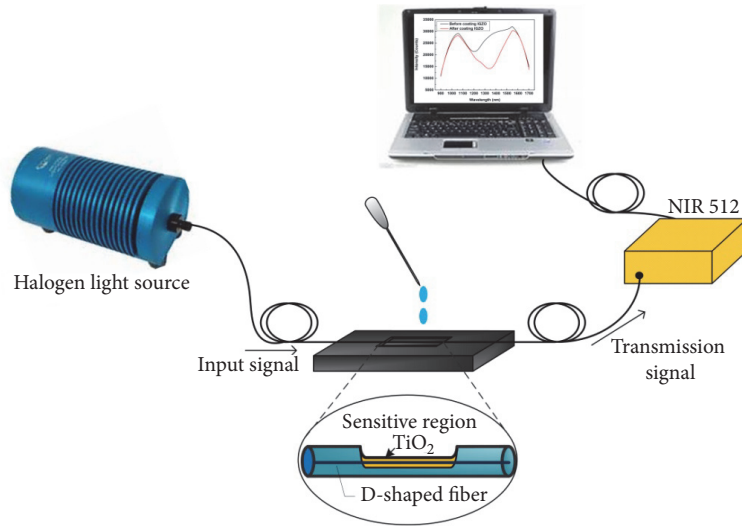


FIGURE 3: Schematic of the proposed RI sensor and experimental setup.

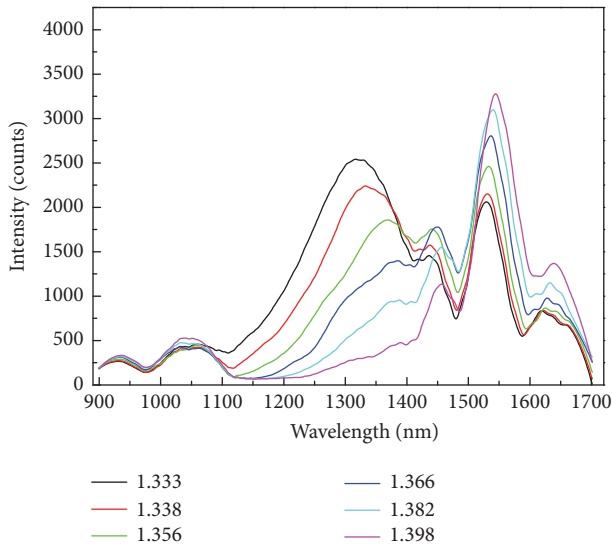


FIGURE 4: LMR spectra of the D-shaped fibers coated with TiO₂ nanofilm for different liquid refractive indices.

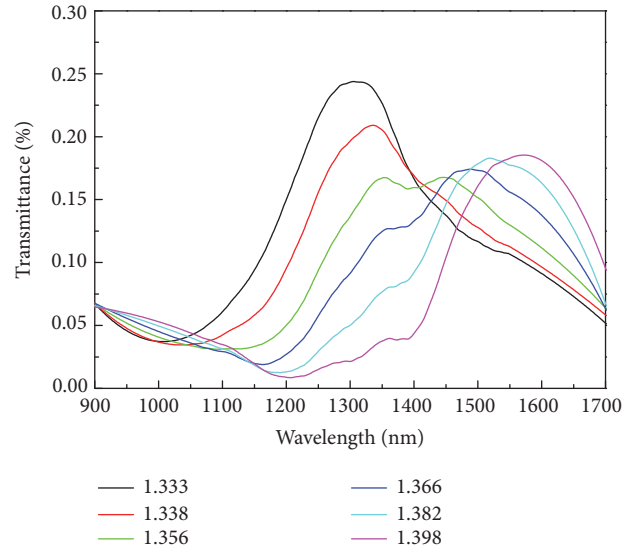


FIGURE 5: The transmittance spectra of different refractive index solutions by D-LMR optical fiber sensor.

used for the analysis were 1.333, 1.338, 1.356, 1.366, 1.382, and 1.398. Figure 4 shows the LMR transmission spectra of D-shaped fibers coated with nanosized TiO₂ film for different liquid refractive indices. The sensing sensitivity is defined as the shift of resonance wavelength versus the change in surrounding refractive index. If the refractive index value is increased by higher concentration of NaCl solutions, the LMR peak shifts to higher wavelengths. From the transmittance spectra, when the refractive index of the external medium is 1.333, the absorption peak is located at 1307 nm. When the refractive index of the external medium is 1.338, the absorption peak is located at 1335 nm. When the RI is 1.382, the peak is at 1520 nm, and when its value is 1.398 the peak reaches 1571 nm. Figure 5 illustrates the normalized transmittance of D-LMR optical fiber sensor for different

refractive index solutions. Here the transmittance is defined as the ratio of the transmitted light intensity to the incident light intensity. It is important to note that the wavelength's shift of the resonance peaks is a function of the refractive index of NaCl solutions, as shown in Figure 6. The sensing sensitivity of the D-LMR sensor was 4122 nm/RIU; RIU is refractive index units, for the fiber residual thickness of 72 μm and the polishing length of 30 mm. Figure 6 also shows the linear fitting of the resonant wavelength as a function of the liquid refractive index. The linear fitting curve demonstrates R^2 value of 0.980. In our previous publication [23], a liquid refractive index sensor using double-sided polishing long period fiber grating (DSP-LPFG) was reported. A sensing sensitivity of 143.4 nm/RIU for the DSP-LPFG sensor was obtained from the RI range of 1.333–1.375. In this work, the

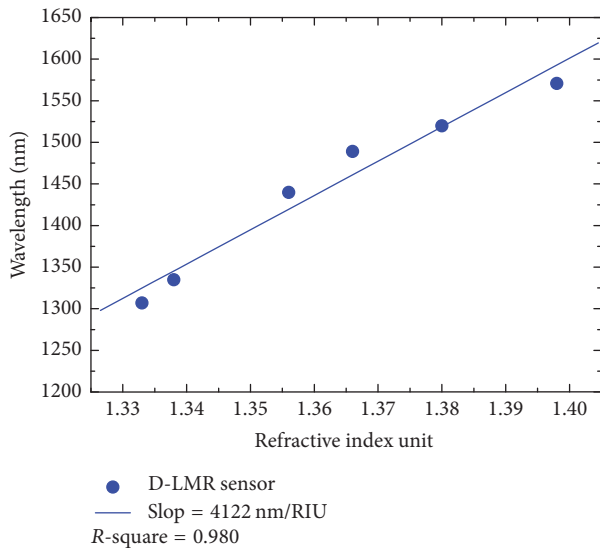


FIGURE 6: LMR wavelength as a function of the refractive index for different NaCl solutions.

experimental results show that the sensing sensitivity of the D-LMR sensor is 28 times higher than that of the DSP-LPFG sensor. These results also show that the sensing sensitivity of the D-LMR sensor is about 12 times higher than that of a tilted-LPFG sensor for liquid refractive index measurements [6]. The detection range of the proposed RI sensor is also extended.

5. Conclusion

We have proposed and demonstrated a novel D-LMR fiber sensor by coating TiO_2 nanofilms on D-shaped fibers. The D-LMR sensor response to the liquid refractive index changes has been carried out by measuring the resonance wavelength's shift. The results show that LMR peaks shift to higher wavelengths with increasing the liquid refractive index. The greatest sensitivity of the RI sensor that has been experimentally demonstrated is 4122 nm/RIU for the RI range from 1.333 to 1.398. Compared with other sensors, we propose that a simple structure based on a D-shaped fiber and nanosized TiO_2 coating layer will be more sensitive for the liquid refractive index measurements with the advantages of being more compact, of low cost, and easily portable. The general idea of proposed D-LMR sensor can also be applied to other sensing applications.

Conflicts of Interest

The authors declare that they have no conflicts of interest.

Acknowledgments

This work was supported by the Ministry of Science and Technology (MOST) of Taiwan under Grants MOST 103-2221-E-035-032 and 104-2221-E-035-058-MY2. The authors also appreciate the Precision Instrument Support Center

of Feng Chia University for providing the measurement facilities.

References

- [1] B. Culshaw and A. Kersey, "Fiber-optic sensing: a historical perspective," *Journal of Lightwave Technology*, vol. 26, no. 9, pp. 1064–1078, 2008.
- [2] D. Tanaka, S. Shinohara, E. Usukura, P. Wang, K. Okamoto, and K. Tamada, "High-sensitivity surface plasmon resonance sensors utilizing high-refractive-index silver nanoparticle sheets," *Japanese Journal of Applied Physics*, vol. 53, no. 1, Article ID 01AF01, 2014.
- [3] M. R. Hasan, S. Akter, M. S. Rahman, and K. Ahmed, "Design of a surface plasmon resonance refractive index sensor with high sensitivity," *Optical Engineering*, vol. 56, no. 08, article 087101, 2017.
- [4] C. R. Taitt, G. P. Anderson, and F. S. Ligler, "Evanescent wave fluorescence biosensors," *Biosensors and Bioelectronics*, vol. 20, no. 12, pp. 2470–2487, 2005.
- [5] A. Iadicco, A. Cusano, S. Campopiano, A. Cutolo, and M. Giordano, "Thinned fiber Bragg gratings as refractive index sensors," *IEEE Sensors Journal*, vol. 5, no. 6, pp. 1288–1294, 2005.
- [6] H. J. Patrick, A. D. Kersey, and F. Bucholtz, "Analysis of the response of long period fiber gratings to external index of refraction," *Journal of Lightwave Technology*, vol. 16, no. 9, pp. 1606–1612, 1998.
- [7] J. Zhou, Y. Wang, C. Liao et al., "Intensity modulated refractive index sensor based on optical fiber Michelson interferometer," *Sensors and Actuators B: Chemical*, vol. 208, pp. 315–319, 2015.
- [8] N. D. Rees, S. W. James, R. P. Tatam, and G. J. Ashwell, "Optical fiber long-period gratings with Langmuir-Blodgett thin-film overlays," *Optics Express*, vol. 27, no. 9, pp. 686–688, 2002.
- [9] M. Jiang, Q.-S. Li, J.-N. Wang et al., " TiO_2 nanoparticle thin film-coated optical fiber Fabry-Perot sensor," *Optics Express*, vol. 21, no. 3, pp. 3083–3090, 2013.
- [10] P. Zubiato, C. R. Zamarreño, I. Del Villar, I. R. Matias, and F. J. Arregui, "Experimental study and sensing applications of polarization-dependent lossy mode resonances generated by D-shape coated optical fibers," *Journal of Lightwave Technology*, vol. 33, no. 12, Article ID 7010892, pp. 2412–2418, 2015.
- [11] I. Del Villar, M. Hernaez, C. R. Zamarreño et al., "Design rules for lossy mode resonance based sensors," *Applied Optics*, vol. 51, no. 19, pp. 4298–4307, 2012.
- [12] P. Zubiato, C. R. Zamarreño, I. Del Villar, I. R. Matias, and F. J. Arregui, "High sensitive refractometers based on lossy mode resonances (LMRs) supported by ITO coated D-shaped optical fibers," *Optics Express*, vol. 23, no. 6, pp. 8045–8050, 2015.
- [13] M. Hernáez, I. Del Villar, C. R. Zamarreño, F. J. Arregui, and I. R. Matias, "Optical fiber refractometers based on lossy mode resonances supported by TiO_2 coatings," *Applied Optics*, vol. 49, no. 20, pp. 3980–3985, 2010.
- [14] P. Sanchez, C. R. Zamarreño, M. Hernaez, I. R. Matias, and F. J. Arregui, "Optical fiber refractometers based on Lossy Mode Resonances by means of SnO_2 sputtered coatings," *Sensors and Actuators B: Chemical*, vol. 202, pp. 154–159, 2014.
- [15] C. R. Zamarreño, P. Zubiato, M. Sagües, I. R. Matias, and F. J. Arregui, "Experimental demonstration of lossy mode resonance generation for transversemagnetic and transverse-electric polarizations," *Optics Express*, vol. 38, no. 14, pp. 2481–2483, 2013.

- [16] T. Shinonaga, M. Tsukamoto, and G. Miyaji, "Periodic nanostructures on titanium dioxide film produced using femtosecond laser with wavelengths of 388 nm and 775 nm," *Optics Express*, vol. 22, no. 12, pp. 14696–14704, 2014.
- [17] I. Hamberg, A. Hjortsberg, and C. G. Granqvist, "High quality transparent heat reflectors of reactively evaporated indium tin oxide," *Applied Physics Letters*, vol. 40, no. 5, pp. 362–364, 1982.
- [18] K. Sokolowski-Tinten and D. Von Der Linde, "Generation of dense electron-hole plasmas in silicon," *Physical Review B: Condensed Matter and Materials Physics*, vol. 61, no. 4, pp. 2643–2650, 2000.
- [19] A. Kumar, V. K. Sharma, D. Kumar, and A. Kapoor, "Integrated optic TE/TM pass polarizers using resonant coupling between ITO thin film lossy modes and dielectric waveguide modes," *Optics Communications*, vol. 291, pp. 247–252, 2013.
- [20] T. E. Batchman and G. M. McWright, "Mode Coupling Between Dielectric and Semiconductor Planar Waveguides," *IEEE Transactions on Microwave Theory and Techniques*, vol. 30, no. 4, pp. 628–634, 1982.
- [21] R. F. Carson and T. E. Batchman, "Multimode phenomena in semiconductor-clad dielectric optical waveguide structures," *Applied Optics*, vol. 29, no. 18, pp. 2769–2780, 1990.
- [22] C. D. Hussey and J. D. Minelly, "Optical fibre polishing with a motor-driven polishing wheel," *IEEE Electronics Letters*, vol. 24, no. 13, pp. 805–807, 1988.
- [23] C. Tien, T. Lin, H. Hsu, and W. Liu, "Double-Sided Polishing Long Period Fiber Grating Sensors for Measuring Liquid Refractive Index," in *Proceedings of the Asia Communications and Photonics Conference and Exhibition*, vol. 7634, p. 76341A, Shanghai, China, 2009.